Computational and Experimental Studies of Field-Driven Additive Manufacturing Processes

By

Zachary Yun

A dissertation submitted in partial satisfaction of the

requirements for the degree of

Doctor of Philosophy

in

Engineering - Mechanical Engineering

in the

Graduate Division

of the

University of California, Berkeley

Committee in charge:

Professor Tarek I Zohdi, Chair
Professor Simo Mäkiharju
Professor Per-Olof Persson

Spring 2023

Computational and Experimental Studies of Field-Driven Additive Manufacturing Processes

Abstract

Computational and Experimental Studies of Field-Driven Additive Manufacturing Processes

by

Zachary Yun

Doctor of Philosophy in Engineering - Mechanical Engineering

University of California, Berkeley

Professor Tarek I Zohdi, Chair

Industrial coating and painting operations have used electric fields as a driving force for decades to help more of the particles reach and stick to the intended part. More recently, this concept has been explored for use in additive manufacturing (AM) processes as a way to control the microstructure and geometry of particle deposits through processes like Electrospray Deposition and Electrophoretic Deposition (EPD). These AM processes are increasingly used to make components that require specific structures such as colloidal crystals made of micro- and nano- particles, which are then used in applications in microelectronics, sensors, and superlattice materials. So far, most development of the EPD process for colloidal crystals has been performed via experiments, with many measurements taken *ex-situ* to weigh deposits over time. However these experiments do not directly observe how the particles integrate into the crystal, so the kinetics of the deposit formation are not yet well understood. This work aims to contribute towards EPD and other field-driven AM process development in two ways: 1) by creating a computational framework to directly simulate the particles in these field-driven processes and 2) work towards an experimental platform for *in-situ* observations of these particles to better understand how they form the deposit.

In this dissertation, I present my work towards a computational framework for simulating these field-driven processes and a preliminary experimental setup for *in-situ* process observation. The simulation model captured the essential physics of the processes, while remaining computationally tractable on limited resources, such as a laptop. I discuss the results from verification studies showing good agreement with analytical theory as the model is developed and then use illustrative examples to explore deposit behavior under different processing conditions. I then present preliminary results from experiments aimed at further expanding observations of EPD. The preliminary results from both the simulation and experimental work show that these methods can contribute to process development and have several avenues for future extensions.

To my amazing family and friends, thank you for everything. I could not have crossed the finish line without you.

Contents

List of Figures

List of Tables

Acknowledgments

I am deeply thankful and fortunate to have worked with my advisor Prof. Tarek Zohdi, and want to express my gratitude for his support through these last several years. When first starting grad school, I was relatively new to using simulation tools, but through his course and further discussions, my interest expanded and culminated in this work. The support and guidance brought me here, and I will always be thankful. I also want to thank my committee members, Prof. Simo Mäkiharju and Prof. Per-Olof Persson, both of whom provided guidance in the experimental and numerical methods realms that was invaluable for the completion of my PhD.

My work would not have been the same without the support and mentorship from Dr. Andy Pascall and the many members of the Center for Engineered Materials and Manufacturing at LLNL that I had the honor of working with. The opportunity to work with the scientists at the lab first as an intern, then as a student collaborator further fueled my interest in additive manufacturing and research and helped to motivate me through even the toughest times when the ability to perform experiments was limited and uncertain during the pandemic. Continued discussions about work and, just as importantly, life outside of work with Andy and many others in the CEMM were invaluable.

I am thankful to my fellow lab-mates for their support and will always remember our shared successes and trials through late nights working in the office. Specifically I'd like to thank Roger Isied and Nico Castrillon, our shared efforts on our PhDs, coursework, and expansive side projects brought us all through the grad school experience together (even if I took a little extra time).

Finally I want to thank my family and friends for their unwavering support throughout my time working on my PhD. Spending time with family and friends in the bay and beyond made even the hardest times throughout my years here good times. The unwavering support from my parents and siblings continues to be a source of motivation and pushes me to higher heights. Your love and support means the world to me. Thank you all, I could not have done this without you.

This work was performed under the auspices of the U.S. Department of Energy by Lawrence Livermore National Laboratory under Contract DE-AC52-07NA27344.

Chapter 1

Introduction

1.1 Field-Driven Deposition and Additive Manufacturing

The technique of using external fields such as electric fields to facilitate the motion of particles to form deposits and coatings has been utilized by industry for many years. These deposits and coatings can be used for many functions including environmental and corrosion protection, thermal and electrical insulation, and electron emission components. An early adopter of the techniques used an electric field to deposit thoria particles for use in an electron tube in the early 1930's [7], and industry continues to use these techniques today in processes like electroplating, electrostatic painting as shown in Figure 1.1, and many others. In these techniques, the basic principle of operation relies on electrical charge: the particles will be given a charge while the work piece or substrate has an opposite charge. The charged particles are then attracted to the oppositely charged work piece and form a coating or deposit. This has several advantages including less waste and time, as the particles are attracted to the surface of the work piece, and better ease of coverage, as surfaces out of the direct sprayer path can still attract particles.

The painting and coating examples shown in Figure 1.1 are two illustrative examples of how these external fields can drive particle deposition in different mediums. In panel a), the robot arms are spray painting the car body in air, while in panel b) the car body is being coated while immersed in a liquid suspension. In both cases, the car body is oppositely charged from the particles and will attract them to all parts of the surface.

While these methods have been used for decades in industry for coating, the techniques of using external fields has more recently been a topic of study when combined with modern Additive Manufacturing (AM) methods. The construction of parts or components by *adding* material as opposed to removing material from a raw piece of material like in machining or other subtractive methods leads to completely different design possibilities. These can include complex geometries with features such as integrated cooling channels and components with added electrical, optical, thermodynamic functionality [35]. Varied materials and

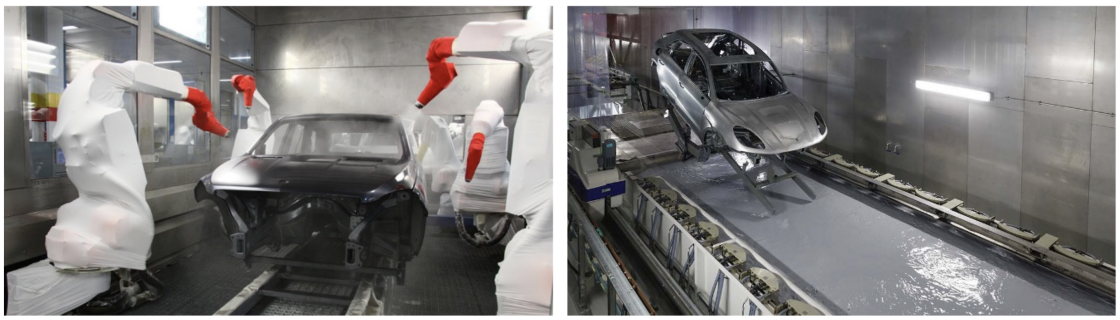

Figure 1.1: Examples of industrial use of external fields for painting and coating. a) Electrostatic spray painting of a car body, from [46]. b) Electrophoretic coating of a car body, from [47].

geometries can be additively manufactured in many processes including extrusion-based processes, powder bed-based processes, vat photopolymerization processes, material and binder jetting, and many more [20].

Since AM's expansion in the 1980's with stereolithography, the capabilities of these processes to expand potential materials used and functional material properties in completed parts, and to reduce material waste and production time, have continued to be developed. This development has been augmented wby the combination of some of the original AM process concepts with external fields [27] [26]. Recent research efforts have combined acoustic, electrical, and magnetic fields with AM processes to increase the process capabilities. Some examples include: an acoustic field selective powder delivery system for powder bed sintering [65], where different material powders were dispensed depending on the frequency applied to the dispensing system allowing for tailored material deposition; a magnetic field-aided selective laser melting system where the applied static magnetic field helped different titanium phases migrate before total solidification resulting in a more homogeneous microstructure and increased tensile strength and ductility compared to parts made with the same selective laser melting process without a magnetic field[29]; and a jet-printing process that used an electric field to effectively constrict the jet size beyond the size of the physical nozzle to increase print resolution to achieve microscale features [64]. Another example uses a magnetic field in a direct energy deposition process to attract ferritic steel powder to the substrate; this process improved the amount of powder that stuck to the target substrate before melting [55]. More examples of recent field-aided AM processes were reviewed by Hu, which further emphasizes a trend of increasing interest in combining external fields with AM processes to continue improving AM capabilities [26].

Speaking more specifically to the deposition processes, there has been recent research interest in adapting the field-driven deposition processes described above in a more controlled manner to control the resulting structure and build up components. Some examples of this

include Electrospray Deposition, and light-directed Electrophoretic Deposition as shown in Figure 1.2.

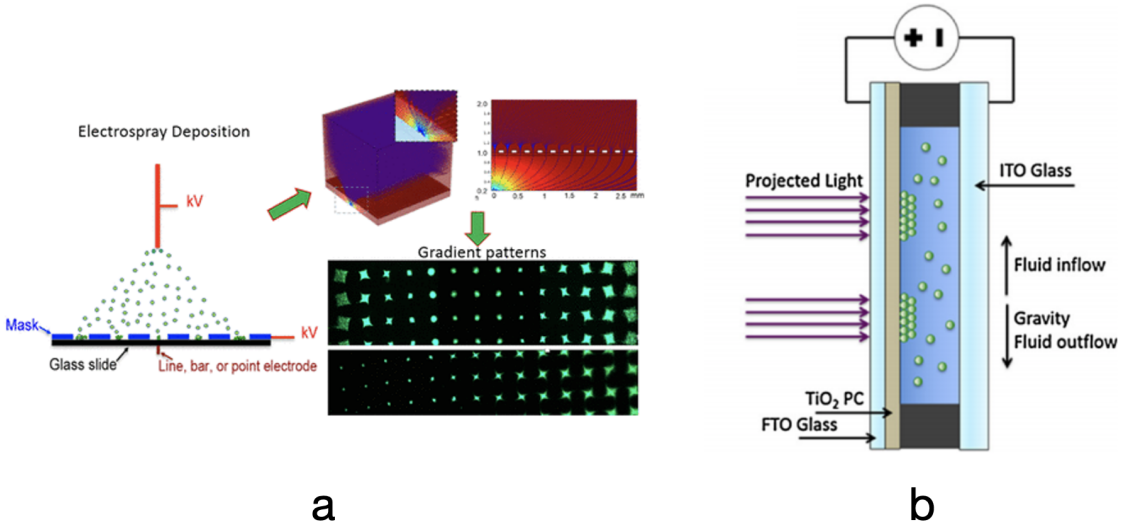

Figure 1.2: Schematics of electric-field aided deposition processes. a) Electrospray deposition resulting in gradient patterns in a deposit from Yan et al. [63]. b) Light-Directed EPD where the conductive areas are defined by the projected light from Mora et al.[37].

These processes will be essentially the main focus of the following work as I investigate how the physics behind processes like Electrospray Deposition and Electrophoretic Deposition (EPD) create particle deposits under different processing conditions. While introduced here, more details on the process will be given below in Chapter 2. In Figure 1.2, panel a) shows a schematic of the Electrospray Deposition process used by Yan et al. to deposit particles through air onto a substrate [63]. By controlling the electric field pattern on the target substrate, they demonstrated controllable gradient patterns in the resulting deposit. Panel b) shows a schematic of Light-Directed EPD in which the substrate was coated with a photoconductive layer so the illuminated region serves as the conductive target. When the electric field is applied, the particles deposit on the illuminated conductive area. As time passes, the user can change the area being illuminated, resulting in a new conductive area where deposition will occur. This can lead to a layer-by-layer deposition building up parts as an AM process.

These processes can be used to manufacture components with a wide range of applications including localized functional coatings, multimaterial structures, architectured materials with tailored microstructures for enhanced material properties [56], and colloidal crystals which in turn can be used for numerous applications including photonic crystals [62], superlattice materials [28], and environmental sensors [32]. Colloidal crystals are crystalline

structures made of micro- and nano-particles and serve as a motivating application for the direction of this research. In Chapter 2, I go into further detail about prior research with the EPD process and how the kinetics of the particle integration into a crystalline structure are not yet well understood. Examples of a multimaterial deposition and a colloidal crystal are shown in Figure 1.3.

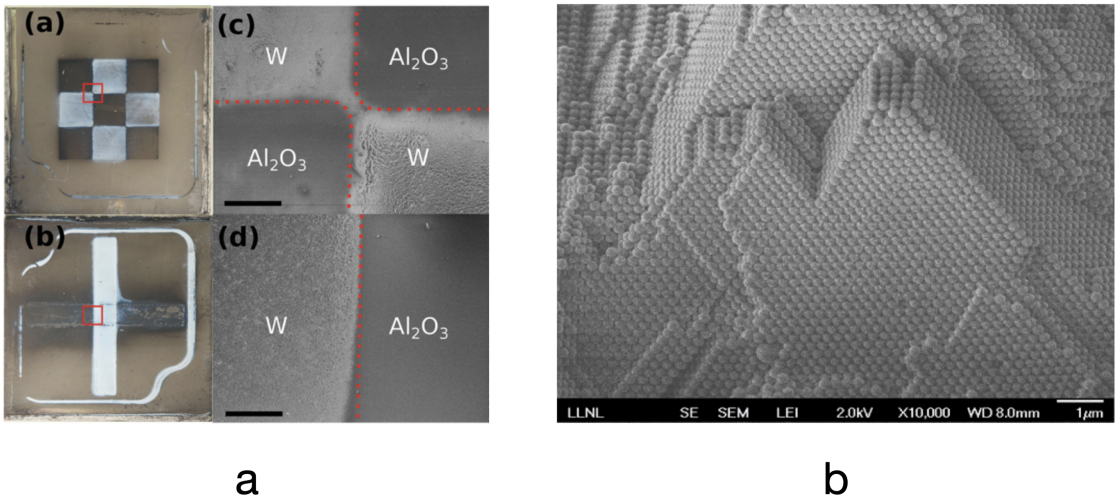

Figure 1.3: Examples of some applications of EPD. a) Multimaterial deposits made with Light-Directed EPD from Pascall et al. [44]. b) Colloidal crystal structure SEM micrograph, courtesy of Dr. Marcus Worsley, LLNL [61].

Why Study These Processes

The section above showed many examples of deposition and AM processes that are being combined with external fields to further develop their capabilities to produce parts. External fields such as acoustic, electric, and magnetic fields have been shown to enhance processes in many ways, including allowing tailored multi-material deposition, aiding in homogenizing microstructure of solidified material by moving material as it solidifies, and enhancing material deposition resolution. These all serve to further develop AM processes by increasing functionality in a part design through material and structure control. These methods can also help reduce material waste, as shown in deposition processes that use fields to ensure more of the particles or material reach their intended targets.

The recent and continuing research interest makes the development of these processes good applications for enhanced studies and potential tools for process development. This work aims to contribute to the development of these processes by studying field-driven processes numerically and experimentally which can lead to the development tools to aid in future process optimization.

1.2 Numerical Modeling in Engineering

In engineering, the concept of modeling allows for a complex system to be represented in more simplified, conceptual form which aids us to better understand the key components of a problem and decide on a solution or optimized design to achieve a specific goal. Modeling can come in many forms including physical prototypes, experimental set ups, and numerical simulations.

Utilizing numerical modeling techniques to simulate physical processes allows us to explore some of the wide possible outcomes of a physical process. These numerical models attempt to represent complex physical systems well, but are limited by the resources of how they are computed, be that a person using a pencil and paper or a large simulation run on a supercomputer. For these models to be useful, they must also reflect important factors and outcomes that are present in the real process they aim to represent - this can come in many forms, including obeying the laws of physics and constraints. These physically informed models will provide the best representation of actual systems, such as the AM systems described above.

Many of the AM processes described above, including EPD, have been developed mostly through experimental studies, which can be both time-consuming and expensive, especially when applied to AM processes which can operate with a large range of process parameters. Numerical simulations can work in conjunction with these experiments by narrowing down the potential wide range of parameters to find sets that lead to desired results. This combined approach can lead to tuned process optimization for these complex field-driven AM processes.

1.3 Motivation

This work is motivated in large part by the need to better understand and optimize the advanced manufacturing processes previously mentioned. In many instances, including in AM methods such as electrophoretic deposition, much of the development has been performed experimentally. The wide design space available in AM processes requires a large range of experiments to broadly explore what parameters make a process work well, which can be extremely time consuming and resource intensive. This presents an opportunity for models that capture the essential physics of a process to help guide this development, resulting in more limited experimental runs and more efficient optimization. This work aims to contribute towards that goal in two ways:

1. creating a framework that moves towards faster, physics-informed process simulation of field-aided AM processes, and

2. exploring the specific behaviors of additive deposition processes through simulation and preliminary experimental observation.

These faster simulations are a step towards developing *digital twins* of complex physical process; when combined with experiments, a digital twin can lead to improved results when utilizing these advanced manufacturing methods.

While the main focus of my following research will be on processes using electric fields such as EPD, the model framework will be set up to be able to incorporate other effects including additional external fields. The example framework will serve as a preliminary tool for continuing process optimization.

1.4 Dissertation Outline

This work focuses on the modeling and simulation of field-aided AM processes, as well as how we can use those models and experiments to further our understanding and development for particular applications such as particle deposition in electrophoretic deposition for producing desired crystalline structures. The rest of my dissertation is organized into the following chapters.

Chapter 2 discusses more background information on the field-driven AM processes, going into particular detail on the concept and process details of EPD. This chapter will also discuss prior work in developing EPD and show how my present research can further expand the understanding and development of EPD through both numerical simulation and experimental observation. I also discuss details on existing modeling efforts of the EPD process and the numerical methods I used for my simulation framework. Chapter 3 then takes the concepts of electric field-driven processes and presents a numerical framework for simulation. I then use my particle-based model to verify against analytical cases as development milestones before modeling deposition cases under different process parameters to observe particle behavior during deposition. Chapter 4 discusses my experimental work towards *in-situ* observation of EPD. I detail the methods used and the preliminary work towards constructing and verifying the setup for particle observation. Finally Chapter 5 provides a summary of the work and final conclusions.

Chapter 2

Background and Theory

This chapter expands upon the background and theory of some of the field-driven processes of interest in the work. I specifically discuss more details about EPD and it's application towards making colloidal crystals including prior experimental studies and modeling work focused on EPD. I also discuss more about the numerical method, the Discrete Element Method, I use in this work and why I chose it for these studies.

2.1 Systems of Interest - Particle Deposition with External Fields

This section provides more background on the AM processes of interest. These processes will focus on the deposition of particles under external electric fields and Electrophoretic Deposition (EPD) will specifically be described in detail because it is used as a direct motivating process behind the modeling and experimental work described later in Chapters 3 and 4.

2.1.1 Principles of Field-Driven AM Processes - Electrospray Deposition and EPD

As mentioned in the introduction in Chapter 1, my research presented here was motivated by and focused mainly on electric field-driven processes. The two that describe the main focus are Electrospray Deposition and EPD as introduced and shown schematically in Figure 1.2. The basic principles behind these two processes are the same, with the distinction being that Electrospray Deposition uses a nozzle to spray the particles through air while in EPD, the colloidal particles are suspended in liquid contained between electrodes. The Electrospray Deposition process described by Yan et al. deposited particles by atomizing the solution through the nozzle into particle droplets, but the concept is also the same for other techniques that spray solid particles. For the purposes of my work moving forward, I use the term electrospray as a blanket term to describe the family of processes that spray particles through air before deposition. For both electrospray and EPD, the essential process

is particles are driven through a fluid (air or a liquid) by an external electric field to deposit on an oppositely charged electrode. Figure 2.1 shows a graphic representation of the basic principle of EPD. In EPD, the particles suspended in the liquid develop an effective surface charge and move towards the oppositely charged electrode when the electric field is applied.

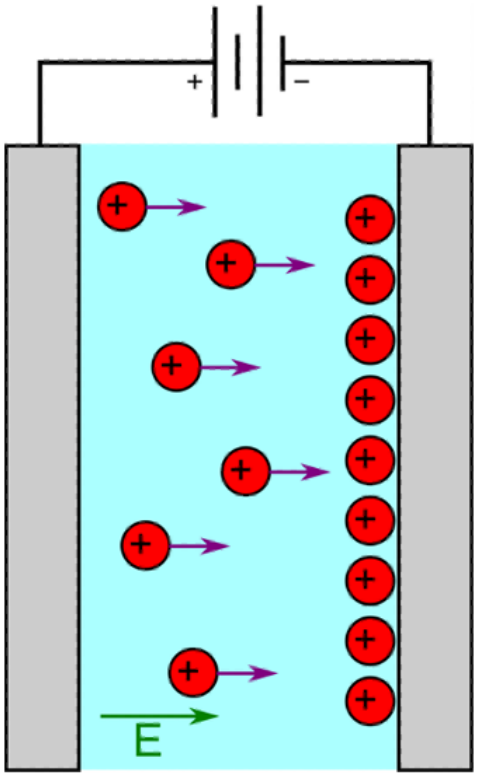

Figure 2.1: Graphic showing the basic principles of EPD. The positively charged particles move through the suspension towards the negatively charged electrode due to the applied electric field.

While Figure 2.1 shows particles moving in a quiescent fluid, variations of EPD can also have the liquid injected into the cell during deposition to add more particles or particles of different materials.

The EPD process has several advantages in forming depositions and components like colloidal crystals. The process has been shown to be quick, creating full deposits or components in the order of seconds and minutes [42], and scalable, able to create deposits potentially up to square meters if the electrodes are large enough [30]. The effective surface charge that develops on the colloidal particles also allows different materials including metals, polymers, and ceramics to be used [7] [53] and multiple materials can be deposited to further expand component design capabilities [44]. These advantages make EPD a good choice of process for making colloidal crystals as described in Chapter 1.

Why use field-driven AM processes?

Field-driven AM processes like EPD are particularly good choices of methods for creating components that may require a tailored microstructure such as colloidal crystals. They can be made of different materials, even multiple if desired, be created quickly over a large area as needed, and reduce material waste due to more particles reaching their intended targets. Using colloidal crystals as an example, we can see the benefits of using a process like EPD compared to other processes such as sedimentation [1], evaporation [48], or layer-by-layer assembly [18] which can be time intensive.

Another of the main benefits of using these processes is the controllable geometry and structure of the deposit. An example of this is shown in Figure 2.2.

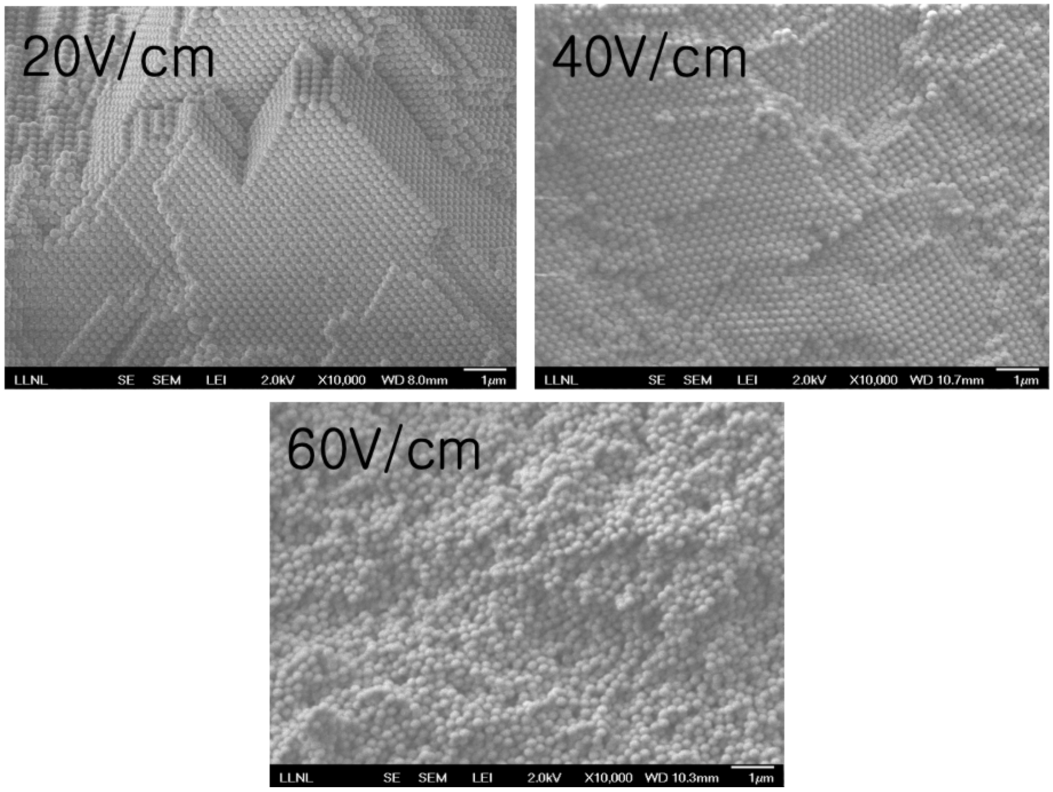

Figure 2.2: Micrographs of deposits made with EPD, courtesy of Dr. Marcus Worsley, LLNL [61]. As the applied electric field strength increases, the structure becomes less crystalline and more amorphous.

The micrographs shown in Figure 2.2 show the effect of adjusting the electric field strength in EPD on the resulting deposit structure [61]. In the upper left panel, labeled with the electric field strength of $20\frac{V}{cm}$, the deposit appears crystalline with large grains. As the electric field strength further increases in the upper right and bottom panels, the structure

transitions to be less organized and more amorphous. Depending on the level of crystallinity desired for the end component, the electric field strength can play a significant factor.

2.1.2 EPD Background - Brief History and Process Development

The phenomenon of EPD was first observed when clay particles moved through water due to an applied electric field as studied by Ruess in 1808 [7]. It was then developed in industry starting in the 1930's and continued to be used for depositing a variety of materials. Early studies into the kinetics of EPD to understand how much mass was deposited were performed by Hamaker, who observed linear dependence of the deposited weight with the amount of charge passed through the process [25]. The linear model proposed by Hamaker is described by the Hamaker Equation [19]:

$$m(t) = C_s \mu A E t f \tag{2.1}$$

where $m(t)$ is the mass of the deposit as a function of time t, C_s is the suspension concentration, μ is the electrophoretic mobility, A is the deposition area, and f is a "sticking parameter" analogous to the efficiency of the deposit where $f = 1$ if all particles are deposited and $f = 0$ if none incorporate into the deposit. This factor is generally determined emperically for a specific EPD process [19].

Generally, EPD kinetics are determined by weighing deposits after specified amounts of deposition time, and the morphology of the structures are investigated with imaging via an SEM. These techniques are performed *ex-situ* and do not give direct insight into the particle-particle interactions as the deposit forms. This is one of the motivating factors for my work - to further understanding of particle kinetics through *in-situ* observation. Details on this are described in Chapter 4.

2.1.3 EPD Modeling - Prior Work

Following on the studies of Hamaker, most modeling work around EPD provides a continuum approach to investigate the thickness or overall shape of deposits [19]. Kinetic models predicting how the mass of the deposit forms over time following similar strategies as Hamaker's model above in Equation 2.1 have been used to incorporate additional effects such as changes in suspension concentration C_s, and different EPD processing conditions, such as constant-current and constant-voltage configurations [54].

These kinetic models are mostly used for determining bulk mass deposited, and are able to be solved analytically for cases such as infinite planes and concentric cylinders. More recent studies have investigated the shape of deposits due to more specific geometries of electrodes. While still from a continuum domain, these models begin to look at the overall morphology of the deposits . Most models have used methods such as the Finite Element Method (FEM) or Finite Difference Method to simulate particle transport through the fluid towards the electrode. Pascall et al. studied the morphology of deposits on strip electrodes using FEM as shown in Figure 2.3 below.

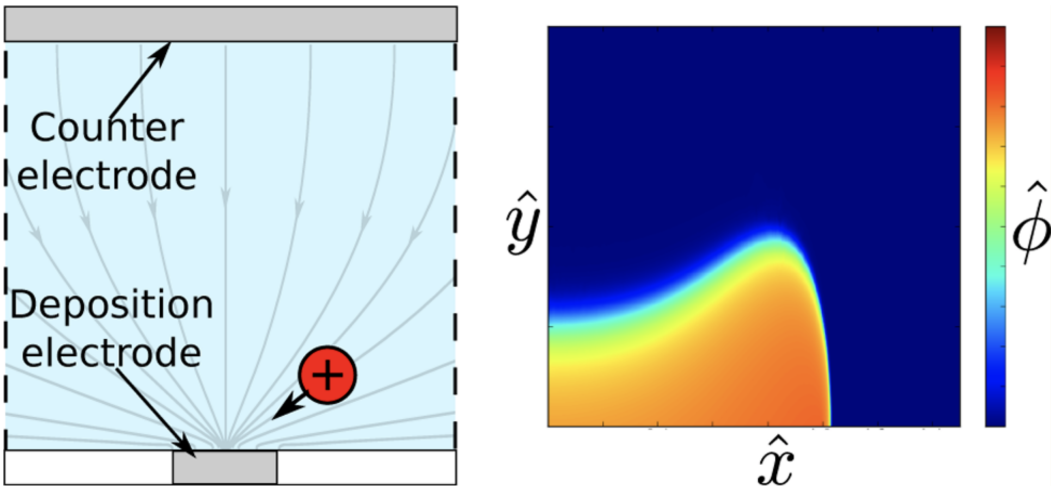

Figure 2.3: FEM simulation results from Pascall et al. investigating the morphology of EPD deposits on electrodes with corners and edges [43].

Other recent examples include work by Braun et al. where they used FEM to study the deposition of copper in through-silicon vias [12] and simulations by Verma et al. who used FDM to simulate paint depositions on car bodies [59]. As shown in Figure 2.3, these types of models are well suited to investigate overall deposit shape, but do not account for particle-particle interactions or give details on the crystallinity of the structure.

Direct particle-based modeling of EPD has more recently been investigated by Giera et al. to study these interactions more closely and lead to simulation tools that can help predict structure of the deposit [22] [23]. The model uses a direct particle representation accounting for hydrodynamic interactions with the fluid, particle-particle and particle-wall interactions due to electrostatic and steric repulsion and van der Waals attraction, and electrophoretic motion due to the applied electric field. Their model is implemented in the Large-scale Atomic/Molecular Massibely Parallel Simulator (LAMMPS) and used a high performance computing system to perform the simulations [23]. An example of the visualizations from the Giera et al. model is shown in Figure 2.4.

This work by Giera et al. represents a high resolution model and one of the first direct particle-based models used to study deposits made through the EPD process. Their model simulated 15000 particles over a deposition time on the order of milliseconds. This early work is another motivating factor in my present research as this shows an availability for increased study in direct particle models of EPD, and with particular focus on expanding the field's capabilities with respect to process parameters and working towards full scale simulation. As a full scale deposition is performed on the order of seconds or minutes, working towards expanding modeling capabilities approach these regimes is desirable. This leads to one of the driving goals of my research to present a simpler model framework that can simulate

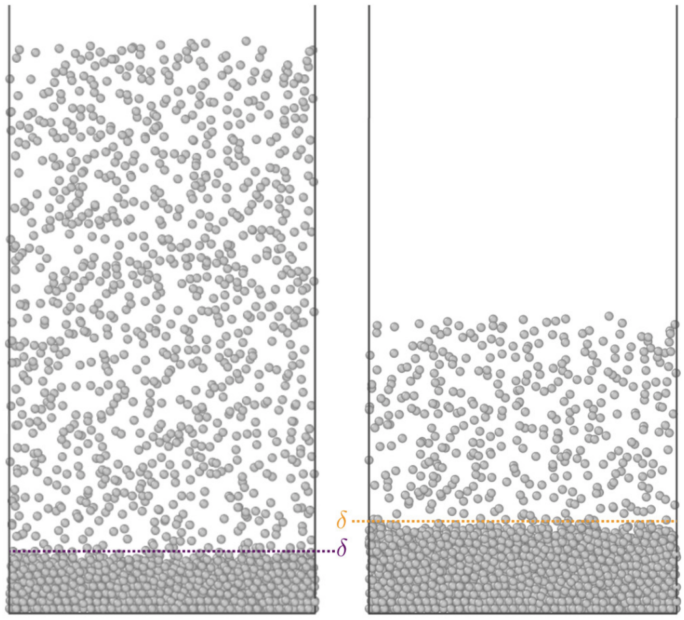

Figure 2.4: Simulation results from Giera et al. showing a particle deposit form through EPD where δ is the deposit height [23].

multiple processes, but that can be applied to EPD and works in the direction of expanding on those capabilities and comparing it to the present standard set by Giera et al. My model will be discussed more in Chapter 3.

2.2 Numerical Methods - Discrete Element Method (DEM)

To work towards my goal of presenting a simulation framework that can be applied to a range of field-driven AM processes including electrospray and EPD, I have chosen to use the Discrete Element Method (DEM).

2.2.1 Intro to DEM

The Discrete Element Method was originally introduced as the "distinct element method" in 1979 by Cundall and Strack [16] and has been used extensively since then to model a wide variety of particle-based systems in many fields that deal with granular media [24]. The basic principle of DEM is a direct representation of particles that interact with the environment and each other through interaction forces. The forces on each particle can be computed, resulting in a total force, and by using Newton's equations of motion, the trajectories of the particles through time can be computed. Solving the general $F = ma$ equation for each

particle will result in descriptions of their motion through the simulation. Many different forces can be accounted for using DEM, including those imparted by physical contact with other particles and boundaries, non-contact forces due to drag with surrounding fluids or interactions with external fields like acoustic, electric, and magnetic fields as used in the AM processes described above.

2.2.2 DEM for My Model

I have chosen to use DEM for my simulation framework for several reasons:

- Direct particle representation allows for analysis of the deposit structure
- The general framework allows for the introduction of many forces
- The method is well established in literature for simulation of similar systems and can be combined with other methods for representing multiphysics problems

One of the main goals of my research is use this framework to be able to evaluate the structure of a deposit and observe how the particles interact. This direct representation of the particles is well set up to achieve that goal as I will be able to discretely track each particle through time.

The general framework of DEM allows it to be module in the way forces are applied. When computing the total force, the definitions of separate forces can be implemented as separate functions so the relative complexity of the physics affecting the particles can be chosen for the particular situation. Another goal of my work is to make the framework as simple as possible to work towards a "digital twin" of these AM process, so the ability to start with simple cases and expand the forces involved as necessary is very beneficial.

Since its inception, DEM has been used for many different applications spanning different physical systems. It has been shown to be used for physical systems similar to those of interest in my work, including deposition processes under magnetic fields [39] and electric fields [38], and colloidal systems [10]. It has also been combined with other methods to incorporate additional physics. Additional factors such as h considerations and two-way coupled interactions with fluids can be combined with DEM representations for particles using methods like FDM to compute temperature or the fluid velocity fields [67] [21]. These exemplify methods to build up multiphysics simulations for "digital twins" of AM processes.

My work aims to use this established method to study the field-driven AM processes in a general framework that can be used as a starting point expanded as a useful tool for further process development. Building upon this prior work around these AM processes, I detail my simulation framework and preliminary experimental work in the following chapters.

Chapter 3

A Numerical Study on Deposition

In this chapter, I discuss a numerical model framework that I use to study field-driven AM process, specifically those with a powder or particle deposition step. To study that deposition, I will first describe a model using DEM and implemented in Python. The framework of the model and physics included are described before investigating the framework more with several numerical studies. I use this framework to study different cases of processes with varied parameter scales to show it's potential as a process development tool.

3.1 Motivation

For further development and understanding of these field-driven processes, modeling can used to explore wide ranges of parameters that might be difficult or expensive to study purely with experiments. Using simulations to guide the experimental parameters of interest, and using well designed experiments to further validate the models will lead to the best results towards developing well understood processes. As I previously mentioned in Chapter 2, there have been some modeling efforts towards simulating EPD, but many of those have looked at it through a continuum lens. These approaches can provide insight on the overall deposit shape and deposit density, but may not necessarily capture the microstructure details that can lead to an understanding of the crystallinity or order of the deposits that are important for the end application like colloidal crystals. DEM is a method that can provide information on individual particle motion and allow studies aimed at understanding the microstructure, so that will be my chosen method. This direct representation of the particles will be helpful in comparing with the prior work performed by Giera et al. on depositions from a more simplified framework as well as be a tool for comparison with experimental work as described later [22] [23].

Goals of Model

The main goal of this simulation work is to provide a framework that can be used as a potential development tool for optimizing field-driven AM processes such as electrospray and EPD in a simple implementation that can be run on a laptop that does not require large computational resources. These direct particle simulations will also provide particle trajectories under varied parameters which can be used to compare with existing models and particle tracking experiments. In particular, this simulation framework can be used to further develop the EPD community's work towards understanding the process kinetics where the prior work is mostly performed with more computational intensive frameworks. The simulation framework is designed to produce particle trajectories that allow for the study of how they move due to the physics of the field-driven AM processes and can be directly informed by experiments that also provide particle trajectories, such as those described below in Chapter 4. In summary, the goals of this work are:

1. Provide a simulation framework capable of being run on a laptop to study field-driven AM processes with a range of parameters.

2. Compare the simulation framework results against analytical solutions and explore how a variety of process parameters effect the resulting depositions.

The work I describe below works towards these goals through several studies used as milestones of the simulation framework development. While I made progress towards exploring different depositions, there are several directions for future studies of immediate interest, namely studying more parameters similar to the EPD process. The examples I discuss show the capabilities of this simple framework designed to run on smaller computational resources than previous work. This can be used as a starting point and serve as an example for the results that can be achieved with this framework.

3.2 Methodology

This section will describe the particle model framework used for the majority of the work described in this dissertation. I used a DEM formulation to represent the particles in 3D and will describe the forces included in my model framework to capture the physics seen in processes including electrospray and EPD. Due to the types of collisions I expect to see in these simulations, I implemented an explicit time stepping scheme, however implicit iterative schemes may also be potentially used as in other DEM models, but that exploration is currently left for future studies [66].

3.2.1 Discrete Element Framework

For this model framework, I begin with the familiar $F = ma$ equation that is the basis for the equation of motion for the DEM particles mentioned previously in Chapter 2. More

specifically, this equation written for a single particle will be denoted as:

$$\boldsymbol{F}^{Total} = m\ddot{\boldsymbol{r}} \tag{3.1}$$

where $\boldsymbol{F}^{Total}$ is the summation of all forces applied to the particle, m is the particle mass, and $\ddot{\boldsymbol{r}}$ is the second time derivative of the particle position, or the acceleration. The overall strategy of this model is to choose the forces to model the physics of the field-driven AM processes, compute those for each particle, and then simulate particles in time to see how that affects the deposition. At the highest level, the basic steps in this model are:

1. Initialize Particles
2. For each timestep:
    a) Compute total force on each particle
    b) Compute acceleration
    c) Step forward in time and compute new particle velocities and positions
3. Repeat until end of simulation
4. Analyze trajectories

I describe the forces involved in more detail in the following sections, but they will include interactions between the particles and the fluid, particles and the driving field, particles with other particles, and particles and the boundaries. An overall schematic of the model problem is shown below in Figure 3.1 below. The driving field in my problem of interest is an electric field, denoted by E in the figure, but the framework could be expanded to include others that are also employed in AM processes such as magnetic and acoustic as in processes described in Chapter 2 [29] [65] [26].

The inputs to the model will then be parameters describing the particles themselves such as material and size, parameters describing the environment including fluid material properties such as viscosity, domain dependent properties such as the boundary conditions, and time parameters for the time stepping scheme. These will be discussed more in detail in further sections about the forces and specific numerical studies. The output from the model will be the particle positions overtime, or trajectories. I analyze the trajectories in the different numerical studies described below to understand how these particles move and, in the last studies, how they incorporate into a deposit. The results from my modeling work show examples of how this framework can potentially be used for process development and optimization of field-driven AM processes such as electrospray and EPD.

3.2.2 Physics Model Formulation for Field-Driven AM

The basic situation captured in this framework can be summarized as particles in a fluid, being driven by an external electric field towards a substrate where they form a deposit. To

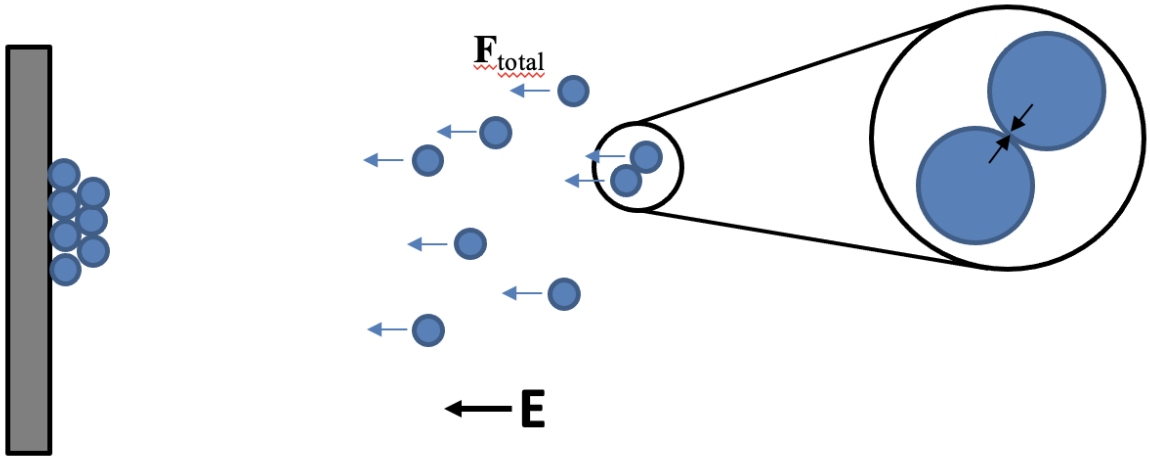

Figure 3.1: Overview graphic of the model problem approached with this simulation showing some of the forces and interactions that the particles will see with the driving field (E) and with other particles via near-field and contact as they deposit on the substrate.

capture this essential base situation, the forces considered will include particle-fluid interactions, particle-field interactions, particle-particle interactions, and particle-wall interactions. The forces and boundary conditions used in the framework are discussed in further detail below.

For the AM processes I am interested in studying with this model framework, I make several simplifying assumptions. The main assumptions are as follows:

- Particles are sufficiently small, so particles will be idealized as spheres and rotation will be neglected.
- The external electric field is constant, and unaffected by the moving particles.
- The particles are affected by drag from the fluid, but do not affect the fluid in a one-way coupled system.
- Contact area is small compared to the particle size.
- Contact results in small strains, well within the elastic limit of the particle and wall material.

When formulating this model, I aimed to start with a simple framework which could then be expanded to capture additional effects. The simplifying assumptions listed above capture that essence and enable the model framework to be developed with the tradeoff of accuracy in the form of both resolution and complexity, for simplicity in model development

and speed. Some of the next levels of complexity, including addressing the assumption of the one-way coupled system will be addressed in the future work section.

Forces used in the Model

This section will define all the forces used when computing $\boldsymbol{F}^{Total}$ for the particles. Starting with the external, environmental forces, we have effects that apply to every particle independent of interactions with other particles. These are effects from drag with the surrounding fluid, gravity, the Lorentz driving force, and the browning force from collisions with the fluid molecules. Next, the interaction forces are considered. These include the forces between multiple particles as well as particles and the wall, namely contact and dissipation, friction, bonding, and nearfield forces.

Drag Force First we'll discuss the drag force imparted on the particle by the surrounding fluid. I represent the drag force with the generalized drag model [67] [41]:

$$\boldsymbol{F}^{Drag} = \frac{1}{2} C_D A_c \rho_f \|\boldsymbol{v}_f - \boldsymbol{v}_p\|^2 \boldsymbol{\tau} \tag{3.2}$$

where C_D is the drag coefficient, $A_c = \pi R_p^2$ is the characteristic area for our spherical particles, ρ_f is the density of the surrounding fluid, $\boldsymbol{v}_f$ and $\boldsymbol{v}_p$ are the respective fluid and particle velocities, and $\boldsymbol{\tau}$ is a unit vector defining direction of drag force as shown below:

$$\boldsymbol{\tau} \equiv \frac{\boldsymbol{v}_f - \boldsymbol{v}_p}{\|\boldsymbol{v}_f - \boldsymbol{v}_p\|} \tag{3.3}$$

In most cases I used my model to investigate, the surrounding fluid was quiescent with a $\boldsymbol{v}_f = \boldsymbol{0}$, but the framework can be used for more general situations where the fluid has a known velocity.

The drag coefficient, C_D, is generally a function of the Reynolds number (Re). Reynolds number can be computed by:

$$Re = \frac{2 R_p \rho_f \|\boldsymbol{v}_f - \boldsymbol{v}_p\|}{\mu_f} \tag{3.4}$$

where μ_f is the absolute viscosity of the surrounding fluid. As can be seen, the Reynolds number is directly proportional to particle size, fluid density, and relative velocity of the particle and the fluid, and inversely proportional to the fluid viscosity. For colloidal particles in a solvent such as in the case of EPD, the Re are usually low, as characterized by Stokes flow [53].However, I intended this framework to be used for a variety of processes and a process like electrospray in air may have a much higher range of Re. To account for the possible wide range, I employed a piecewise empirical relation for the drag coefficient from Biringen and Chow [9]:

$$C_D = \begin{cases} \frac{24}{Re} & 0 < Re \leq 1 \\ \frac{24}{Re^{0.646}} & 1 < Re \leq 400 \\ 0.5 & 400 < Re \leq 3 \text{ x } 10^5 \\ 0.000366 Re^{0.4275} & 3 \text{ x } 10^5 < Re \leq 2 \text{ x } 10^6 \\ 0.18 & 2 \text{ x } 10^6 < Re \leq \infty \end{cases} \tag{3.5}$$

Gravity Gravity is the simplest of all forces used in this model to implement. Using a cartesian coordinate system, the force is enacted in the z direction, denoted here as $\boldsymbol{e_3}$ and causes a constant acceleration defined by the gravitational constant, g. The gravitational force on a particle is defined as:

$$\boldsymbol{F}^{grav} = mg\boldsymbol{e_3} \tag{3.6}$$

where m is the mass of the particle and the gravitational constant $g = 9.81\frac{m}{s^2}$.

Lorentz Force The field-driving force in my model framework is expressed by the classical Lorentz force. This force describes the force experienced by a charged particle moving through an external applied electromagnetic field. The Lorentz force can be defined as [39]:

$$\boldsymbol{F}^{Lorentz} = q\left(\boldsymbol{E} + \boldsymbol{v}_p \times \boldsymbol{B}\right) \tag{3.7}$$

where q is the charge of the particle, $\boldsymbol{E}$ is the applied electric field, and the term $\boldsymbol{v}_p \times \boldsymbol{B}$ is the cross product of the particle velocity and the applied magnetic field $\boldsymbol{B}$. For my cases, the magnetic component is not utilized as I am interested in looking at applied electric fields. As this is a framework, the potential to add that component is still used. For this framework, I am assuming that any induced magnetic field due to the motion of the charged particles is small, and the force is dominated by the externally applied electric field. So for my cases presented below, the Lorentz force will be expressed as (with a magnetic field component of $\boldsymbol{B} = \boldsymbol{0}$:

$$\boldsymbol{F}^{Lorentz} = q\boldsymbol{E}$$

Brownian Force The Brownian Force on the particles describes the random force from collisions with surrounding fluid molecules resulting in Brownian motion. The definition I use in my model was derived from the Langevin equation as presented by Russel, Saville, and Schowalter [53]. The derivation approximates the random collisions that occur on the time scale of molecular motions from fluid molecules as rapid fluctuations defined to be random in magnitude and direction and uncorrelated on the time scale of particle motion.

For my model, this takes the form of:

$$\boldsymbol{F}^{Brownian} = \sum_{i=1}^{3} F_i^b \boldsymbol{e_i} \tag{3.8}$$

where the three cartesian components of the force vector are defined with magnitude F_i^b. For each force component, we have:

$$F_i^b = G_i \sqrt{12\pi\mu_f R_p k_B T} \tag{3.9}$$

where T is the temperature and k_B is the Boltzmann constant. G_i is a Gaussian random number that has a mean of 0 and a variance of 1. This force in particular plays a large role in the first verification trial discussed below when I discuss studying particle diffusion with this model.

Normal Contact, Dissipation, and Bonding Forces For many of the interaction forces, I will be following an approach presented by Zohdi [66]. To begin with the first interaction forces, I will look at the normal contact and dissipation forces. This approach uses a simplified model where the contact force is proportional to the normalized overlap. To begin, we have two particles i and j. To determine if they are in contact, we first look at their relative positions to check if the distance between them meets the criteria for contact. If center distance between the particles is smaller than the sum of their radii, mathematically shown below in Equation 3.10, then they are in contact and we can define the overlap, δ_{ij} as shown below in Equation 3.11.

$$\|\boldsymbol{r}_i - \boldsymbol{r}_j\| \leq R_i + R_j \Rightarrow \text{Particles are in contact} \tag{3.10}$$

$$\delta_{ij} = |\|\boldsymbol{r}_i - \boldsymbol{r}_j\| - (R_i + R_j)| \tag{3.11}$$

where R_i and R_j are the radii of Particle i and Particle j. This is graphically shown in the left panel of Figure 3.2 below.

Now we can define the contact force between particles as:

$$\boldsymbol{F}_{ij}^{contact,n} = -K_{pij}|\varepsilon_{ij}|^{p_p}\boldsymbol{n}_{ij}A_{ij}^c \tag{3.12}$$

where K_{pij} is a particle-particle contact compliance constant and p_p is a material deformation parameter. In practice, these material parameters could be determined empirically [66]. ε_{ij} is a normalized *strain-like* deformation metric defined as:

$$\varepsilon_{ij} = \left| \frac{|\|\boldsymbol{r}_i - \boldsymbol{r}_j\| - (R_i + R_j)|}{(R_i + R_j)} \right| = \frac{\delta_{ij}}{(R_i + R_j)} \tag{3.13}$$

The vector $\boldsymbol{n}_{ij}$ is the unit normal vector between the particle centers and points from particle i to particle j. It is defined as:

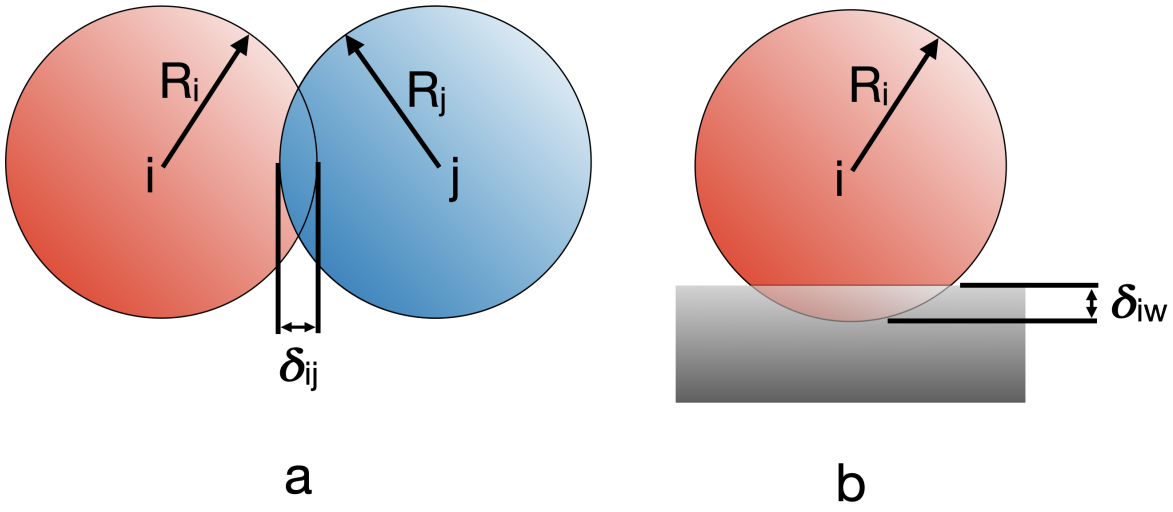

Figure 3.2: Graphic representation of particle contact. a) Particle-particle contact with overlap δ_{ij}. b) Particle-wall contact with overlap δ_{iw}.

$$\boldsymbol{n}_{ij} = \frac{\boldsymbol{r}_j - \boldsymbol{r}_i}{\|\boldsymbol{r}_i - \boldsymbol{r}_j\|} \tag{3.14}$$

Finally, the contact area parameter, A_{ij}^c, is defined as:

$$A_{ij}^c = \pi(R_i^2 - L_i^2) \tag{3.15}$$

where:

$$L_i = \frac{1}{2}\left(\|\boldsymbol{r}_i - \boldsymbol{r}_j\| - \frac{R_j^2 - R_i^2}{\|\boldsymbol{r}_i - \boldsymbol{r}_j\|}\right) \tag{3.16}$$

Phenomenological particle contact dissipation essentially dampens the contact force defined in Equation 3.12. The dissipation is a function of the difference in normal velocities of the particles and is defined as:

$$\boldsymbol{F}_{ij}^{dissipation} = c_{cd}(\boldsymbol{v}_{j,n} - \boldsymbol{v}_{i,n})A_{ij}^c \tag{3.17}$$

where c_{cd} is a contact damping parameter which in practice would be determined empirically, and $\boldsymbol{v}_{i,n}$ and $\boldsymbol{v}_{j,n}$ are the normal velocities of the particles i and j. The normal components of the velocity of a particle i can be computed using the vector dot product with a unit normal vector $\boldsymbol{n}_{ij}$ as follows:

$$\boldsymbol{v}_{i,n} = (\boldsymbol{v}_i \cdot \boldsymbol{n}_{ij})\boldsymbol{n}_{ij} \tag{3.18}$$

For the last normal force, we look at bonding between the particles. For an attractive normal bond to occur, I use a critical normalized deformation metric, ε^*, as a user-defined parameter. If the particles in contact meet the criteria of $|\varepsilon_{ij}| \geq \varepsilon^*$, the normal bond is activated following the definition:

$$\boldsymbol{F}_{ij}^{bond,n} = K_{ij}^{nb}|\varepsilon_{ij}|^{p_b}\boldsymbol{n}_{ij}A_{ij}^{c} \tag{3.19}$$

This force takes the same for as the normal contact force in Equation 3.12 with the normal bonding parameter K_{ij}^{nb} and the bonding law exponent p_b also being determined experimentally in practice. The normal bonding force is also noted to be active in the opposite direction of the contact force. When active, the interplay between both forces and their effect on the particle dynamics will be determined by the parameters used.

Tangential Contact Forces - Friction and Bonding Continuing with the contact forces, we have forces acting in the tangential direction. The two main tangential contact forces for my particle model will be friction and a tangential bonding force. For friction, I use a regularized stick-slip friction model following Zohdi [66]. The friction model first checks the static friction threshold at the contact point, $\mu_s\|\boldsymbol{F}_{ij}^{contact,n}\|$, and then utilizes either a stick or slip condition. The piecewise definition for friction is applied as follows:

$$\boldsymbol{F}_{ij}^{friction} = \begin{cases} K^f\|\boldsymbol{v}_{j,\tau} - \boldsymbol{v}_{i,\tau}\|A_{ij}^{c}\Delta t\boldsymbol{\tau}_{ij} & K^f\|\boldsymbol{v}_{j,\tau} - \boldsymbol{v}_{i,\tau}\|A_{ij}^{c}\Delta t < \mu_s\|\boldsymbol{F}_{ij}^{contact,n}\| \\ \mu_d\|\boldsymbol{F}_{ij}^{contact,n}\|\boldsymbol{\tau}_{ij} & K^f\|\boldsymbol{v}_{j,\tau} - \boldsymbol{v}_{i,\tau}\|A_{ij}^{c}\Delta t \geq \mu_s\|\boldsymbol{F}_{ij}^{contact,n}\| \end{cases} \tag{3.20}$$

where K^f is a tangential contact friction compliance constant, in practice determined empirically, Δt is the time step used in the simulation, and μ_s and μ_d are the static and dynamic friction coefficients, respectively. $\boldsymbol{F}_{ij}^{contact,n}$ is computed using Equation 3.12 above. $\boldsymbol{v}_{\tau i}$ and $\boldsymbol{v}_{\tau j}$ are the tangential velocities of the particles i and j. They can be computed by subtracting the normal component of the particle velocities from the full velocity vector as shown:

$$\boldsymbol{v}_{i,\tau} = \boldsymbol{v}_i - \boldsymbol{v}_{i,n} \tag{3.21}$$

where the normal component is defined in Equation 3.18.

The unit vector $\boldsymbol{\tau}_{ij}$ is defined by the tangential velocity components at the contact point as shown:

$$\boldsymbol{\tau}_{ij} = \frac{\boldsymbol{v}_{j,\tau} - \boldsymbol{v}_{i,\tau}}{\|\boldsymbol{v}_{j,\tau} - \boldsymbol{v}_{i,\tau}\|} \tag{3.22}$$

If the static friction threshold is not met, as in the first part of the piecewise friction model in Equation 3.20, the force is defined as a stick model. The second part is enforced when the static threshold is met or exceeded, and a slip model is applied.

Finally, if a bond is activated as above in Equation 3.19, another rotational bond which acts in the tangential direction is activated. This bond force takes the form of:

$$\boldsymbol{F}_{ij}^{bond,r} = K_{ij}^{rb}\|\boldsymbol{v}_{j,\tau} - \boldsymbol{v}_{i,\tau}\|A_{ij}^{c}\Delta t\boldsymbol{\tau}_{ij} \tag{3.23}$$

where K_{ij}^{rb} is a rotational bonding parameter, which in practice is empirically determined. This force is again only applied if the bond is active and there is also a corresponding normal bond force applied. The tangential rotational bond force is in the same direction as the tangential stick friction force denoted in the first part of Equation 3.20, so both will work together to resist tangential motion.

Wall Contact Forces The previous contact forces starting with Equation 3.10 were defined for contact between particles. As I am using this framework to investigate deposition processes, the particles will also interact with a substrate, or wall. For my studies, I use the bottom boundary as a solid wall and the particles will interact with that wall using basically the same forces including normal contact, dissipation, bonding, and tangential friction and bonding. In these cases, the wall will take the place of Particle j. It is assumed to be large and stationary, resulting in a "radius" $R_w \to \infty$ and a velocity $\boldsymbol{v}_w = \boldsymbol{0}$ using the subscript w to denote the wall. I use the bottom surface as the wall, so the normal direction for $\boldsymbol{n}_{iw}$ will always be in the z or $\boldsymbol{e}_3$ direction and the tangential direction for friction and tangential bonding will be in the $x-y$ or $\boldsymbol{e}_1-\boldsymbol{e}_2$ plane. The surface of the wall defines the plane where $z = 0$, so a particle is in contact with the wall if the z component of its position $\boldsymbol{r}_i$ is less than the radius R_i and the penetration δ_{iw} is measured as shown in the right panel of Figure 3.2. With those adjustments, the Equations 3.10 through 3.23 are used in the same way to compute particle-wall contact interaction forces.

Near-Field Interaction Forces One more class of interaction forces between particles are the near-field forces. These are applied when the particles are close, but not related to contact. One example of this forces is repulsion of like-charged particles. For this model, I follow Zohdi and use a simple form to capture effects from attractive and repulsive near-field forces [66]:

$$\boldsymbol{F}_{ij}^{NF} = \sum_{j\neq i}^{N_p}\left(\underbrace{\alpha_{1ij}\|\boldsymbol{r}_i - \boldsymbol{r}_j\|^{-\beta_1}}_{\text{attraction}} - \underbrace{\alpha_{2ij}\|\boldsymbol{r}_i - \boldsymbol{r}_j\|^{-\beta_2}}_{\text{repulsion}}\right)\boldsymbol{n}_{ij} \tag{3.24}$$

where α_1, α_2, β_1, and β_2 are empirical material parameters. There are various decompositions used for these parameters such as those based on mass, surface area, and volume, but the main one I use in this model is charge-based:

$$\alpha_i j = \bar{\alpha}_{ij} q_i q_j \tag{3.25}$$

where $\bar{\alpha}$ will be the material parameter I use in the model.

In Equation 3.24, the sum includes all particles $j \neq i$, which is a more rigorous definition and at high number of particles N_p, this will become quite computationally expensive. These forces are inversely proportional to the distance between particles, so as the particles are further apart, the forces decrease. I employ an effective cutoff distance for computing these near-field forces to neglect interactions with those particles that are far enough away similar to a strategy used by Giera et al. [23]. This cutoff distance is a user-controlled parameter that is system dependent in practice.

Total Force on a Particle Now that all the individual force components are defined above, I combine them to compute the total force on each particle. Using Equations 3.2 through 3.25 total force on Particle i is now defined as:

$$\begin{aligned}\boldsymbol{F}_i^{Total} =& \boldsymbol{F}_i^{Drag} + \boldsymbol{F}^{grav} + \boldsymbol{F}_i^{Lorentz} + \boldsymbol{F}_i^{Brownian} \\ &+ \sum_{j \neq i}^{N_p} \left(\underbrace{\boldsymbol{F}_{ij}^{contact,n} + \boldsymbol{F}_{ij}^{dissipation} + \boldsymbol{F}_{ij}^{bond,n} + \boldsymbol{F}_{ij}^{friction} + \boldsymbol{F}_{ij}^{bond,n} + \boldsymbol{F}_{ij}^{NF}}_{\text{Particle-Particle Interactions}} \right) \\ &+ \underbrace{\boldsymbol{F}_{iw}^{contact,n} + \boldsymbol{F}_{iw}^{dissipation} + \boldsymbol{F}_{iw}^{bond,n} + \boldsymbol{F}_{iw}^{friction} + \boldsymbol{F}_{iw}^{bond,n}}_{\text{Particle-Wall interactions}}\end{aligned} \tag{3.26}$$

where the particle summation terms are formally stated to account for all particles, but contact, dissipation, friction, bond, and near-field forces are only activated under certain conditions specified in their definitions above. This is then used with Equation 3.1 for each particle in the system to solve for velocities and positions throughout the simulation.

Boundary Conditions

For this simulation framework, the boundary conditions of the domain had to be defined to allow particles to deposit on a substrate and start to stack to build up layers. I chose the bottom surface to represent the substrate with a solid boundary with force interactions described above. The top surface is open, and that is where the particles are generated. To investigate depositions such as those found in EPD, the number of particles can grow extremely large. I chose not to attempt a full scale simulation since the code framework is intended to be run quickly on a laptop. To keep the number of particles in the simulation in a good range for my framework, but also be able to investigate behavior of stacking particles in a deposit structure, I used periodic boundary conditions for the side boundaries. This assumes the domain is now a representative volume element (RVE) of the domain near the substrate. Essentially the periodic boundaries allow the particles near one side of the boundary to exit and re-enter on the other side with the same velocity. The boundary conditions are shown graphically in Figure 3.3 below. While they are shown in 2D, the same

periodic boundary condition were applied to the boundaries perpendicular to those shown (into and out of the page), forming a 3D rectangular domain.

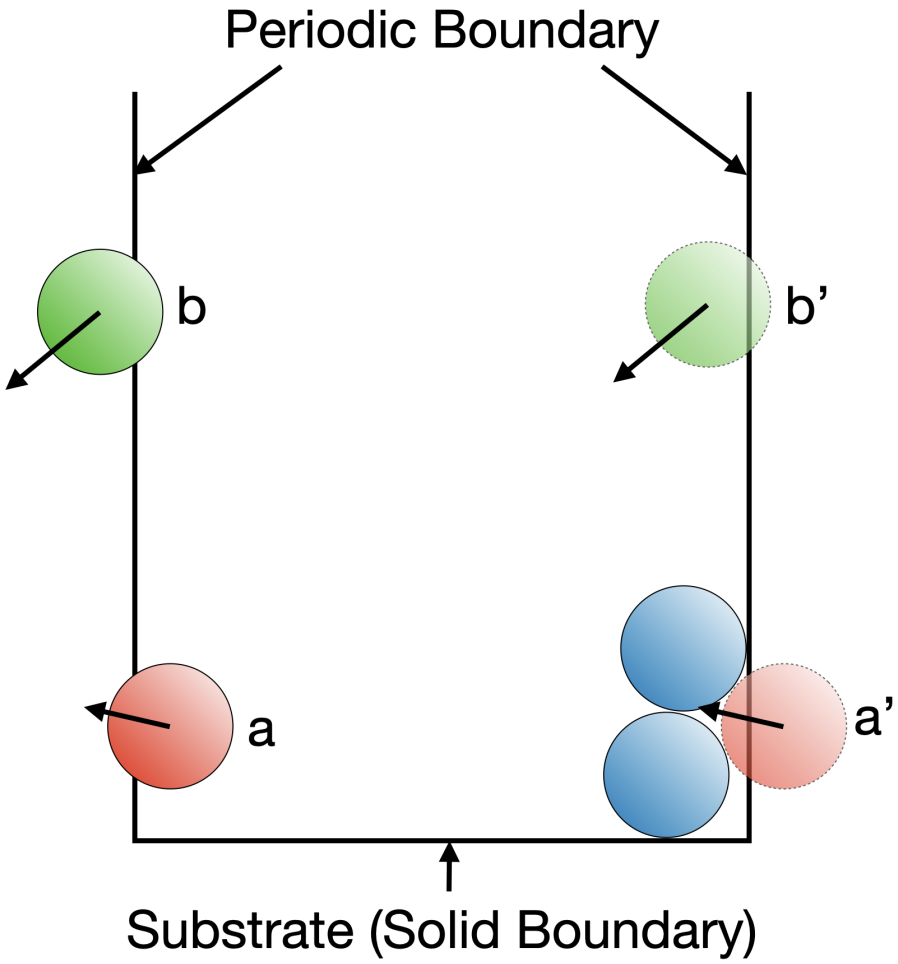

Figure 3.3: Graphic representation of the boundary conditions used in the model framework. Two scenarios are shown: 1) Particle (a) has partially crossed the left boundary and interacts with the blue particles near the right boundary as if it were in the position of Particle (a'). 2) Particle (b) crosses the left boundary completely and re-enters the right boundary with the same velocity, represented as Particle (b').

For the periodic boundaries on the four sides, the $\pm x$ and $\pm y$ using a Cartesian coordinate system, there are two main situations in which particles need special treatment near the boundary. The two situations are depicted in Figure 3.3 and are described by:

1. Particle edge crosses boundary.
2. Particle center crosses boundary.

In the first situation, a particle edge crosses a boundary, but the center is still within the domain. In the figure, situation one is shown by the red Particle a and Particle a'. We see Particle a is positioned so it's center is within the domain, but it's edge has crossed the left boundary. The arrow denotes its velocity. Since its edge has crossed the periodic boundary, it interacts with the blue particles near the right boundary as if it were in the position of Particle a'. When computing the total forces on Particle a, I use a "ghost particle", denoted Particle a'. This ghost particle then interacts with the blue particles and the sum of those interactions is added to the total interactions for Particle a.

The second situation concerns particles that fully cross a boundary. For this criteria, I considering situation 2 by using the center position of the particle as a reference. Again looking at Figure 3.3, when the center position of Particle b crosses the left boundary, the particle position will be moved to the position of Particle b', maintaining the same velocity. In my code, I implement this condition at the beginning of a time step while looping through the particles before computing forces. It is possible that both conditions occur for a particle, such as in the figure. Since Particle b' still has it's edge over the right boundary, it is possible that it interacts with particles near the left boundary. These will be considered when computing total forces on Particle b after adjusting its position to that of Particle b'.

3.2.3 Time Stepping Scheme

This section will discuss the time discretization used for my model. Following the approach in Zohdi, I will start by integrating Equation 3.1 for the ith particle [66]:

$$\boldsymbol{v}_i(t+\Delta t) = \boldsymbol{v}_i(t) + \frac{1}{m_i}\int_t^{t+\Delta t} \boldsymbol{F}_i^{Total}\, dt \tag{3.27}$$

where $\boldsymbol{v}_i$ is the velocity of the ith particle. Using a trapezoidal rule with a variable integration metric, $0 \leq \phi \leq 1$, we have:

$$\boldsymbol{v}_i(t+\Delta t) \approx \boldsymbol{v}_i(t) + \frac{\Delta t}{m_i}\left(\phi \boldsymbol{F}_i^{Total}(t+\Delta t) + (1-\phi)\boldsymbol{F}_i^{Total}(t)\right) \tag{3.28}$$

Now integrating the velocity equation and applying the trapezoidal once more results in the following for the particle position:

$$\boldsymbol{r}_i(t+\Delta t) \approx \boldsymbol{r}_i(t) + \Delta t\left(\phi \boldsymbol{v}_i(t+\Delta t) + (1-\phi)\boldsymbol{v}_i(t)\right) \tag{3.29}$$

The formulations in Equations 3.28 and 3.29 are implemented in my code for solving for the particle velocities and positions over time. The use of the time stepping parameter ϕ allows for a general formulation with the ability to quickly use explicit and implicit schemes as needed. Using a value of $\phi = 0$, the time stepping scheme will be the explicit Forward Euler, with $\phi = 1$ we have the implicit backward Euler, and with $\phi = \frac{1}{2}$, we have the second order accurate implicit trapezoidal rule.

For the trials discussed below, I used a parameter $\phi = 0$, which resulted in Forward Euler for the time stepping scheme. I chose this scheme as it is the simplest to run, and is fully explicit, using only known data to compute the next time step. While it has first order accuracy for the numerical solution, the goal of this model is to be implemented as quickly as possible, and the accuracy is good enough for this early testing of the framework. For specific use in problems in the future, more accurate, higher order accurate time stepping schemes such as an explicit higher order Runga Kutta method may be more appropriate [33] [21]. Utilizing implicit schemes may allow me to increase the maximum time step due to their larger stability regions, but due to the high number of expected particle collisions and the need to keep the time step small enough to limit particle penetration, the maximum time step size will still have to be small. Additionally, the implicit time stepping schemes would require iterations within the time step, so that will further increase the computation time. It should be noted that throughout the deposition process, there are times when particles are not colliding and are mostly moving due to the driving electric force. This section of the simulation, before many particles start interacting with the substrate, could benefit from a faster time step not used in my current implementation. One way to include this would be to use an adaptive time stepping scheme, which uses an iterative scheme to control error and adjust the time step value based on the current physics of the model [67]. I discuss this topic further below when looking at increasing my model's efficiency.

General Algorithm

Now that the components of the framework have been described, we will be those together to build the full model. The overall general algorithm described with pseudocode is as follows:

1. Generate particles, initialize positions and velocities
2. Begin time loop, for each time step:
3. Begin particle loop, for each particle i:
    a) Check position vs side boundaries, adjust positions, and add ghost particles as needed
    b) Compute gravity, drag, brownian, and Lorentz forces
    c) loop through all other particles j, compute distance for force criteria, and compute all contact and near-field forces on particle i
    d) Check position vs wall, compute wall interaction forces
    e) Sum all components to determine total force
4. Compute new acceleration, velocity, and positions of all particles
5. Step forward in time, and repeat from Step 3 until simulation end

6. Analyze particle trajectories

The general algorithm above was used mostly in the last study below, while it was simplified for the first two. Details on each study and how I used my framework for those are described below. I implemented the framework in python, created functions for each force calculation that could be called as needed when particles met the criteria [52].

3.3 Studies towards verification and validation

This section will describe verification and validation studies undertaken throughout the development of this particle model framework. With my model framework described in the sections above, I performed three main studies:

1. Diffusion Study
2. Electrophoretic Velocity Study
3. Deposition Studies

The first two, the diffusion study and electrophoretic velocity study, used simplified forms of the general algorithm above. For those studies, I am looking at particle behavior without a boundary, and without interparticle interactions, which significantly simplifies the computations required. My aim when choosing these studies was to begin with the framework development by starting out with the simplest situations and then increasing the complexity. Through the consecutive studies, I build that complexity by adding more physics in to the model in the form of forces and boundary conditions.

For third set of studies, I use the full deposition framework as described in the sections above. This set of studies had multiple numerical examples, and looked at the capabilities of the framework to simulate multiple processes, namely electrospray in air and EPD in water. The results of my simulation work thus far will be discussed in the context of these three sets of studies below.

3.3.1 Diffusion Study

This diffusion study is the first study I performed with my model framework. The goal was to start with the simplest situation for my particles - which is particle diffusion in a quiescent fluid. The Brownian force will then be the main driving physical factor as I simulate and analyze the Brownian motion of my particles. This is also the first test study I use for my experimental work discussed further in Chapter 4. The development of both the simulation framework and the experimental work begin from the same starting point. The analysis for this study will be similar to that used in the experimental diffusion trial.

Methods - Simulation Details and Analysis

To begin with this first study, I discuss the physics taken into account in the model, and details on using the simulation framework. The basic steps for this trial will be:

1. Generate particles
2. Track particle positions over time due to Brownian force
3. Compute the Diffusion coefficient

To generate the particles, I sequentially generate random non-overlapping particle positions within a rectangular domain. For this trial, I use a constant particle radius so the distance minimum distance between all particles required for no overlap is constant as well. This is not as important for this particular trial because I do not account for particle interactions, but it is important for the deposition studies and so I implemented it for all the sets of studies. An example of the generated particles is shown in Figure 3.4 below. Visualizations for simulation were created with Tecplot [58].

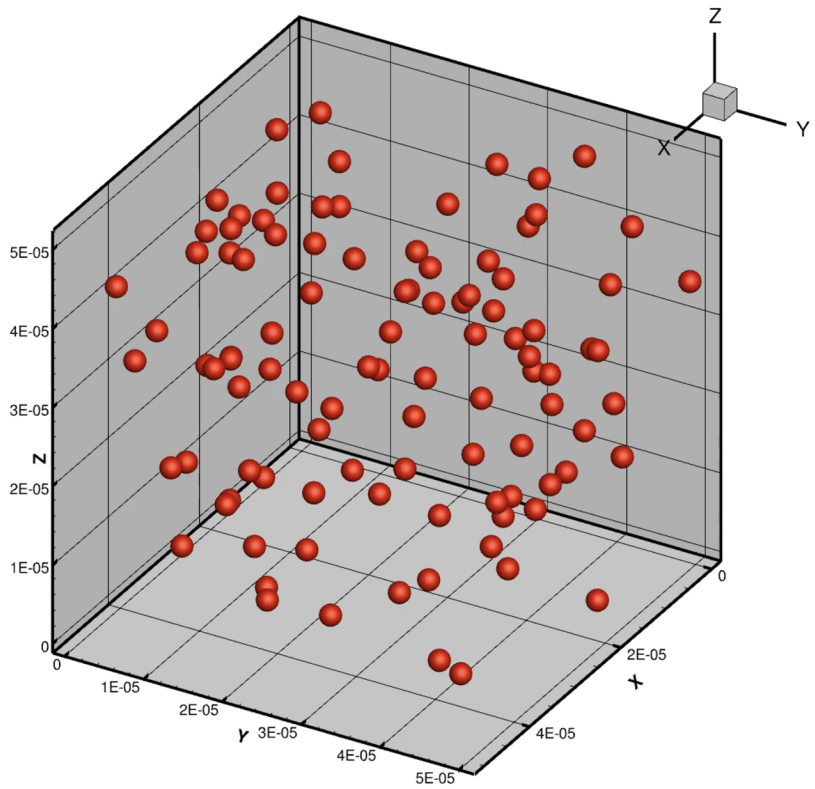

Figure 3.4: Example domain with generated particles.

For this simple diffusion case, the Brownian force will be the only force acting on the particles. The particles will not need to interact in this study, and their trajectories will be used to compute the Diffusion coefficient. However, I do generate multiple particles in each trial to provide more data points for averaging. Therefore the equation of motion for the particle will only use Equation 3.8 for the definition of total force. The inputs for this study are the particle and fluid properties, specifically the particle diameter and fluid viscosity will play particularly important roles in the following analysis. The outputs will be the particle positions over time, or the trajectories, which will be used to compute the diffusion coefficient using the Mean Squared Displacement (MSD).

Brownian motion is exhibited by particles suspended in a fluid and was observed as a "random walk" as the particles are constantly colliding with the smaller fluid particles. These collisions result in motion in random magnitudes and directions. Examining the second moment of positional displacement, or the Mean Squared Displacement, you can obtain the diffusion coefficient using Einstein's relation [8]:

$$\langle \Delta \boldsymbol{r}^2(t) \rangle = 2nDt \tag{3.30}$$

where $\langle\rangle$ is the ensemble average, $\Delta \boldsymbol{r}$ is the displacement of the particle, n is the number of dimensions (i.e. 1, 2, or 3), D is the diffusion coefficient, and t is time. The ensemble average, means the MSD can be computed by averaging over all particles at all time steps for displacement. I use multiple particles in each trial and as I generate trajectories, I can compute displacements over numerous time steps. I then plot the computed MSD vs those time steps and use a polynomial fit to find the slope of the fit line of MSD vs time step. The slope of that plot is used to compute the diffusion coefficient D from equation 3.30. Since the particle framework is set up for 3D analysis, I use $n = 3$. As the particle model framework is implemented in python, I also implement this MSD analysis in python as a pedagogic practice.

To quantitatively evaluate the "experimental" (simulated) diffusion coefficient from my model, I compare it to the diffusion coefficient as calculated by the classical Stokes-Einstein relation. The Stokes-Einstein relation defines the diffusion coefficient as [53] [22]:

$$D = \frac{k_B T}{6\pi \mu_f r} \tag{3.31}$$

where k_B is the Boltzmann constant, T is the temperature, μ_f is the absolute viscosity, and r is the particle radius. This equation relates the motion and diffusion of the particles to the collisions with the fluid molecules and the dissipation from drag [53]. Using this analytical value, I can directly compare it with the results of my simulation from the MSD calculation. The basic steps for this set of diffusion trials is as follows:

1. Generate particles

2. Step through time, computing trajectories due to Brownian force

3. Analyze diffusion by computing D from the slope MSD vs time step calculation in Equation 3.30

4. Compare with analytical diffusion coefficient from Stokes-Einstein relation in Equation 3.31

The results from those trials are discussed below in the next section.

Results and Discussion

For these trials, I computed the diffusion coefficient for different parameter combinations, staying closer to parameter values similar to colloids such as those used in EPD. Following the work of Giera et al., I varied both particle radius and fluid viscosity [22]. The parameters I used for these trials were:

- Particle radius, $R_p = 1nm$, $10nm$, $100nm$, $1\mu m$
- Fluid viscosity, $\mu_f = 0.0001Pa \cdot s$, $0.001Pa \cdot s$, $0.01Pa \cdot s$
- Temperature, $T = 293K$
- Boltzmann constant, $k_B = 1.3806 \times 10^{-23} \frac{Nm}{K}$
- Number of particles, $N_p = 10$
- Number of Time Steps, $N_{ts} = 2.5 \times 10^6$

This essentially became 12 different trials, with 4 different particle radii and 3 different fluid viscosities representing several orders of magnitude of colloidal suspension properties. Using Equation 3.31, this resulted in 6 different orders of magnitude of diffusion coefficients. Each set of 12 parameters was simulated with 20 replicants, and over a final simulation time of $0.2s$ resulting in at least 3.5×10^5 time steps for each trial to provide many data points for displacement calculations. The time step size used for the different trials varied between the trials and was chosen to be the maximum time step size for the suspension parameter sets. This method of choosing time steps is discussed further below. With one plot per viscosity value, we can see the results of the trials plotted in Figures 3.5-3.7 to show data without overlap.

The results are also combined onto one plot as shown in Figure 3.8 with some marker overlap, but showing the results from all 12 trials.

The results shown in Figures 3.5 - 3.7 and 3.8 plot the simulated Diffusion coefficient on the y axis against the analytical diffusion coefficient from the Stokes-Einstein relation on the x axis. The error bars on the plots are defined by the standard deviation. As can be seen from all the plots, the simulation results agree quite well with the analytical expected. To further examine the results, they are summarized in Table 3.1.

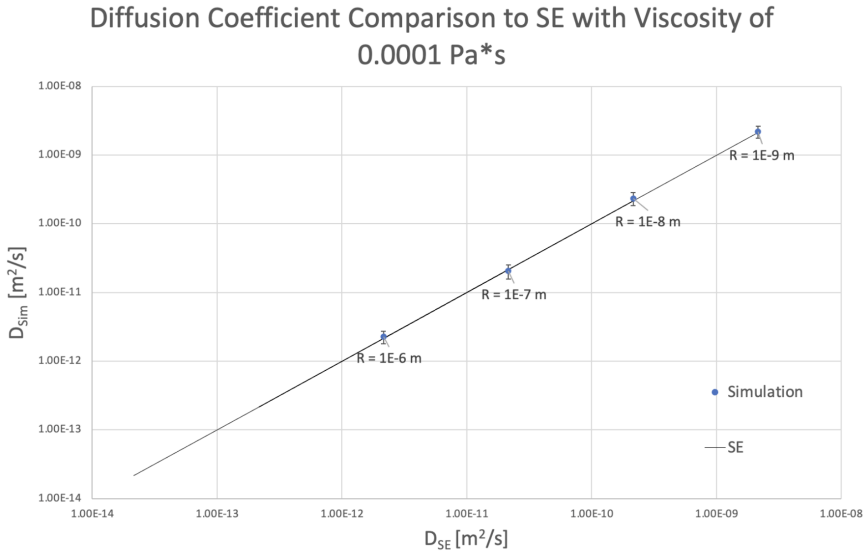

Figure 3.5: Results from the 12 diffusion trials with different plots for each value of fluid viscosity μ_f. Results for $\mu_f = 0.0001 Pa \cdot s$.

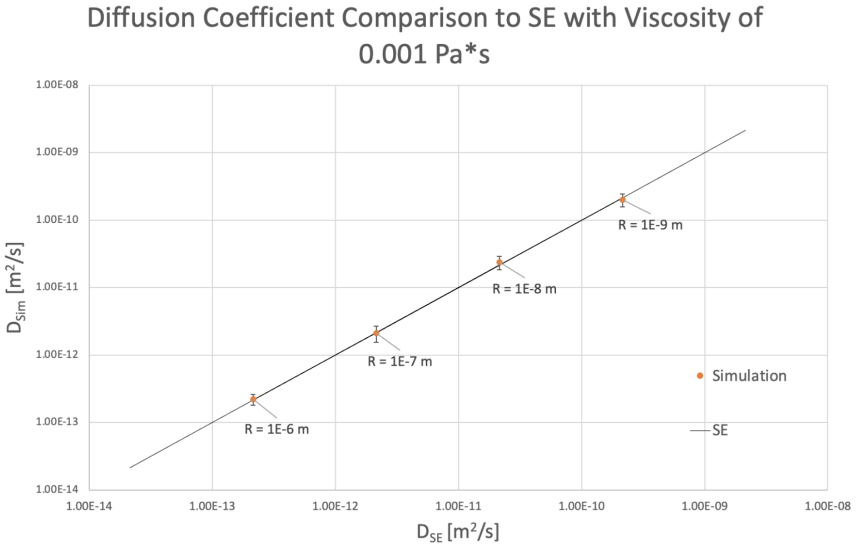

Figure 3.6: Results from the 12 diffusion trials with different plots for each value of fluid viscosity μ_f. Results for $\mu_f = 0.001 Pa \cdot s$.

As can be seen from the results in Figure 3.8 and Table 3.1, the 12 trials result in 6 different expected diffusion coefficients covering 6 orders of magnitude. The tabulated results show fairly good agreement in the 12 trials with the expected analytical value from the

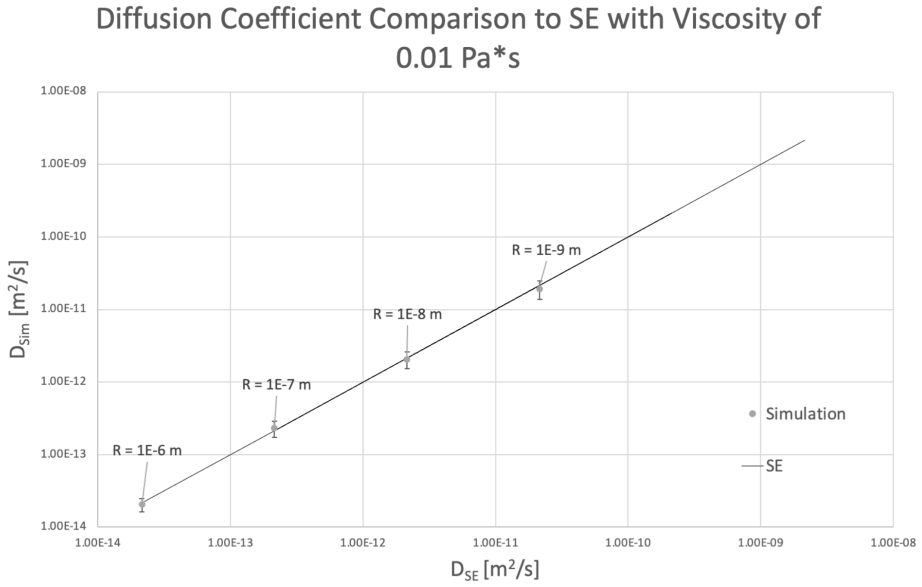

Figure 3.7: Results from the 12 diffusion trials with different plots for each value of fluid viscosity μ_f. Results for $\mu_f = 0.01 Pa \cdot s$.

Table 3.1: Results from the simulated diffusion trials compared with the analytical results from the Stokes-Einstein relation.

Fluid Viscosity, μ_f $(Pa \cdot s)$	Particle Radius, R_p (nm)	Analytical D_{SE} $(\frac{m^2}{s})$	Mean Simulation D_{Sim} $(\frac{m^2}{s})$	$Error$ (%)
0.0001	1	2.15×10^{-9}	2.18×10^{-9}	1.4
0.0001	10	2.15×10^{-10}	2.35×10^{-10}	9.3
0.0001	100	2.15×10^{-11}	2.05×10^{-11}	4.7
0.0001	1000	2.15×10^{-12}	2.28×10^{-12}	6.0
0.001	1	2.15×10^{-10}	2.00×10^{-10}	7.0
0.001	10	2.15×10^{-11}	2.37×10^{-11}	10.2
0.001	100	2.15×10^{-12}	2.11×10^{-12}	1.9
0.001	1000	2.15×10^{-13}	2.21×10^{-13}	2.8
0.01	1	2.15×10^{-11}	1.93×10^{-11}	10.2
0.01	10	2.15×10^{-12}	2.06×10^{-12}	4.2
0.01	100	2.15×10^{-13}	2.30×10^{-13}	7.0
0.01	1000	2.15×10^{-14}	2.06×10^{-14}	4.2

Stokes-Einstein relation. 6 of the 12 trials had a percent error between the mean simulated diffusion coefficient and the analytical diffusion coefficient of $< 4.7\%$. However, the other half

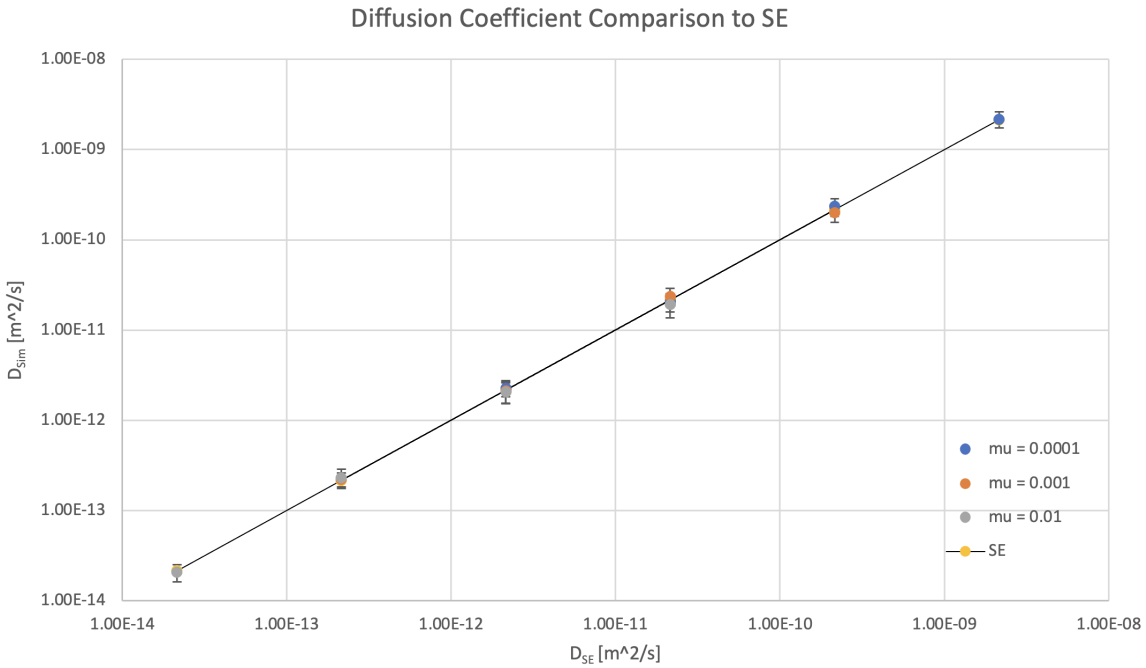

Figure 3.8: Results from the 12 diffusion trials on one single plot comparing the simulated diffusion coefficient with the analytical diffusion coefficient from the Stokes-Einstein relation.

of trials stretched beyond that. The maximum percent error between the mean simulated value and the expected analytical value was 10.2%. This actually occurred in two different trials, both with an expected value of $D_{SE} = 2.15 \times 10^{-11} \frac{m^2}{s}$. Giera et al. performed a similar study across the same ranges of parameters with their model implimented in the LAAMPS framework and they found a maximum error in their trials to be 5.6% [22]. While my results showed a higher percent error, they were still relatively close to the expected analytical value.

One potential factor leading to a difference in results could be the time constant and chosen time step when computing the diffusion coefficient in the simulation. The time constant I refer to here is the viscous time scale at which the energy from collisions with fluid molecules approximately dissipates before another effective Brownian force collision is applied. This viscous time scale is on the order of $10^{-9}s$ for a $100nm$ neutrally buoyant particle suspended in water [53]. As I was developing this model, I wanted to run the simulation with larger time steps to maximize the final time and allow the particles to effectively diffuse longer. As I was testing, I found that by going too high, I could cause the simulation to go unstable and the positions would diverge, which is a limitation of the time stepping scheme I chose (Forward Euler). However there was a situation where the time step chosen was large while still resulting in a stable simulation, but the magnitude of

the simulated diffusion coefficient was significantly higher than the expected value. I found that in this regime, the Brownian force magnitude could essentially be too high, causing the displacements to also be larger. This occurred when the time step chosen was greater than the viscous time scale for that particular suspension. To correct for this, I reformulated the Brownian force definition to be computed by an average impulse-like definition such that:

$$\boldsymbol{F}^{Brownian} = \boldsymbol{F}_O^{Brownian}\frac{t*}{dt} \tag{3.32}$$

where $\boldsymbol{F}_O^{Brownian}$ is the original Brownian force definition defined by Equation 3.8, dt is the time step of the simulation, and $t*$ is a time constant representing the viscous time scale. Both dt and $t*$ have the units of s, so effectively I am computing the impulse of an average Brownian force, and then scaling it by the time step of the simulation so that the magnitude of the acceleration is not overly large in the situation described above. This additional scaling term also helped in the opposite situation where the simulation time step was much lower than the viscous time scale and the displacements were too low.

Now with the new definition of Brownian force scaled appropriately in Equation 3.32, I wanted to generally define a $t*$ for my model framework that would work decently well for most conditions I applied. To find a time constant that worked, I started with a constant of $t* = 1 \times 10^{-9}s$ and then varied the value while computing the diffusion coefficient for suspensions with parameters across the orders of magnitude in the 12 trials. Performing these trials, I found a value of $t* = 7 \times 10^{-9}s$ led to a mean value of diffusion coefficients matching decently well for the range of parameters. Now in my model, I chose to apply this value to the broad range of suspension parameters as a broad solution. A more rigorous solution might include a broader set of trials repeating the same strategy, but determining a $t*$ value for each set of parameters. In practice this could be performed for every set of parameter values, and would most likely lead to an improvement in the mean error as the time scale is more acutely tuned for the specific conditions. However, as the number of suspensions simulated increases, so will the convergence trials needed to find the time scale. This is a tradeoff, and for this set of diffusion trials I chose to limit those efforts, to find one value that worked fairly well for my range of cases.

One set of parameter convergence trials I did perform was for the time step values for each suspension. As mentioned above, I wanted to maximize the time step for each suspension trial to minimize the required run time of my framework. This follows my larger goal of balancing the ability of my framework to produce results while operating more quickly and capably on a laptop. To achieve this with this first set of trials, I ran repeated trials of each suspension parameter set varying only the time step dt of the simulation. I increased time step sizes until the error between the mean diffusion coefficient and the analytical diffusion coefficient became more than one half of the standard deviation. To improve the overall mean error, I could have decreased my tolerance while performing these convergence trials, which would most likely have resulted in a smaller time step size for each trial. In future trials, the sensitivity to time step size could be further explored. However in this case, I

found that balancing the error I found with maximizing the time step to be a worthwhile trade-off in my trials.

In summary, the results from the diffusion study showed fairly good agreement with the analytical comparison for diffusion coefficient computed with the Stokes-Einstein relation. This was a first test of my particle framework, and the diffusion case study was the most simple for physics involved as the driving force was dependent on only the Brownian force and particle interactions were not taken into account. 12 suspension parameter sets were run, resulting in diffusion coefficients spanning 6 orders of magnitude, similar to a trial performed by Giera et al. [22]. The results showed a maximum error of 10.2%. For my model, I made several simplifying decisions which could have factored into this error, namely using a single time scale factor for the Brownian force for the 12 different suspension combinations, and choosing a simulation time step to minimize my simulation's run time based on a user-specified tolerance. To address these factors, future studies could preform a set of convergence trials to find a time scale value tailored for each suspension, as well as adjust the user specified tolerance in the time step convergence trials to reduce the overall error. These results were a relatively successful first step in my model framework development.

3.3.2 Electrophoretic Velocity Study

The next study I performed with my framework is the electrophoretic velocity study. Increasing the complexity of the physics included with the framework, I moved on from the initial diffusion study and then investigated electrophoresis, or the motion of particles due to the external electric field. In this study, the main forces involved are the Lorentz force due to the external electric field moving the particle and the Drag force imparted by the surrounding fluid to oppose that motion. The balance between these opposing forces will determine the motion of the particles in the suspension when I apply an electric field, and that motion is study by investigating the terminal velocity of the particles.

Methods - Simulation Details and Analysis

For this study, the basic steps were:

1. Generate particles
2. Track the particle velocities and positions over time
3. Compute the average terminal velocity of the particles

Similar to the diffusion trial described above, I simulated multiple particles for averaging. I used the same algorithm as in that trial, sequentially generating the particles in random, non-overlapping positions. Again for this trial, I do not account for particle interactions, under a similar assumption of investigating dilute suspensions. I again used a constant radius when generating the particles, but added some new particle parameters to the model. The

effective particle charge in general could be assumed to be a known parameter based on the process, but for this particular case with colloids, I use a definition derived by Giera et al. [22]:

$$\begin{aligned} q^{col} =& \frac{\pi\zeta R_p\epsilon_0\epsilon}{24\lambda_d^6}\left(R_p^5\lambda_D - R_p^4\lambda_D^2 - 10R_p^3\lambda_D^3 + 6R_p^2\lambda_D^4 + 96\lambda_D^6\right. \\ &\left. + R_p^4(12\lambda_D^2 - R_p^2)e^{\frac{R_p}{\lambda_D}}\int_1^\infty \frac{e^{-\frac{R_p\hat{g}}{\lambda_D}}}{\hat{g}}d\hat{g}\right) \end{aligned} \tag{3.33}$$

where ζ is the Zeta potential of the suspension, ϵ_0 is the permittivity of free space, ϵ is the relative permittivity, and λ_D is the debye length. With this expression for effective colloid charge, the value q_p can be defined with parameters that are able to be directly measured in an experiment [22]. I do not always use this definition of charge, especially when simulating larger particles in air for the deposition study as discussed further below, but I do employ it for the cases with colloids like in this study and for deposition with EPD.

Now with the particles generated, the main forces acting on them in this study are the Lorentz force and the Drag force. These two forces act in opposing directions as shown in Figure 3.9. The particles in the figure are shown moving in the same direction as the electric field, indicating they have a positive effective charge. The Lorentz force and Drag force are computed using Equations 3.7 and 3.2, respectively. I simulate the particles over a range of simulation time that allows the particle to find an equivalent terminal velocity and remain at that steady state. I performed exploratory studies to determine the simulation times for each suspension parameter set where I found the velocities to not change between several successive time steps. The outputs of each suspension parameter set simulation run are the average terminal velocity of the particles.

For an analytical comparison of these electrophoretic terminal velocities, I use the Henry velocity described by the Henry equation [22]:

$$v_H = \frac{2}{3}\frac{E\zeta\epsilon\epsilon_0}{\mu_f}f\left(\frac{R_p}{\lambda_D}\right) \tag{3.34}$$

where v_H is the Henry velocity, E is the applied electric field, and the term $f\left(\frac{R_p}{\lambda_D}\right)$ is the Henry function and accounts for variations due to suspensions with different double layer thicknesses. This function varies from $f\left(\frac{R_p}{\lambda_D}\to 0\right)\to 1$ in the thin double layer limit to $f\left(\frac{R_p}{\lambda_D}\to\infty\right)\to\frac{3}{2}$ in the thick double layer limit. To keep my framework general, I used an expression presented by Swan and Furst to compute an approximate Henry function value for variable double layer thicknesses [57]. This relation for the Henry function is a simple approximation that matches within 0.1% for all values of $\frac{R_p}{\lambda_D}$ and is given as [57]:

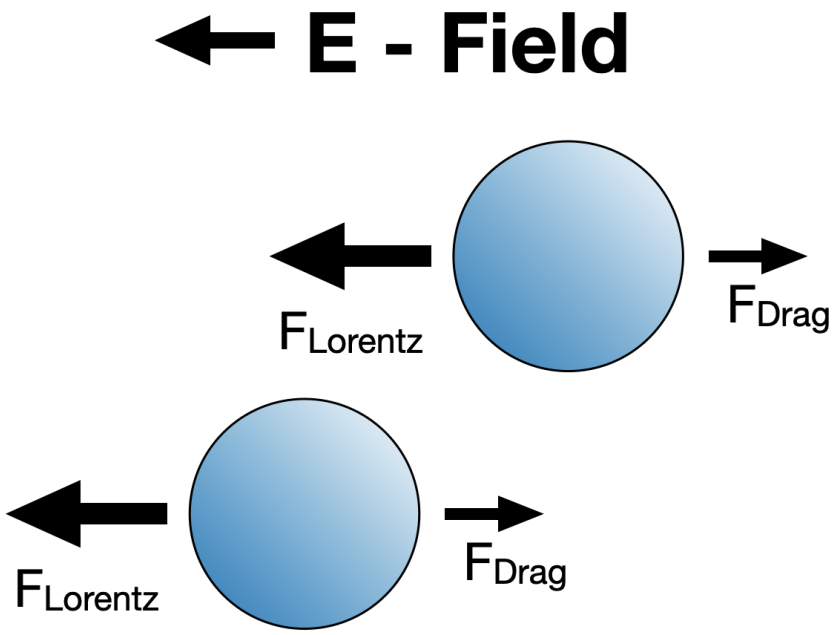

Figure 3.9: Graphic of forces acting on particles for the electrophoretic velocity study. The force directions are assuming the particles have a positive charge so they are moving in the same direction of the E-field.

$$f\left(\frac{R_p}{\lambda_D}\right) \approx \frac{16 + 18\frac{R_p}{\lambda_D} + 3\left(\frac{R_p}{\lambda_D}\right)^2}{16 + 18\frac{R_p}{\lambda_D} + 2\left(\frac{R_p}{\lambda_D}\right)^2} \tag{3.35}$$

For a suspension parameter set, I then simulate the particles and compute the electrophoretic velocity at different field strengths to compare to the analytical Henry velocity as computed in Equation 3.34 in Python [52]. An example comparison across 6 different orders of magnitude of electric field strength is shown in Figure 3.10.

Now with the analytical Henry velocity defined, I simulate a range of simulations by varying the parameters of particle radius, fluid viscosity, and relative permittivity. The basic steps for this set of trials comparing the terminal electrophoretic velocity are as follows:

1. Generate particles and compute effective colloid charge
2. Step through time, compute velocities due to Lorentz and Drag forces until reaching steady state
3. Repeat for a range of electric field strengths

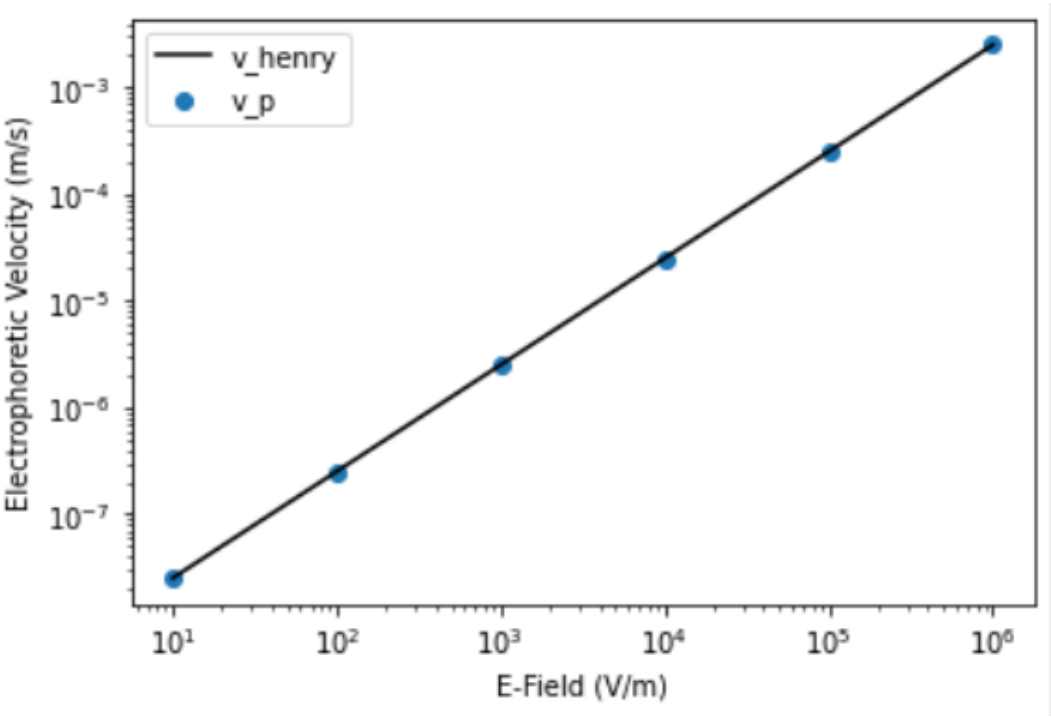

Figure 3.10: Example velocity comparison across 6 orders of magnitude of electric field strength.

4. Compare the simulated terminal velocity with analytical Henry velocity defined in Equation 3.34

The results for the electrophoretic velocity study are discussed in the following section.

Results and Discussion

For this electrophoretic velocity study, I ran several different particle suspension simulations and computed the terminal velocity. Again following a similar study performed by Giera et al., I created the suspension parameter sets by varying the particle diameter, fluid viscosity, and relative permittivity [22]. The parameters I used for this trial were:

- Particle Radius, $R_p = 10nm$, $100nm$, $1\mu m$
- Fluid viscosity, $\mu_f = 0.0001Pa \cdot s$, $0.001Pa \cdot s$, $0.01Pa \cdot s$
- Relative Permittivity, $\epsilon = 2$, 40, 80
- Vacuum Permittivity, $\epsilon_0 = 8.85419 \times 10^{-12} \frac{C^2}{N \cdot m^2}$
- Zeta Potential, $\zeta = -0.05V$

- Number of particles, $N_p = 10$
- Electric Field Strength, $E = 10\frac{V}{m}$, $100\frac{V}{m}$, $1000\frac{V}{m}$, $1 \times 10^4\frac{V}{m}$, $1 \times 10^5\frac{V}{m}$, $1 \times 10^6\frac{V}{m}$

These sets of parameters define 27 different suspensions with 3 different particle radii, 3 fluid viscosities, and 3 relative permittivities. In each case described above, I also use a constant ratio of $\frac{R_p}{\lambda_D} = 2$ similar to Giera et al. For each suspension, I simulate the particles moving due to the Lorentz force and the Drag force and compute their terminal velocities to compare with the analytical Henry velocity using Equation 3.34 across 6 orders of magnitude of electrical field strength E. For each suspension I average the velocity across 10 particles and 500 replicants. In these trials the actual electrical field applied was $\boldsymbol{E} = [0, 0, -E]$ so the field was oriented down in the z direction. The suspensions had a zeta potential $\zeta = -0.05V$, so the charge of each particle computed with Equation 3.33 was also negative. Together, this caused particle motion to move in the positive z direction. In the plots below, the field strength E is the magnitude of the applied electric field. The time steps and final simulation times varied across the different suspension parameter sets and were determined by running the simulation trials to find appropriate values. This is discussed in further detail below. The results from the 27 different trials are shown in Figures 3.11 - 3.13.

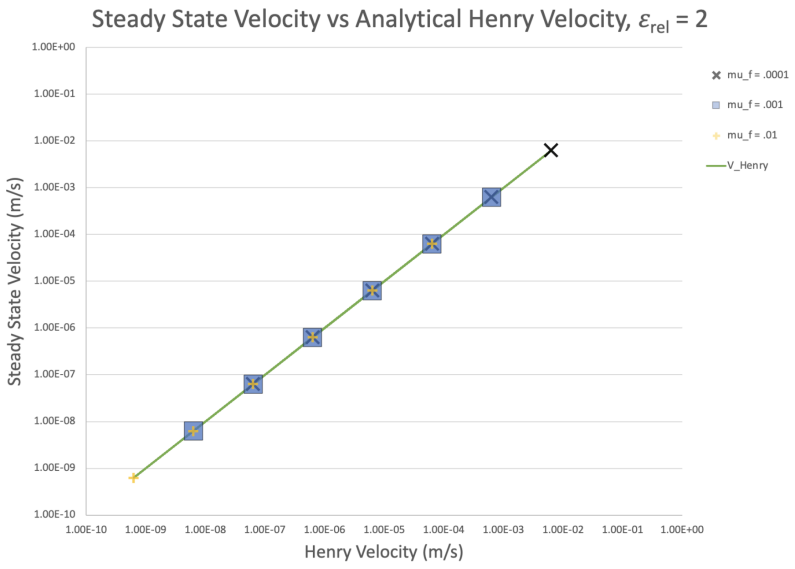

Figure 3.11: Velocity study results from 9 different suspension parameter sets with relative permittivity $\epsilon_{rel} = 2$. The simulated steady-state velocity plotted against the analytical Henry velocity.

The three plots shown plot the simulated Steady-state (or terminal) velocity on the y axis against the analytical Henry velocity from Equation 3.34 on the x axis. The line represents the Henry velocity and has a slope of 1. The velocities in each plot show relatively

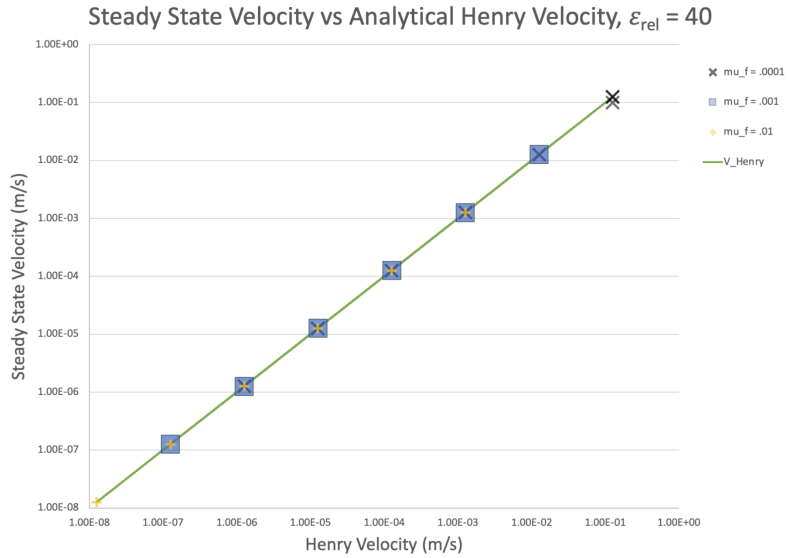

Figure 3.12: Velocity study results from 9 different suspension parameter sets with relative permittivity $\epsilon_{rel} = 40$. The simulated steady-state velocity plotted against the analytical Henry velocity.

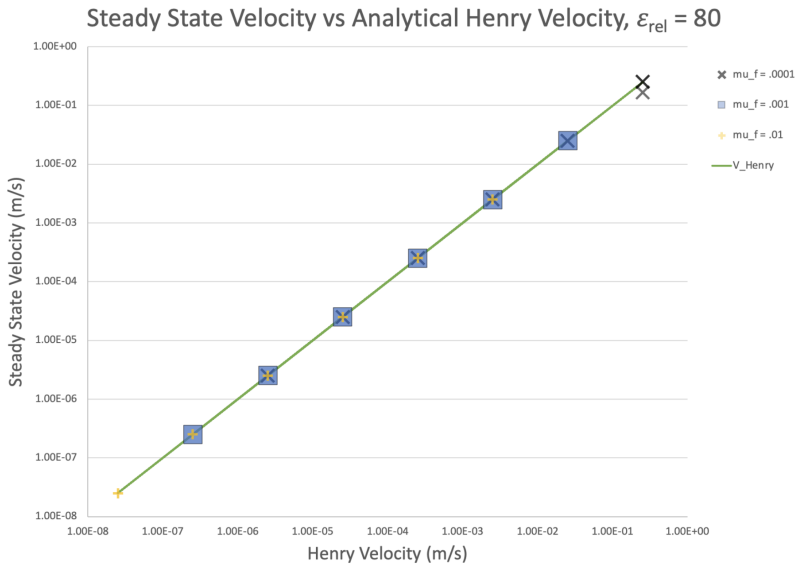

Figure 3.13: Velocity study results from 9 different suspension parameter sets with relative permittivity $\epsilon_{rel} = 80$. The simulated steady-state velocity plotted against the analytical Henry velocity.

good agreement across the 8 orders of magnitude of velocity. The points with the largest deviation from the expected value can be seen at the highest velocity points on both the middle and lower plots. These points correspond to the suspensions with lowest viscosity $\mu_f = 0.0001Pa \cdot s$ and the largest diameter particle $R_p = 1\mu m$. While these points may be outliers, the similarities of them being one of the more edge cases on the higher end of velocity indicates it may be due to one of the factors of my trial design.

For each combination of particle radii R_p and fluid viscosity μ_f, I determined a time step and final simulation time value based on convergence trials. When I performed these trials, I used my initial results from the case of the $\epsilon = 2$ and did this for only a small number of replicants. It is possible that the time step chosen for these trials was not small enough or the simulation time was not large enough to allow the particles to fully reach their terminal velocity. The latter seems unlikely as in all cases I checked, I noticed velocity leveling off quite quickly on the order of hundreds of time steps.

To investigate the cases above, I performed a sanity check of computing the terminal particle velocity in a simple force balance. Assuming the Lorentz force and the Drag force are balanced at steady state, i.e. acceleration is zero, I approached with an implicit solution method to determine the steady state velocity. For the computations below, I performed them only in the z or $\boldsymbol{e}_3$ direction for simplicity.

$$\begin{aligned} \boldsymbol{F}^{Lorentz} + \boldsymbol{F}^{Drag} &= ma = \mathbf{0} \\ \boldsymbol{F}^{Lorentz} &= -\boldsymbol{F}^{Drag} \\ q_p E &= C_D(Re(v_{ss}))\pi R_p^2 \rho_f \|v_{ss}\|^2 \\ \Rightarrow v_{ss} &= \sqrt{\frac{q_p E}{C_D(Re(v_{ss}))\pi R_p^2 \rho_f}} \end{aligned} \tag{3.36}$$

where v_{ss} is the steady state velocity and C_D is explicitly showing it is a function of Reynolds number Re, which is in turn a function of the steady state velocity v_{ss}. With v_{ss} on both sides of Equation 3.36, this can be solved implicitly. I use a simple fixed point iteration with an initial guess to find the steady state velocity as follows:

1. Set initial guess velocity
2. Loop over a max number of iterations
    a) Compute Re and C_D with v_{guess}
    b) Compute v_{new} from Equation 3.36
    c) Update $v_{guess} = v_{new}$ and repeat until convergence

where the definition of convergence is controlled by a tolerance between successive guesses. I found that typically this occurred in a very short number of iterations, usually less than 10.

Figure 3.14 shows an example plot of the guess velocity vs iteration when using the implicit fixed-point iteration method described above to find the steady state velocity implemented in Python.

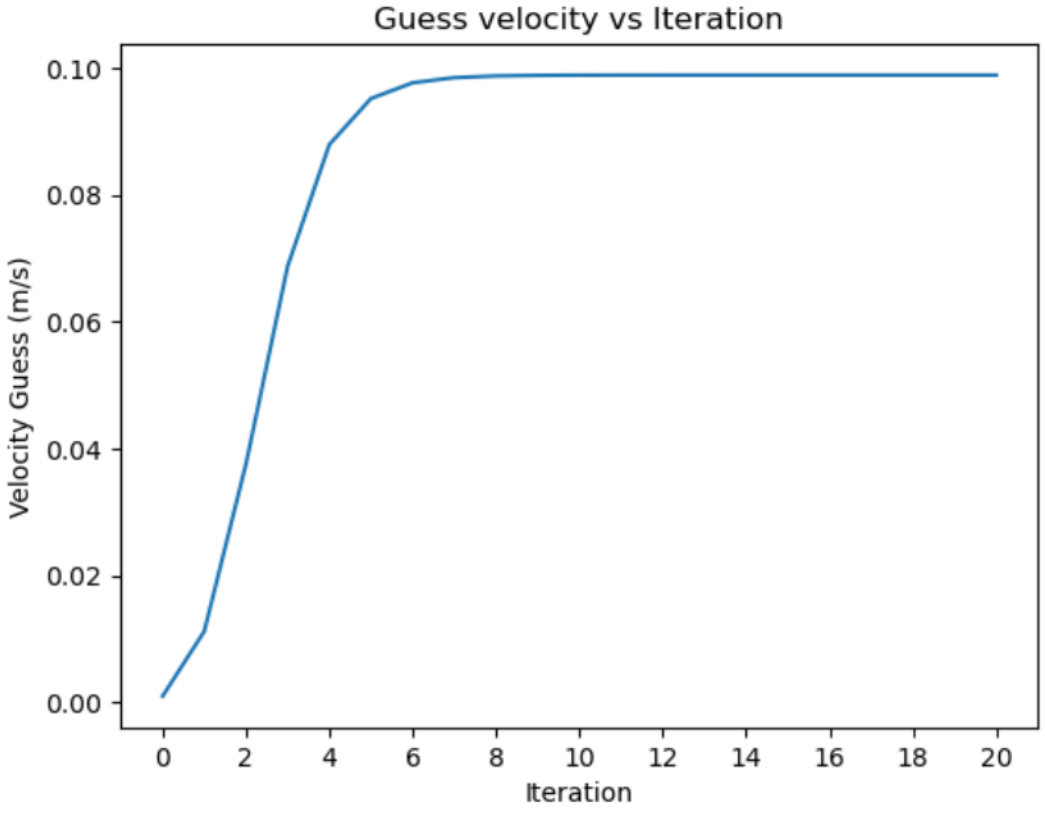

Figure 3.14: Plot of the guess velocity vs Iteration while solving for the steady state velocity from the force balance in Equation 3.36. The velocity levels off near iteration 7.

I utilized this sanity check on all the electrophoretic velocity trials to ensure my steady state velocity computed with my explicit method was consistent with the implicit as well. Across the 27 trials, I found a difference in computed steady state velocities between my explicit simulation and implicit check to be less than 0.2%. Specifically, the two cases mentioned above that deviated from the analytical Henry velocity had an error of 21.5% between the explicit steady state velocity and the Henry velocity for the $\epsilon = 40$ case and 34.5% for the $\epsilon = 80$ case, but between my implicit check and the explicit steady state velocity, they had $< 0.01\%$ difference in both cases. This indicated to me that my explicit simulation model was consistent with my implicit force balance for all cases, but that my assumptions of the physics involved may have limits, represented by physical cases described by the parameters in those two trials.

To better visualize the range of parameters I explored in the electrophoretic velocity trial, I investigated non-dimentionalizing the system. I computed the non-dimensional Péclet number, Pe, which is the ratio of convective to diffusive motion of the particle suspensions with the applied electric fields.The Péclet number is defined as:

$$Pe = \frac{|v_H|}{D_{SE}} R_p = \frac{6\pi R_p^2 |E\zeta| \epsilon\epsilon_0}{k_B T} f\left(\frac{R_p}{\lambda_D}\right) \tag{3.37}$$

where D_{SE} is the diffusion coefficient as defined by the Stokes-Einstein relation discussed earlier in this chapter. I used the same temperature as in the previous section, room temperature, for my cases in this study as well. At each value of the Péclet number, I also computed a ratio of the simulated steady state velocity over the analytical Henry velocity. I used the velocity found using my explicit simulation for this analysis. Figure 3.15 shows the plot of the velocity ratios plotted against the Péclet number.

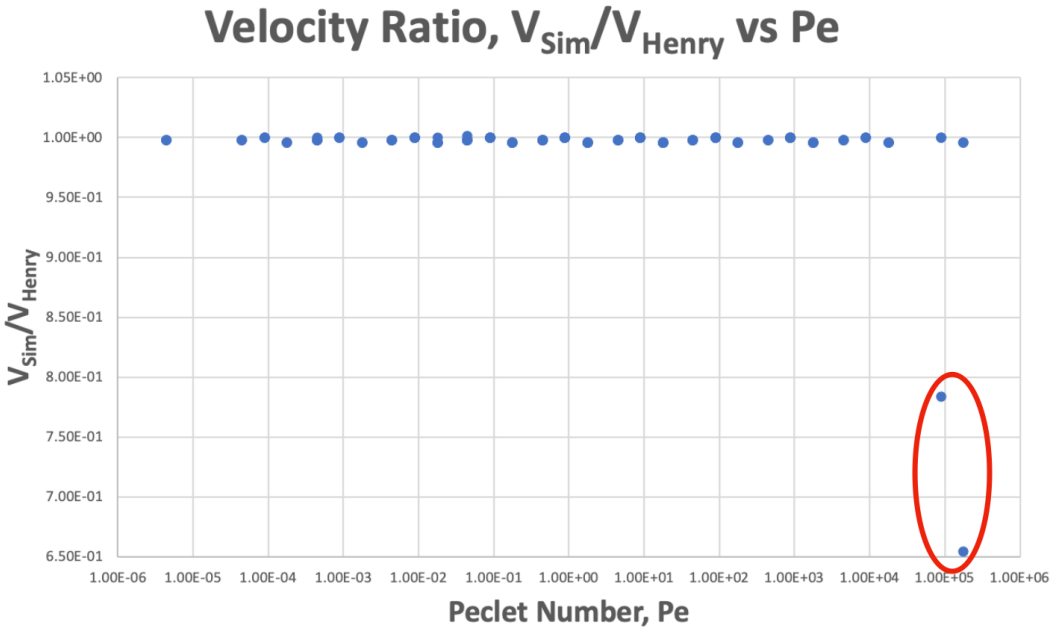

Figure 3.15: Plot of the ratio of simulated velocity over Henry velocity over the Péclet Number Pe. The vast majority of cases is near the ideal value of 1, but two outlying cases are highlighted in red.

The plot in Figure 3.15 shows the ratio of the simulated steady state velocity to the analytical Henry velocity on the y axis and the Péclet number on the x axis. As can be seen from the plot, the vast majority of the trials were very close to the ideal ratio of 1. This represents a large range of parameters for colloidal suspensions, covering 12 orders of magnitude of Péclet number. This good agreement indicated to me that the model was able to capture the essential physics for electrophoretic motion in the majority of cases. The

two outlier points circled in red represent the two cases that had a higher error as described above. They had a velocity ratio below 1, indicating that the trials produced a lower steady state velocity vs the analytical Henry velocity. This could be an indicator that my simplifying assumptions start to break down in this higher limit of Péclet number, and introduce error.

Summarizing the results shown in Figure 3.15, I tablulate the average error for a order of magnitude of Péclet number below in Table 3.2. The percent error is computed as:

$$\%\text{Error} = \left|1 - \frac{V_{Sim}}{V_H}\right| \times 100\% \tag{3.38}$$

Table 3.2: Summary of error between electrophoretic velocity ratio for Péclet number order of magnitude.

Pe Order	Percent Error
1×10^{-6}	0.16%
1×10^{-5}	0.08%
1×10^{-4}	0.17%
1×10^{-3}	0.14%
1×10^{-2}	0.15%
1×10^{-1}	0.16%
1	0.19%
1×10^{1}	0.22%
1×10^{2}	0.19%
1×10^{3}	0.24%
1×10^{4}	3.80%
1×10^{5}	11.77%

From Table 3.2, good agreement is seen across the first 10 orders of magnitude with the average error being below 0.24%. It is in the last two orders of magnitude of Pe that I start to get the percent error to increase with the presence of the two cases circled in Figure 3.15. This may be an indicator that my assumptions in formulating the model may not be capturing all the physics as well as I hoped in this regime. The results from this trial were still helpful to me in identifying where the model may need more investigation to understand the electrophoretic behavior of particles. This result of high Pe starts to represent the edge cases for my model and would be the sight of future studies using this code framework. Giera et al. performed a similar study and found their cases near this order of magnitude of Pe to have good agreement, so future work can start to investigate the differences between my simple model formulation and the more expansive one used in their studies [22]. Besides those two cases, I had good agreement across the wide range of parameters, and used this as a milestone to then begin studying the deposition of particles as described in the next section.

3.3.3 Deposition Studies

The third set of studies I performed with my model framework are focused on the deposition of particles. Now further increasing the physics involved, I take into account all the forces described above to factor in all of the external field, environmental, and inter-particle forces used to cause the motion of particles in deposition processes. The field-driven AM processes of interest vary widely in their parameters, and I intended for this framework to be a tool capable of simulating those separate cases. Here I will discuss the cases I investigated and present the results of some of the trials with parameters similar to electrospray of particles in air and EPD of colloids in water. The examples here show some of the capabilities and limitations of my model framework approach.

Methods - Simulation Details and Analysis

Similar to the previous two studies, the basic steps of these depositions were:

1. Generate particles
2. Track particle velocities and positions over time
3. Analyze the deposit structure

Throughout the development of this model framework, and especially with these deposition studies, I began with small numbers of particles before increasing the number of particles to see what a larger deposition would look like. For testing, this could mean I generated anywhere from 20 to 2000 particles for investigating the interaction of all the forces and the resulting deposits. In all cases, I used the same algorithm as described in the first diffusion studies, where I sequentially generate the particles in random, non-overlapping positions within a defined representative volume element, or voxel, that scales in size with the number of particles. To save on computational time, I started the region of particle generation to be near the surface so the lowest particles will start interacting with the bottom wall soon in the simulation. If I made the offset higher, generating more and more particles in the bulk, a lot of time steps would be used in just moving particles before any significant interactions took place. The particles are initialized with velocities in the direction consistent with the overall Lorentz force with a magnitude on the order of the Henry velocity to present the scenario where these particles have been moving from the bulk towards the substrate due to electrophoresis. I used a constant time step for my simulation framework, but like mentioned above when discussing the time stepping scheme, future additions to this framework could include an adaptive time stepping scheme that would also larger time steps to be used in instances such as when particles are mostly moving through the bulk fluid before there are many interactions with the wall and other particles. However, this technique of starting the particles closer to the substrate helped make the simulation time within reason, even when needing to use a small time step for certain conditions. This will be discussed further in detail below in the results and discussion section.

One new addition I made to the particle generation step was allowing for variable particle radii. Up to this point, I had formulated the code and run the trials with a constant particle radius. However, to allow for more detailed studies in the future such as those looking at uncertainty quantification due to particle size, I allow for variation in the radius to be introduced by the simple relation:

$$R_{pi} = \bar{R}_p(1 + \alpha_{Rad} c_i) \tag{3.39}$$

where R_{pi} is the radius of Particle i, $\bar{R}_p$ is the mean particle radius, α_{Rad} is a parameter defining the amount of variation, and c_i is a random number between -1 and 1. As the particles are generated, I also sequentially compute the radius at the same time to properly compute distance between existing particles to make sure there is no initial overlap. Using this relation, I was able to choose as much variation as I wanted, but for most trials I used uniform radii. To add no variation, I just set the parameter $\alpha_{Rad} = 0$.

After the particles are generated, the simulation will then step through time, computing all the forces on each particle to solve their equations of motion. In these studies, I employ all the forces defined above in Equations 3.2 to 3.26. For each particle this step can be computationally intensive as many of the forces are dependent on the relative distance to other particles. I discuss several methods to improve the efficiency, particularly for these calculations further below.

While most of the examples moving forward are mostly qualitative in nature, one method of quantitative analysis I use is a quantitative look at the "order" of a deposit. A more ordered, or more crystalline, structure of a deposit will in general have each particle with more nearest neighbors than an amorphous or less ordered deposit. In a more amorphous deposit, the particles may have voids between them that limit the number of nearest neighbors they are able to have. As a measure of this "order", I used the coordination number of each particle. For my model, I define the coordination number of a particle as the number of nearest neighbors. To define nearest neighbors, I set a distance from the particle center, generally related to that particular particle's radius. When analyzing a deposit, I can look at the positions of the particles, and for each particle, count the number of neighboring particles within that set "nearest neighbor" distance. This is graphically shown in Figure 3.16.

In the example case shown in Figure 3.16, the red particle is being analyzed and checked for its nearest neighbors defined by the center distance denoted R_{CN}. In this case, 3 particles have a center distance within that range and are highlighted in green. The blue particles are out of that range, so are not counted towards the nearest neighbors to add to the coordination number.

The higher the coordination number, the more local order is in the deposit near it. This is similar to the coordination number used when analyzing atoms in a crystal structure. For my colloidal crystals, the particles are analogous to the atoms, and the coordination number can be a measure of the order of that structure. This is also a quantity used by Giera et al.

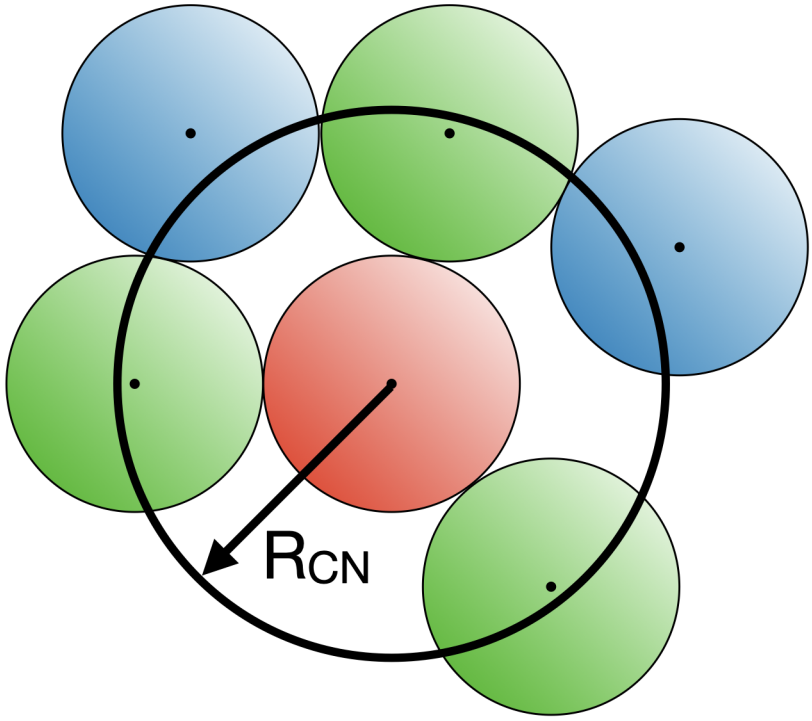

Figure 3.16: Example of the coordination number for a particle. In this case, the red particle has a coordination number of 3 highlighted by the nearest neighbor green particles. The nearest neighbors are defined by a center distance below a parameter denoted R_{CN}.

in their mesoscale model of EPD and since I also aim for this simulation framework to be able to analyze deposits made with EPD, I took a similar approach [23] .

Results and Discussion

The following examples are investigating the behavior of depositing particles with my simulation framework. Some of the studies are more qualitative in nature to make observations about the particle behavior and discuss limitations of my framework in the various cases. I intended this model framework to be used for varying field-driven AM processes, so the parameters in the examples below will vary from larger particles moving through air as in an electrospray process to smaller particles, colloids, moving through water as in EPD.

The first example I examine was a test of the simulation framework similar to one performed by Zohdi [66]. In this example, I was interested in a first check that particles could interact with each other and the bottom wall, so this do not yet include the sidewall periodic boundary conditions detailed in prior sections. This trial represented charged particles moving through air towards a substrate, and are allowed to spread with no sidewalls. The

parameters I used for this first example were:

- Number of particles $N_p = 1000$
- Mean Particle radius $\bar{R}_p = 0.05m$
- Particle radius variation $\alpha_{Rad} = 0$
- Particle density $\rho_p = 1540\frac{kg}{m^3}$, silica
- Fluid density $\rho_f = 1.2754\frac{kg}{m^3}$, air
- Fluid viscosity $\mu_f = 18.03 \times 10^{-6} Pa \cdot s$
- Electric field $\boldsymbol{E} = [0, 0, 100]\frac{V}{m}$
- Particle charge per unit mass $\frac{q_p}{m_p} = -1\frac{C}{kg}$
- Contact damping parameter $c_{cd} = 10^8$
- Friction compliance constant $K_f = 10^9$
- Static friction coefficient $\mu_s = 0.4$
- Dynamic friction coefficient $\mu_d = 0.3$
- Particle-particle contact compliance constant, $K_p = 10^9$
- Particle-particle contact exponent $p_p = 2$
- Particle-particle normal bonding parameter $K_p^{nb} = 10^8$
- Particle-particle rotational bonding parameter $K_p^{rb} = 10^5$
- Particle-wall contact compliance constant, $K_w = 10^{11}$
- Particle-wall contact exponent $p_w = 2$
- Particle-wall normal bonding parameter $K_w^{nb} = 10^{10}$
- Particle-wall rotational bonding parameter $K_w^{rb} = 10^7$
- Bonding law exponent $p_b = 2$
- Near-field parameters, $\bar{\alpha}_1 = 0.5$, $\bar{\alpha}_2 = 0.05$, $\beta_1 = 1$, $\beta_2 = 2$

The parameters were determined through experimentation with the simulation, and this is just one example of a potential set. Part of the experimentation was finding good time parameters that resulted in a stable simulation. I was using the Forward Euler time stepping scheme, with a time stepping parameter $\phi = 0$ in Equations 3.28 and 3.29. For this example the time parameters were:

- Time step $dt = 1 \times 10^{-6} s$
- Final simulation time $t_f = 0.1 s$

The time step was determined to minimize the code runtime, as with the number of particles $N_p = 1000$, the interactions start to cause the runtime to increase significantly. Successive frames from this simulation are shown in Figure 3.17.

The frames shown in Figure 3.17 starting in the upper left panel show the progression from particles in random generated positions, then starting to fall in the upper right panel with the first initial contact with the substrate. The middle left panel then shows particles continuing to fall until they have all fallen and begun to spread out in the middle right frame. Finally the bottom frame shows the end result as the particles have spread out a little more and settled. A few observations can be made from this simulation, including how the particles are clumped together, and how they settle in the z direction.

As can be seen from this last frame in particular, the particles have spread, but are still pretty clumped together. This is possibly due to the higher attraction forces in the near-field force definition. This can be investigated more by looking into the interplay of those parameters, the α's and β's. For illustration purposes, I run similar trials, but with a lower number of particles. As an example, I look at the top down view of the $x - y$ plane for two different trials using 100 particles. The results are shown in Figure 3.18. In the left panel, labeled a), the α's and β's are the same as in the first example parameters listed above with $\bar{\alpha}_1 = 0.5$, $\bar{\alpha}_2 = 0.05$, $\beta_1 = 1$, $\beta_2 = 2$. As shown, the particles look more clumped together, as which may be due to the higher parameter α_1 which corresponds to the attractive force. The right panel, labeled b) shows results from a simulation with a reduced α_1 parameter, with parameters $\bar{\alpha}_1 = 0.025$, $\bar{\alpha}_2 = 0.05$, $\beta_1 = 1$, $\beta_2 = 2$. As can be seen in panel b), the particles are more spread out than in panel a), especially seen with the larger white gaps on the bottom layer. Qualitatively, this makes sense as the repulsive force term in the near-field force now has a larger contribution relative to the attractive term. I saw similar behavior when increasing α_2, but increasing either parameter too much can make the particles go unstable. There is a complex interaction of forces and each parameter can have a significant effect on the overall deposit. This interplay is discussed further below.

Another observation I saw from these few frames in Figure 3.17, is that when the particles hit the substrate, they settle and spread out in a fairly inelastic collision. As the subsequent particles land on top of those that land first, they also start to collect into the pile. This behavior is due to a combination of forces, with perhaps the most consequential being the dissipation, or contact damping force, especially after the first collision with the substrate.

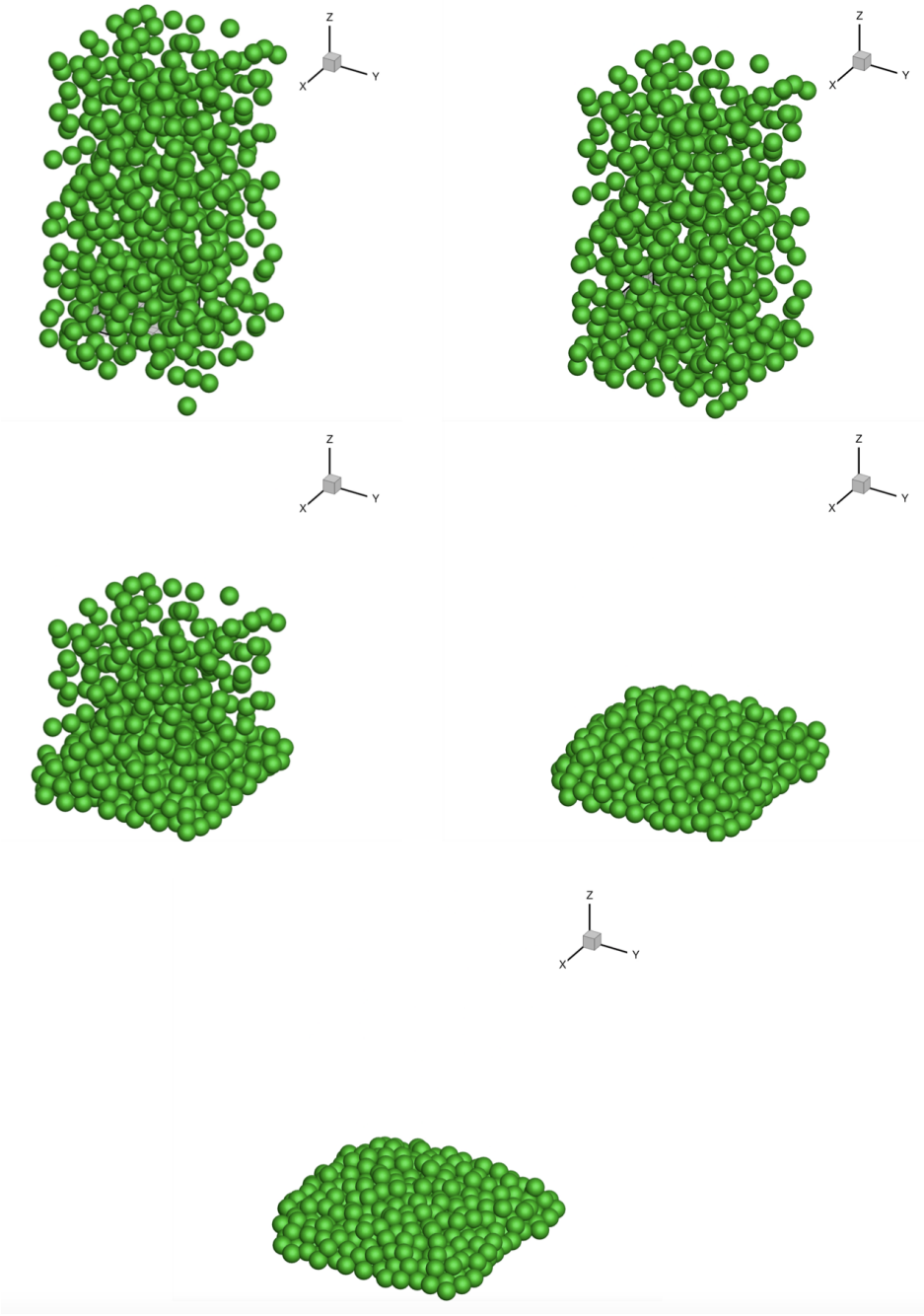

Figure 3.17: Successive frames from a simulation of particles deposited from the first example. The particles are allowed to slowly spread out as there are no sidewall boundary conditions applied in this case.

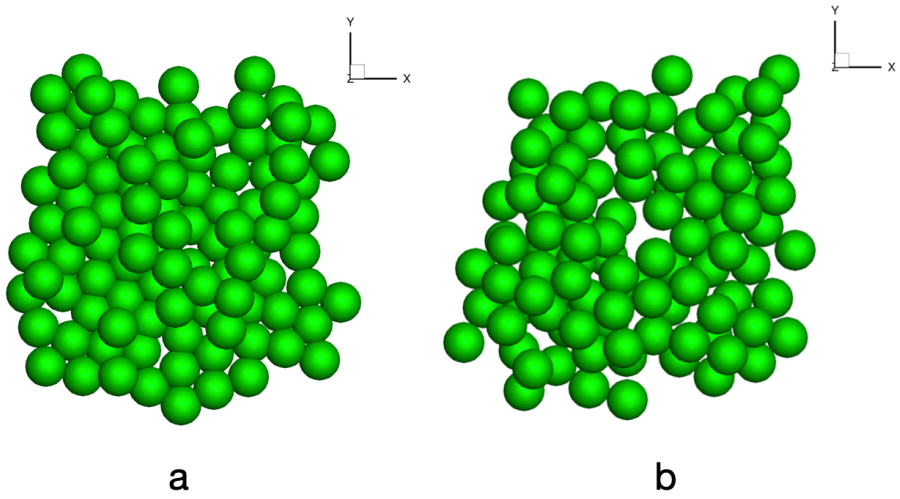

Figure 3.18: Top down view of two separate trials with a) more attractive near-field forces and b) stronger repulsive near-field forces. The particles are more spread out with larger white gaps seen in panel b).

This force defined in Equation 3.17 is proportional to the normal velocity of the particle. Just before the first particles contact the substrate, they will have a relatively high normal velocity, so this dissipation will be higher than in any subsequent collisions. In the first example shown in Figure 3.17, the particles remained in contact with the substrate after collisions, but the behavior changed when adjusted the parameters of the model. In a simulation with a lower damping coefficient c_{cd}, the particles have more elastic collisions with the substrate.

Now this dissipation is not the only force involved with how the particles collide with the substrate. The behavior is ultimately due to a complex combination of many forces involved including the direct contact forces (proportional to the interpenetration of the particles), the Lorentz force from the external electric field, and any bonding or near-field interactions with other particles in addition to the dissipation. The complex interplay between all of these forces leads to the many different possible particle deposit structures. When exploring the parameter spaces to investigate these behaviors, I was also limited by the stability of my time stepping scheme. For instance, if the dissipation parameter is not high enough, particles may have so much acceleration away from the contact point that they diverge and bounce to infinity. This can also occur in situations where the contact compliance parameters are high, essentially resulting in very high forces when particles are in contact with each other and the substrate. If the interpenetration distance is high enough, this can also further increase the contact force such that they diverge. To limit this, I also had to be careful with selecting small enough time steps so the particles in contact didn't have too large of interpenetration distances during contact. My general strategy during development was to

use a smaller time step to make sure particle motion was stable and the particles were able to form a deposit. Then I could slowly increase that time step size in subsequent runs of the simulation to minimize the runtime for a particular set of process parameters. This was a very manual process, and in the future could be addressed with a different approach to time stepping, which I will discuss further below in the future directions for this research section. However, due to the nature of these particles having many collisions over the course of a simulation, I continued to use this brute force approach to determining time step parameters in my examples.

The next observation from this first example is we see that the particles are able to spread out and settle in the z direction so that most particles are touching the substrate, or only forming a few layers above it. This is helpful to see how large particles might fall in a pile when unconstrained, but I also wanted to use this framework to study the structure of deposits that could have many layers. To do that I employed the periodic boundary conditions detailed in the section above. This led into my next example, which used the same model parameters as the first, but now checks conditions when particles are near the sidewalls of the domain. The simulation was carried over a final time of $t_f = 0.15s$ to allow the particles to settle. The periodic boundary conditions allow particles near one of the sides to interact with particles on the other side as if they were adjacent. Frames from this example simulation are shown in Figure 3.19.

In Figure 3.19, the particles are first generated in a rectangular domain using the sequentially random non-overlapping position algorithm described previously in this chapter as shown in the upper left panel. The grey grids show the bounding area of my domain. Next in the upper right panel, the lower particles contact the substrate where they start to build up the layers in the middle left panel. They continue to fall in the middle right panel and settle in the bottom panel. I used the periodic boundary conditions to get more layers in the final deposit shown in the bottom panel of Figure 3.19 than in the deposit from the first example shown in Figure 3.17. When watching the animation of this simulation made of many more frames than shown here, I observed particles near one edge sometimes disappear and then reappear on the opposite edge. This behavior indicated that the periodic boundary conditions were working as intended, and that sometimes as a deposit is settling, particles on intermediate layer could shift their position.

Now to investigate the multiple layers, I used the coordination number as defined in Equation 3.16 to see how it changes as the particles deposit. Figure 3.20 shows the final deposit in panel a) with a plot of the average coordination number over time in panel b).

As seen in the right panel of Figure 3.20, the average coordination number starts low as the particles are initially not within the R_{CN} parameter and counted as nearest neighbors. As the particles fall, they begin to make contact and the average CN starts to increase as more and more particles integrate into the deposit. Near the $t = 0.9s$ mark, the average CN starts to level off as the particles have been driven to join the deposit and are close enough to be counted as nearest neighbors. The particles continue to settle for the rest of the simulation as they shift slightly and the average CN remains fairly steady. This matches the behavior I expected to see well, so this was a positive outcome for the example.

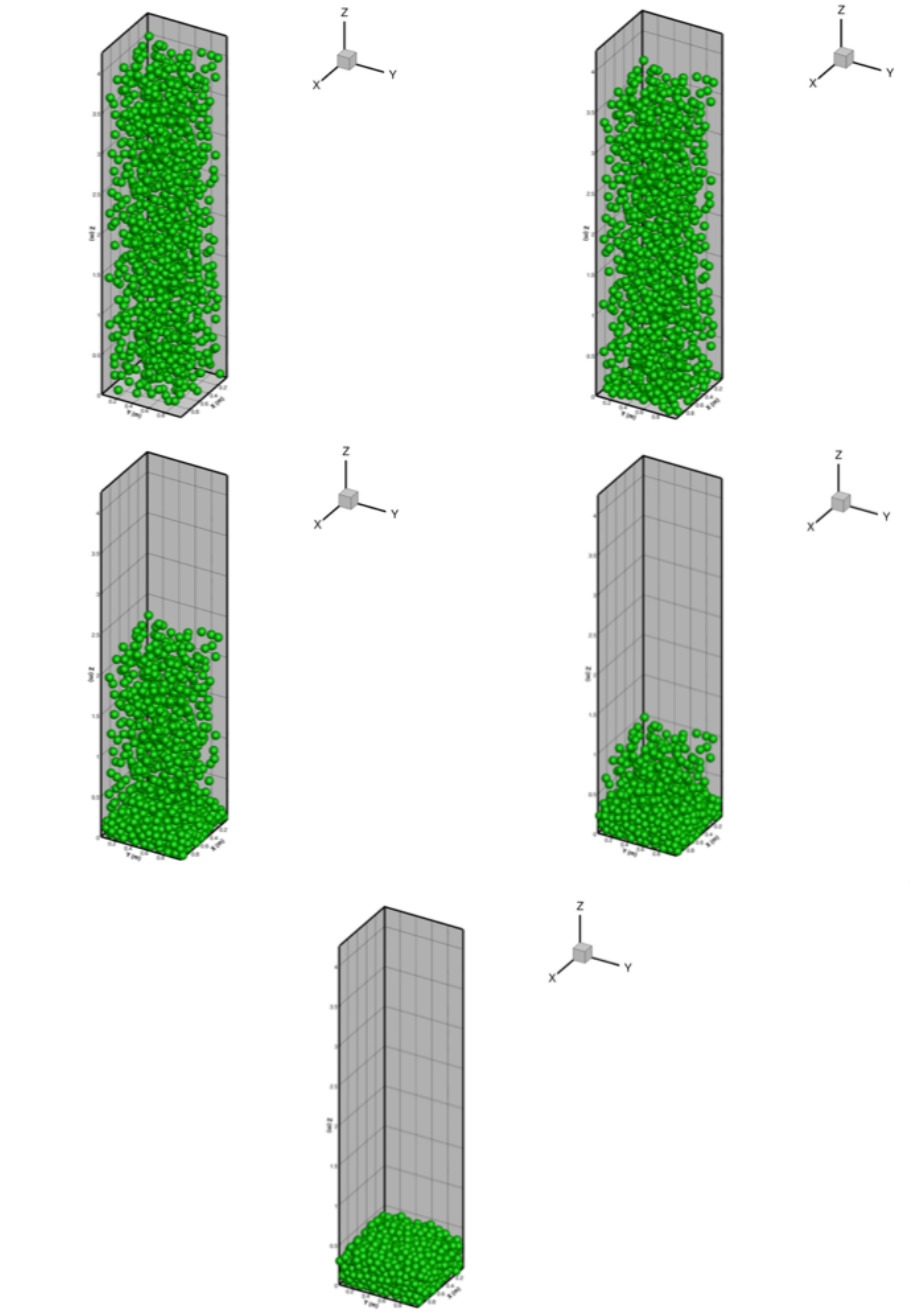

Figure 3.19: Successive frames from a simulation of particles deposited from the second example. The particles are stack up and are contained to the rectangular domain because of the applied periodic boundary conditions.

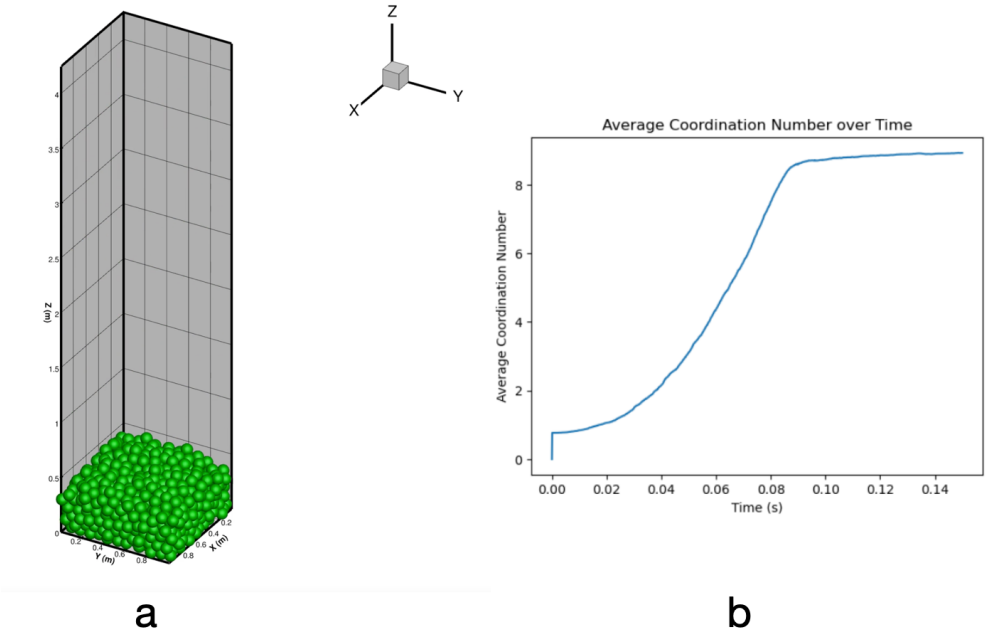

Figure 3.20: a) Final deposit from the second example and b) the corresponding average coordination number vs time throughout the simulation showing an increase as the particles settle near one another.

During development of the model framework, I also tested using solid sidewalls such as in a situation AM with powder bed. These tests showed that my model framework could be used for other applications. In these particular examples, I was focusing more on using the periodic boundary conditions to represent a subsection of the domain. In the future, this framework could be used for full-scale simulations for another application such as the particles in a powder bed, but the high number of particles will still be computationally expensive. Those costs can be addressed with modifications to the simulation framework I discuss further below, or larger computing resources.

The next example I present builds upon the last two, but adds in the use of the variable particle radius. For this example, I investigated how varying the particle radius may effect the overall deposit. This again used periodic boundary conditions like employed in the second example, and used basically the same parameters as the first example. For the simulation shown in Figure 3.21, the mean radius is $\bar{R}_p = 0.05m$ and the variation parameter $\alpha_{rad} = 0.2$ and the deposition is simulated for $t_f = 0.5s$. One more addition was made for these figures, as the color of the particle now represents the coordination number of that particle at the current frame. This is a useful visual aid for quickly seeing which particles have more neighbors.

Starting with the top left panel, the initialized particles show a variation in the particle sizes, as some are small and some are large. The color of the particles also indicates the

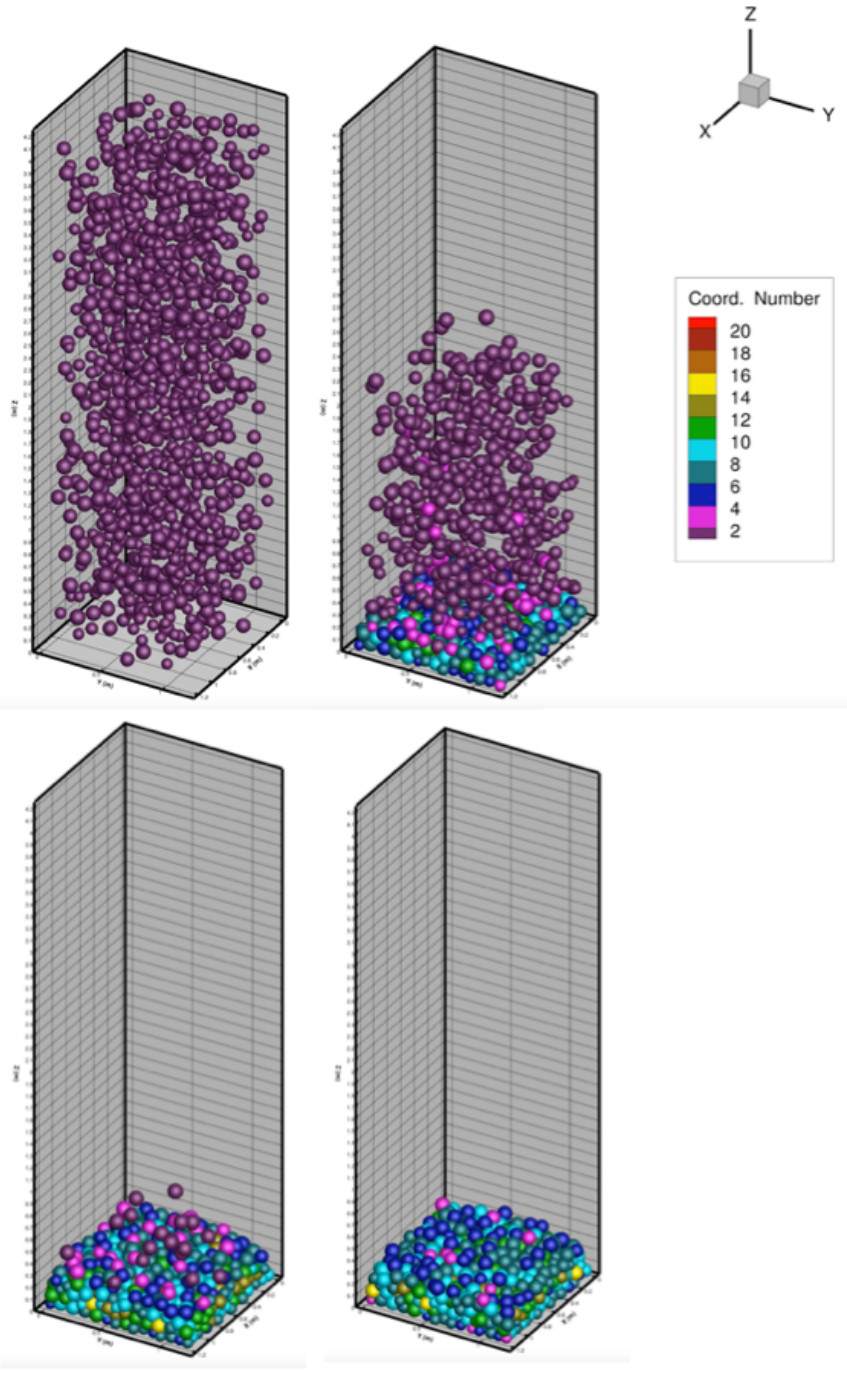

Figure 3.21: Successive frames from a deposit with variable radius. The color bar indicates the coordination number of the particle.

particles all have the minimum number of nearest neighbors (zero), which makes sense as they are generated to be non-intersecting. There is always a small chance that the particles may be extremely close while not intersecting, but none are close enough to be added as a nearest neighbor for the coordination number. The next panel in the upper right shows the particles falling and starting to form the deposit on the substrate. The colors changing indicate the deposited particles have higher coordination numbers than those still being driven towards the surface. The third panel in the lower left has almost all of the particles landed in the deposit, before seeing them fully settled in the last bottom right panel. In the third panel, I see several of the top particles with a purple or magenta color, and then in the last panel they have mostly changed to blue. This indicates that with these parameters, the particles will settle into spaces that bring them closer to the neighboring particles as the driving Lorentz force combined with the inter-particle near-field and contact forces result in the final structure.

Then move towards describing zoomed in figure 3.22- more details final deposit and comment on the slightly higher average CN

I show a more zoomed in view of the final panel in Figure 3.22. Panel a) shows the deposit in more detail while panel b) shows a plot of the average coordination number over time of the deposit.

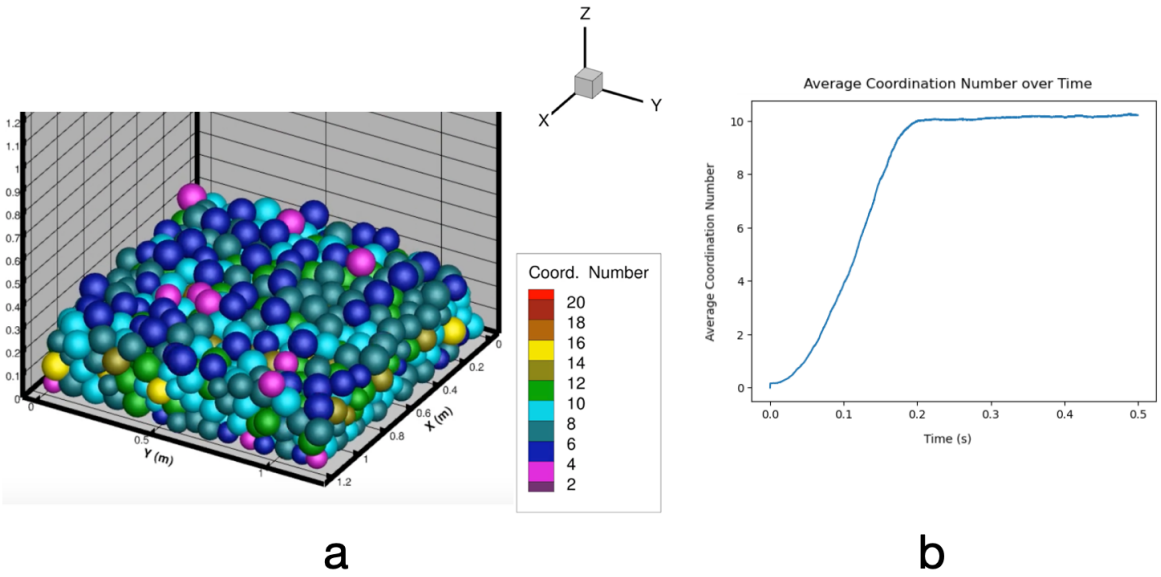

Figure 3.22: a) Zoomed in image of the final frame from the third example deposit with color indicating the coordination number of the particle. b) Plot of average coordination over time for this deposit.

With the addition of the variable radius and the color, I can make a few new observations compared to the second example. First it can be seen that the majority of particles appear

to have a coordination number around $8 - 12$ in the green and teal range. These particles are mostly in the middle layers as they are in contact with the most neighbors above and below them. I also note that a few of the particles are in the yellow range, with coordination numbers around $12 - 16$. These few particles are also in the inner layers, but also appear to be larger in diameter. This slightly larger diameter Those that are visible on the outer edges of the deposit are interacting with the particles nearest them as well as particles on the opposite edge due to the periodic boundary conditions. As expected, I also see more particles on the top and bottom layers with lower coordination numbers. It also appears that smaller particles are able to settle further down in the deposit than larger ones. This behavior can also be a potential cause of the apparent increase in average coordination number, as the smaller particles may be able to settle in contact around larger particles that will then have higher coordination numbers as opposed to the case with uniform particle radius.

In summary, these several examples showed the capabilities of my current model framework to investigate deposits. The first example looked at uniform particles depositing on a flat substrate with no sidewalls and being able to spread out. I briefly looked into the qualitative effect of the near-field forces, noting an observable increase in space between particles as the parameters were adjusted. The second example showed the effect of the periodic boundary conditions, which led to more capabilities in increasing deposition layers while maintaining the same number of particles. Essentially representing a small area or representative volume element of the deposit domain, I used the coordination number as a way to investigate how the particles were settling over time. This behavior was further explored in the third example where I added variation to the particle radius and observed how that effected the deposit. These examples are the preliminary capabilities of the modeling framework, and future directions for modifications and improvements are discussed next.

3.4 Future Directions for Research

So far I've shown some preliminary examples of the capabilities of my simulation framework, but there are several ways in which this framework can be improved and several studies that would be immediate extensions of continuing research interest. The initial improvements to the simulation framework are more related to model efficiency, as one of the main goals of this project was to maximize speed. The future studies are also further explorations into the one of the original motivating applications of this project - simulating deposits created with EPD.

Simulation Framework Improvements

Currently, I have implemented my simulation framework in Python in a simple method which is helpful for clarity for the user, but not necessarily the most efficient. One of the main bottlenecks of my current implementation is in the pairwise calculations used for determining distance and applying the contact or near-field forces. For simplicity, I currently

have the simulation set up to run in two for loops which checks each particle against every other particle, but this becomes an $O(N^2)$ problem, which does not scale as well with large numbers of particles. For my simulations, I tested and debugged the code with smaller numbers of particles, and then expanded them for the examples presented above. Running these simulations on my laptop, with the order of 10^5 or 10^6 time steps would take around $6-8$ hours. This was further improved by the implementation of Numba, a just-in-time compiler for Python which converts the functions written in Python to a machine code version that runs more quickly [31] on my laptop's CPU. Using Numba to compile my functions for force computations sped up my simulations significantly, bringing it down to $1.5-2.5$ hours for a simulation with $N_p = 1000$ particles. Now this is quite an improvement for the current conditions, but while testing the simulation with parameters similar to the EPD case, I found that I need to use a much smaller time step size for stability with the smaller particles. This will inevitably increase the total runtime, even with limiting the number of particles to $N_p = 1000$. However, this current runtime for particle simulations on a laptop is still tractable for many applications as opposed to using models that require more complex computational resources like those running LAMMPS as presented by Giera et al. [22] [23].

There are several avenues I could take to work on increasing the efficiency so the number of particles can be increased while limiting the increase to computational cost and runtime. One method would be to use Verlet Lists, possibly in a combination with cell lists or "binning". Verlet lists essentially sweep through all particles and make a list of nearest neighbors for each particle. Then, when running force calculations, the loop checking for inter-particle forces only checks for particles on each list, as opposed to the full number of particles. As particles move through the simulation, these Verlet lists will need to be updated to maintain accuracy, but they present a big upside since the $O(N^2)$ operation is not being performed every single time step [51]. Cell lists or "binning" is a technique in which the domain is broken down geometrically into "bins", and only particles in neighboring bins are checked for inter-particle interactions. This is graphically shown Figure 3.23 where the particle of interest resides in the red bordered neighborhood and the adjacent green bordered neighborhoods will be checked for interactions. Many DEM simulations utilize Verlet lists and/or "binning" and when implemented they can reduce the operation from order $O(N^2)$ to $O(N)$ [21] [45] [51].

Another improvement would be to utilize parallelization to spread out computations on the particles. In my case, I just used one process to run all computations in the simulation, most laptops now have multiple processors and those can be used to run separate computations in parallel. Using Python's multiprocessing package, calculations of different forces or processes computing forces on all particles in different bins could be turned into individual subprocesses that are run on different processors [40].

One other potential improvement to my framework would be to implement an adaptive time stepping scheme with an implicit solution method similar to the one used by Zohdi [66]. In my current simulation, I have used a trapezoidal time stepping scheme, but stayed on the explicit side, utilizing only the Forward Euler method so far. As mentioned previously, this requires small time steps to maintain system stability, and since a goal of this is to

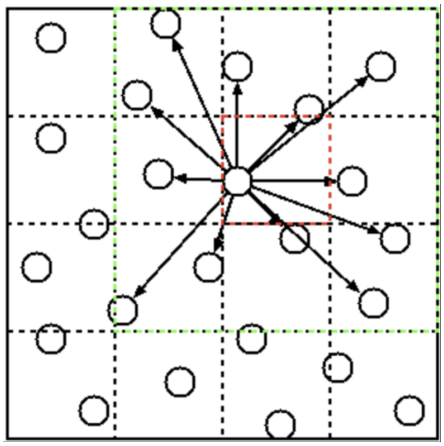

Figure 3.23: Graphical representation of the cell list, or "binning" algorithm from Rokhlin [51].

reduce runtime, a potential method to improve total runtime would be to investigate implicit methods as well. These methods are generally more stable and can use a larger time step, but require iterations within a time step to converge on a solution. Therefore, there is a trade-off between the runtime saved by increasing the time step and a potential increase due to iterating. Studies with this framework would need to be tested to see how those trade-offs work out for these particular applications.

Future Studies with EPD

Studying colloidal depositions via EPD was one of the main applications of interest to motivate this work, so performing more studies of that application would be the immediate direction for future studies. In the model presented by Giera et al. using their implementation in LAMMPS, they performed studies on deposition by varying the Péclet number and the debye length λ_D [23], which essentially varies the near-field interactions of their particles. These studies can be similarly performed using my simulation framework on a laptop by varying the field strength E to vary a simulation's Pe, and by varying λ_D as well as the near-field parameters, the α's and β's to study the effect of the near-field forces. In their studies, Giera et al. observed trends in the relative order of the deposits which are summarized in Figure 3.24.

Qualitatively, the first trend seen in Figure 3.24 is a decrease in relative order of the deposit as Péclet number increases due to a higher driving force from the external electric field forcing particles to settle closer together and in a more amorphous deposit. The next trend shows that for lower Pe, there maybe an ideal ratio of $\frac{a}{\lambda_D}$, or particle radius to Debye length, for which order is increased and can potentially be maximized. This trend was seen to some extent for the range of $Pe = 26.5-214$, and not really seen for the higher simulations with $Pe = 429$ and 858. This indicates an interplay of the attractive and repulsive near-field

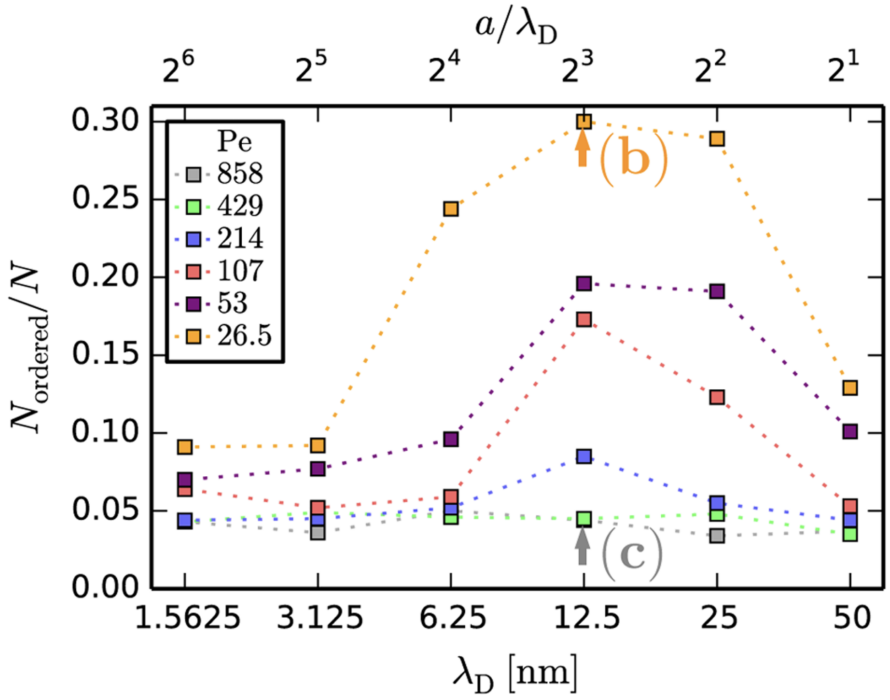

Figure 3.24: Plot of relative order $\frac{N_{ordered}}{N}$ vs Debye Length λ_D for simulations with different Péclet numbers from Giera et al. [23].

forces may be a defining factor in the relative order of deposits with Péclet numbers that are low enough. This is an immediate direction of interest for future trials with my simulation framework to see if similar trends are seen with a simpler implementation that can run on a laptop.

3.5 Summary and Conclusions

This chapter discussed the simulation framework I used to study field-driven AM processes. I first talk about the details of my DEM implementation in Python, including the problem overview, details about the assumptions and physics accounted for, and three sets of verification and validation studies performed using my framework. The sets of studies started with the simple diffusion case, then moved on to investigate electrophoretic velocity studies. Finding good agreement with the analytical values in those first two sets of studies, I then moved to the third set of studies of particle deposition. Using several numerical examples, I explored the behavior of particles depositing under process parameters similar to electrospray deposition on a flat substrate when allowed to spread and when constrained by periodic boundary conditions so they would deposit in multiple layers. Adding in variable particle

radii, I also explored the effect of a potentially more realistic deposit where the particles are not all a perfectly uniform size.

These studies showed the current capabilities of my simulation framework that can simulate a particle deposit and then be used to analyze the results qualitatively by inspection and quantitatively by looking at the coordination number of particles as a measure of relative order in a deposit. Finally I discuss several future expansions and future directions for research opportunities with this simulation framework including more exploration into deposits created with EPD. This simulation framework can eventually be used to aid in process optimization in conjunction with experiments, which I discuss next.

Chapter 4

Particle Tracking Studies Towards Enhanced Understanding of EPD

This chapter will discuss the preliminary experimental work performed to enhance understanding of the EPD process which highlights an opportunity for further studies of this application. Quantitative data in the form of particle trajectories can also be used to validate and verify simulations of the EPD process like those discussed in Chapters 2 and 3, further advancing those tools for process understanding and optimization. The experimental work here was done at the Lawrence Livermore National Laboratory, within the experimental facilities of the Materials Engineering Division and the Center for Engineered Materials and Manufacturing. The work presented in this chapter could not have been done without all of the mentoring and equipment training and expertise of the scientists there, and for that I will always be grateful.

4.1 Motivation

As mentioned earlier in Chapter 2, most of the development and studies of EPD have been performed *ex situ*. These studies have investigated the kinematics of particle depositions under EPD through activities such as measuring deposited mass at different time instances or removing samples from different stages of deposition to investigate the deposit structure via SEM imaging [19]. While these methods are useful for an initial understanding of how particles deposit and what structures may form, the details of how particles interact with the substrate and with each other during deposition and this underlying effect on the structure are not well understood. Specifically, the mechanisms behind the empirically observed f-factor described by Hamaker [25] are not able to be fully observed with the *ex-situ* techniques.

To gain a better understanding of those particle-particle and particle-substrate interactions, *in-situ* observation would provide further insight beyond that provided by the *ex-situ* counterparts. The ability to observe and track particles as they deposit will provide that insight to fill some of the gaps in knowledge of particle depositions under EPD. To the best

of my knowledge, there has not yet been published work of 3D *in-situ* observation of EPD, and the following presented work will give details on the early steps taken towards that goal.

Objectives/Goals

The overall goal of this work is to create and a platform that can be used to observe particles deposited via EPD *in-situ*. The observations will rely on particle tracking methods to provide trajectories of those particles throughout the process. These trajectories can then be studied to further understand the relevant physics that drive particles to deposit and form the structures we see as an end product. With real-time observations of these particle depositions, this platform can be used to provide fundamental insight into the process dynamics, as well as be used as a tool for process optimization when combined with simulations. The particle trajectories under different process parameters can be used in conjunction with simulations like the one described in the bulk of this work and particularly Chapter 3. Better informed simulation tools can then guide experiments towards parameters that produced desired results, such as a more crystalline structure. Experimentally verified simulations will be particularly helpful as the EPD process is evaluated and further developed to produce various components with desired structures. In summary, the goals of this work are:

1. Provide a platform to study *in-situ* 3D trajectories of particles during EPD under a variety of experimental parameters.

2. Provide particle trajectories that can be compared to and inform simulations to more accurately capture the complex behavior of particles during EPD for future process optimization.

Due to time constraints and the onset of the COVID-19 pandemic, the full realization of these goals was not achieved, but this preliminary work can serve as a starting point for further investigations.

4.2 Methods

This section discusses the experimental methods used to perform *in situ* observations of EPD on a particle tracking system using fluorescence microscopy.

Fluorescence Microscopy

To visualize the particles, a fluorescence microscope (Zeiss Axiovert 200) was used. In this technique, fluorescent tagged particles were illuminated with a specific wavelength of light which then emit a different wavelength of light that will be imaged. The details of my specific fluorescent particles are described below. A fluorescence microscope is similar to a conventional light microscope but also contains filters to allow specific wavelengths of light

to pass through the lens [11]. These filters allow for the higher energy light (the excitation source) to reach the target particles and the fluoresced lower energy light (the emitted light) from the particles to be viewed by the detector. The setup used in this work is detailed further below, but essentially required a high energy light source, the fluorescence microscope shown in Figure 4.1 with filters for excitation and emitted light, and the detector which in this case was a CCD camera used to record the images.

Figure 4.1: Fluorescence microscope used for particle tracking experiments.

For this set of experiments, the particles of interested were fluorescently tagged with Fluorescein isothiocyanate (FITC), a common fluorescent dye that is excited by blue light with a wavelength of $495nm$ and emits green light with a wavelength of $519nm$.

Fluorescent microscopy was chosen for this application for several reasons. First, the high-contrast images aid in preparing the images for analysis using the particle tracking software as the particles will stand out well against the background. The specific software I used for particle tracking, GDPTlab, requires darkfield images, or images with a dark background and the particles highlighted as the bright objects, so this was setup directly for that workflow. Secondly, the particle sizes of interest in EPD can range down into the 100 nm range as mentioned in Chapter 2, but the light emitted will be a larger perceivable object. This particle size range is near or below the diffraction limit of most conventional light

microscopes, where they will not easily be able to resolve the particle [14]. With fluorescent particles, the image is of the emitted light that forms an Airy disk, which is larger than the particle. This Airy disk pattern in the particle tracking images can also provide information about location of the center of the particles that can be used to compute the position with sub-pixel precision [15]. An example of the Airy disks observed with my particles can be seen in Figure 4.3.

Another method of viewing particles of this size is confocal microscopy. In this technique, the resulting image can be observed at a higher resolution, but is limited to the focal plane that the microscope is focused on. To change the focal plane location, the objective lens or sample stage must be moved, which limits the ability to quickly see objects as they move into and out of the focal plane. As the main focus of this work is to observe particles depositing on a substrate via EPD, this method will be too slow to resolve particles that may be moving on the order of $100\frac{\mu m}{s}$. Therefore, fluorescence microscopy with its ability to image the light emitted by small particles used in conjunction with the particle tracking technique detailed below to track particle positions in 3 dimensions is the chosen method.

Particle Tracking - General Defocusing Particle Tracking

As mentioned in the previous sections, the goal of this experimental work is to track particles depositing on a substrate via EPD. To achieve that goal, the small particles are imaged using a fluorescence microscope and the trajectories or positions over time of the particles are measured using a particle tracking technique, namely General Defocusing Particle Tracking (GDPT) developed by Barnkob et al. [3] [5]. The GDPT technique is a method of particle tracking that can resolve positions in 3 dimensions using a single camera setup. The technique is part of the Particle Tracking Velocimetry (PTV) family of methods and has been reported to be capable of tracking particles moving up to $1\frac{m}{s}$ with the single camera [49] [3]. For motion in the image plane (x, y), GDPT uses standard particle tracking algorithms to resolve the positions of particles. To gain information in the depth direction, GDPT relies on a "calibration stack" of images shown in Figure 4.2. The images are taken at different z positions to record what the particles look like at different levels of defocus. A cylindrical lens is added to the optical train of the microscope to break image symmetry around the focal plane, which provides a unique image for each z position in the calibration stack. The images for the calibration stack are taken before making a particle tracking measurement, as they are taken by moving the objective or stage to scan through the z direction. An example calibration image from the first set of trials is shown below in Figure 4.3. That trial used 500 nm FITC labeled silica particles. As can be seen with the scale bar, the light emitted from the fluorescing particles can be captured in larger area than if just the particle itself was imaged.

Once the calibration stack images are ready, GDPT software can then perform a particle tracking measurement by analyzing a time-series of images. In subsequent frames of images, particles will be identified and tracked as they move. The software uses standard particle tracking algorithms to track position in x and y, while the z position is determined by

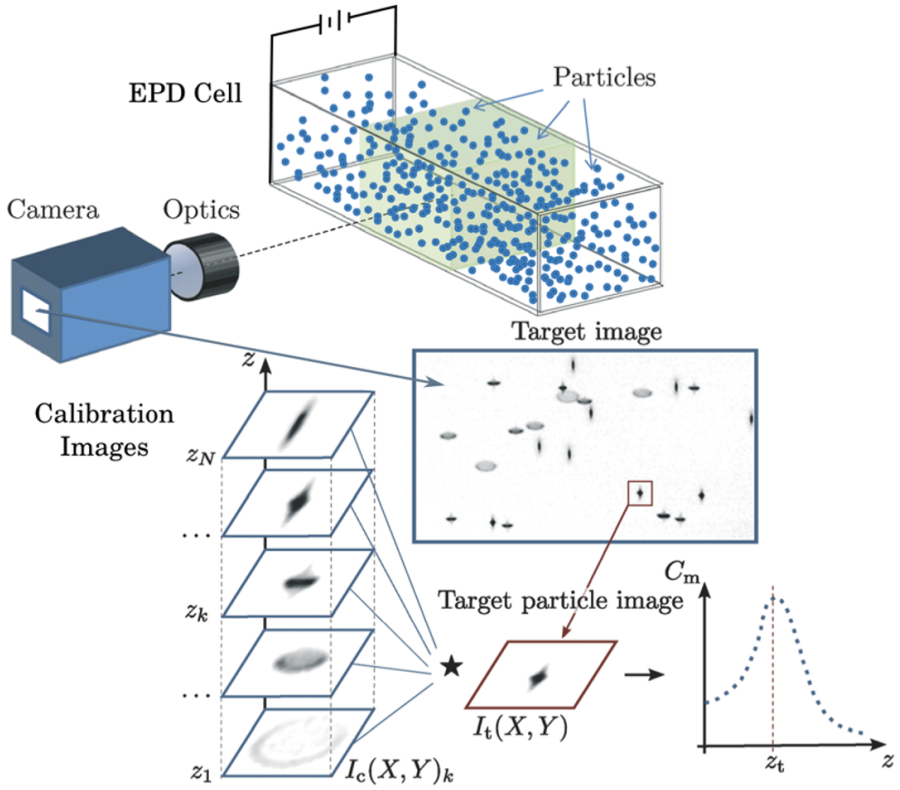

Figure 4.2: Schematic of the GDPT setup and process. Image adapted from [3].

comparing the current image of the particle with the calibration stack. A correlation value is computed for each calibration image, and the maximum correlation will provide the estimate for the z position. Finally, the time series of particle positions is output as a result of the measurement.

GDPT is shown to be an advantageous technique for this application for several reasons, chiefly among them being the singular camera setup. The single camera setup helps with experimental setup cost and is simpler with limited space, making GDPT more accessible for a wider group of experimentalists. Particularly for tracking particles depositing via EPD, the focus is mostly on the $x - y$ plane, but also still interested in motion in the z direction. Since the deposited films are mostly thin in the z direction and we can still observe the kinematics of the particles in that thin region, the extra complication of adding multiple cameras is unnecessary.

The software component of GDPT, GDPTlab is available as a "black box" package for free from the developers [3], [13]. While it is unfortunately not truly open source, there is good documentation and tutorials so understanding how to use the software is convenient. GDPTlab is implemented in Matlab and provides a Graphical User Interface for the user. A

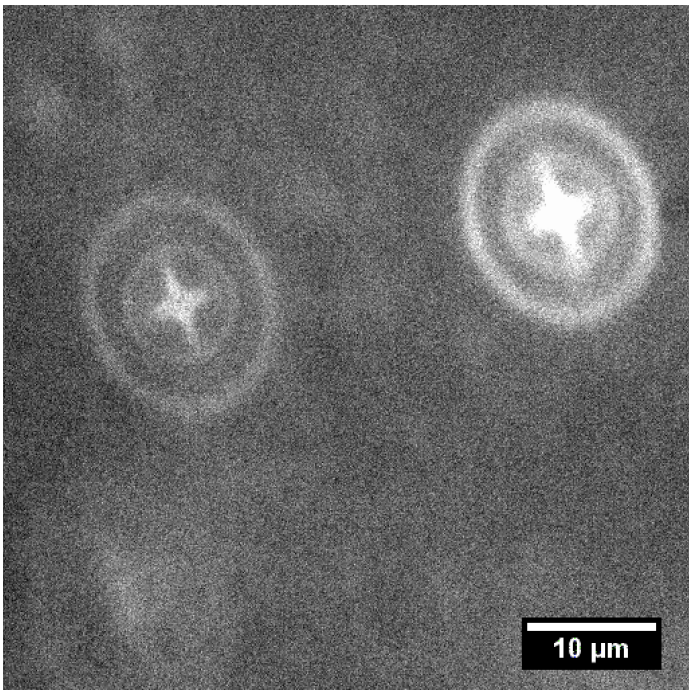

Figure 4.3: Example calibration image taken for 3D GDPT analysis of 500nm silica particles. The Airy disk from the light emitted is larger than just the particle size.

more recent iteration of the software, DefocusTracker, has become available and continues to be developed by the team of Barnkob et al. [4]. The analysis below used the earlier version, GDPTlab.

4.3 Verification Experiments and Results

Using the techniques described above, the experimental work progressed to construct the particle tracking platform and perform preliminary verification experiments. Starting with the simplest case of particle diffusion, followed by observations of particles deposited under EPD.

4.3.1 Diffusion Experiments in 2D

The first experiments conducted were 2D experiments to begin to develop the workflow for the particle tracking experiments. As a first trial, the system was used to track particles in the simplest configuration: diffusing in a still fluid.

The goal of these experiments is to use the particle tracking setup to track diffusing particles in 2D. Particle trajectories are analyzed using Mean-squared displacement and used

to compute the diffusion coefficient. The experimental diffusion coefficient is then compared to the result from the ideal Stokes-Einstein relation as one verification step of the particle tracking setup.

Setup on microscope, details of particles and solution

For the first set of diffusion experiments, the system setup was fairly simple. In this case we used the fluorescence microscope, a Zeiss Axiovert 200 with a Zeiss LD Achroplan 63x/ 0.75 Korr Ph2 objective. The objective lens had a moderately high numerical aperture (NA) of 0.75 to allow a higher intensity of observed light. As mentioned in the review article by Lichtman and Conchello, the intensity of observed light in a fluorescence microscope system is proportional to $(NA)^4$[34]. Higher NA objective lenses such as those designed to be used with oil instead of air could further improve the intensity of light, but for this first test the air objective was sufficient. The diffusing particles are suspended in fluid, water for my case, and are imaged by using a pipette to add a drop to a cleaned glass microscope slide. The procedure for cleaning the slides is noted in Appendix A. A basic schematic of this setup is seen below in Figure 4.4. The microscope used a Lumen Dynamics X-Cite 120Q Fluorescent Light Source and captured particle images with an Andor Zyla 5.5 CMOS camera. The microscope was also fit with a Zeiss FITC filter cube set to provide the proper wavelength of excitation light ($495m$) as well as allow the emitted light ($519nm$) to leave the sample and be detected by the camera.

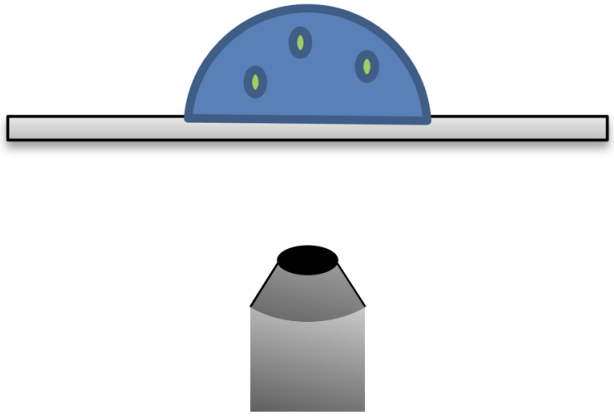

Figure 4.4: Schematic of diffusion experimental setup. The particles are suspended in water and a drop is imaged on the microscope to observe the diffusing particles.

The particles used for these experiments were 500nm diameter FITC-labeled silica particles. The particles were ordered from Bangs Laboratories and are suspended in water at a percent concentration of 1% by volume. For imaging, I wanted to start with less particles

so the images would only be tracking a few particles at a time. Aiming to start with images where I could see 5 or less particles in the frame worked well for my initial tests of the workflow. For the imaging suspension, I created a new suspension of the particles and deionized (DI) water. Adding 50 μl of the particle suspension to 1 ml of water resulted in suspension of approximately 0.05% by volume where images with only a few particles in the frame could be taken. I stored the suspensions with FITC-labeled particles in amber vials to keep them in the dark to extend the life of the fluorophores and prevent early photobleaching, or loss of fluorescence [34]. Before imaging the particles, I wanted to make sure they were properly suspended and dispersed in the solution. Particle clumping or agglomeration became an issue in some of the trials, especially if the suspensions had been sitting in storage for a while between runs. To prevent this, I first mixed the vial of suspension on a vortex mixer for a few seconds and then placed it in a sonicator (Vevor Industrial Ultrasonic Cleaner) for 1 hour to break up any clumps of particles before imaging.

With the microscope set up for fluorescence imaging, the glass slides cleaned and prepped, and the imaging suspension mixed, the data collection could begin. I used a 0.5 mL transfer pipette to add a few drops of suspension onto the cleaned glass slide on the microscope stage. Finally, I focused the microscope at a plane where I could see a particle or a set of particles diffusing. I started with the power source's shutter on the lowest setting to limit the illumination to the lowest level while searching for particles and closed the shutter completely when not needed - this delayed photobleaching, or a loss of fluorescent signal, of the fluorescent particles [34]. With this concentration of particles, it sometimes took a bit of time to find a good viewing window with several particles, but I would generally start with a lower magnification objective (20x) to find a good region before switching to the higher objective (63x) when the particles were located.

Once the particles were in the view window of the microscope, I captured their images with the CCD camera. The Andor Zyla 5.5 camera was attached to the microscope and was controlled using Andor Solis software on a PC [2]. I used Andor Solis to view and save the images observed by the camera. Once the image in the computer preview was located on particles well, I opened the light source shutter all the way to maximize the excitation light and the emitted light for the image. The software has an option to automatically adjust contrast that I was able to use most of the time, but would sometimes need to manually adjust contrast and other acquisition settings like exposure time to get a clear image. If the particles were dim, increasing the exposure time would allow more light to be captured in an image, but also limited frame rate. Since these experiments were trying to capture particle diffusion, the goal was to take an acquisition over time with enough frames to capture Brownian motion. In Andor Solis, this movie acquisition was called a kinetic series, and for that I could determine exposure time, or alternatively frame rate, and the total duration. Frame rate and total duration of the image acquisition were limited by the aforementioned need to allow enough light into the camera for a good image (exposure time) as well as the RAM available to the computer. Due to these constraints, I found a good combination for my setup to be an exposure time of 0.1 seconds, or a frame rate of 10 frames per second, and a total duration of 13 seconds. This resulted in 130 frames in each acquisition. Finally

each frame of the video was saved as a .tiff file to save the highest resolution as possible for each run of diffusion observations.

In summary, the experimental procedure was as follows:

1. Clean glass slides, prepare imaging suspension, turn on microscope and light source.
2. Use transfer pipette to add 2-3 drops of suspension to the glass slide.
3. Set light source shutter to lowest setting and use eyepieces to locate particles.
4. Preview camera image in Andor Solis with acquisition settings for kinetic series.
5. Open light source shutter all the way, adjust contrast as needed, and take acquisition.
6. Close light source shutter, save acquisition data, and prepare to repeat from Step 3 as needed to take more data.

I used the basic procedure above throughout the development of the system and workflow for imaging fluorescent particles. The data discussed below is the culmination of efforts in determining system parameters that provided useful raw images. Details on image processing for analysis will also be detailed in the section below. As mentioned above, the video of each "run" was typically set to be 130 frames over 13 seconds. Saved in this way, the full .tiff files were 5.29 Mb per image, which results in a total of 687 Mb per run. Throughout the development and data gathering stages of this project, many iterations were recorded so this created quite a large amount of data. The challenges large amounts of data were:

1. Data storage
2. Data transfer/communication

The first challenge, storage, was more easily dealt with by both having access to a large hard drive and by deleting old files after they've been used for analysis. The second challenge was determined by the communication limits of the camera and computer. Even though the camera could capture the video in real-time, the computer still required several minutes to save the files corresponding to 13 seconds of recording. This time delay was factored into planning experiments as the camera had to save all files to the computer before taking a new recording. For these experiments with the droplets, time between recordings contributed to an increase in particle suspensions used because over time the suspension would begin to evaporate on the slide. Planning accordingly for these challenges and limitations will aid in future experiments.

Analysis - Mean Squared Displacement and Stokes-Einstein Relation

Using the experimental setup described above, we now have a timeseries of images of diffusing particles. The end goal of this analysis is to compare the diffusion coefficients measured in

the experiments with the diffusion coefficient analytically described by the Stokes-Einstein relation. This analysis is similar to the diffusion study analysis described earlier in Chapter 3 with the main difference being the source of the position data. The next step in analysis is making a GDPT measurement to extract particle positions over time and then using the Mean Squared Displacement (MSD) to calculate the diffusion coefficient.

To make a GDPT measurement, I started with the raw timeseries images from the experiments. Depending on the conditions of the images including contrast, noise, and background (lightfield or darkfield), they may need some preprocessing before using GDPTlab [13]. In early trials, I used non-fluorescing particles and took brightfield images and for these trials needed to invert the images for use in GDPTlab. To invert the images I used the "invert" function in ImageJ [50]. The results shown below were taken with fluorescent particles. For the fluorescent particles, the background is already dark so there was no need to invert the images. If there was noise present, ImageJ was helpful again as I could use the thresholding function as needed to accentuate the difference between particles and the background. By setting a threshold value, the image could essentially increase the contrast between pixels that were part of a particle and those that were not. I would use this in particular situations where the Airy disk of a particle started to blend in with the background, possibly sometimes caused by extra background light present in the image. Finally if excessive noise was present in the image, I used a median filter to smooth out the changes in pixel value in the image. For most cases a 3x3 median filter was sufficient. GDPTlab also had some image processing options, but ImageJ had a more expansive set so I chose to use that, especially when developing the workflow to see how different options worked when experimenting with the GDPTlab inputs.

Now with a set of processed images, I could make the GDPT measurement using GDPTlab. For this first set of experiments I simply used the 2D measurement function to track positions in the $x-y$ plane. I started trials with calibration images and using the 3D measurement function, but unfortunately due to time constraints was unable to fully develop that process and discuss it here. That will be discussed further in the future directions section. The input for the measurement was the timeseries of preprocessed images and scaling values for the dimensions. I used a microscope stage micrometer, essentially a microscope slide with a ruler etched onto the surface, to determine the scaling values in units of length per pixel for calibrating the $x-y$ dimensions. During development of this process, I used image sets taken with and without the cylindrical lens in the optics train. For images without the cylindrical lens, the calibration value was symmetric in both directions, so the value of length units per pixel was the same. For the case with the cylindrical lens, the values are asymmetric and were measured accordingly. With those loaded into the GDPTlab interface, it then performs the calculations and outputs the trajectories over time in the form of a Matlab object that contains the positions and displacements of the particles in the timeseries as well as a graphical summary.

An example of a particle image and the graphical outputs from GDPTlab are shown in Figure 4.5 below. In this example measurement, 3 particles were detected and their positions in time were plotted as a point cloud in the top figure (shown on a 3D grid by default even

though the measurement was 2D). The bottom left figure shows the displacements in the x and y directions. With the default scaling set by GDPTlab, we can see that the displacements are approximately symmetic in the x and y directions as we would expect. The bottom right figure shows the displacements in the x and z directions, with the z direction showing no displacement since it is a 2D study.

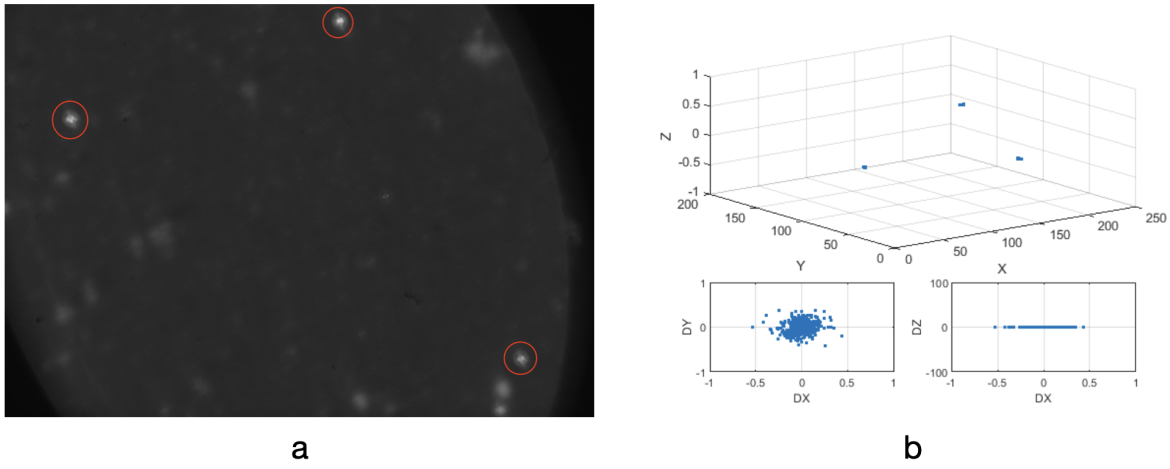

Figure 4.5: a) Example of image from timeseries with detected particles circled in red. b) Graphical summary output from GDPTlab showing positions and dispacements of the particles from the measurement.

After performing the GDPT measurement with GDPTlab, I use the position over time data to compute the MSD similar to the method described in Chapter 3. Recall, the MSD can be related to the diffusion coefficient by Equation 3.30 [8]:

$$\langle \Delta \boldsymbol{r}^2(t) \rangle = 2nDt$$

where $\langle\rangle$ is the ensemble average, $\Delta \boldsymbol{r}$ is the displacement of the particle, n is the number of dimensions (i.e. 1, 2, or 3), D is the diffusion coefficient, and t is time. The trials with results reported below each had 2 or 3 particles tracked in the timeseries of images. Since the position data from GDPTlab was output in Matlab, I also wrote my own code to implement my calculations for the diffusion coefficient in Matlab [36]. I used the position data gained from the GDPT measurement to compute the displacements at different instances in time for the ensemble average which also averages the displacements across multiple particles. Then I computed the MSD and plotted it against time, similar to the plots shown in Chapter 3. I used a polynomial fit to determine the fit line slope and compute the resulting diffusion coefficient following Equation 3.30.

To verify these results, I compared the experimentally derived diffusion coefficient with that computed using the Stokes-Einstein relation. Again, this follows the analysis performed

in Chapter 3. Recall from Equation 3.31, the Stokes-Einstein Relation as derived by Albert Einstein defines the diffusion coefficient, D to be [53]:

$$D = \frac{k_B T}{6\pi\eta r}$$

where k_B is the Boltzmann constant, T is the temperature, η is the absolute viscosity, and r is the particle radius. Using this definition, I directly compute the diffusion coefficient and can then compare it to the experimental diffusion coefficient above. The overall analysis workflow from capturing raw images to computing the diffusion coefficient is as follows and can be seen in Figure 4.6 below.

1. Inspect particle images in timeseries and preprocess with ImageJ as needed.
2. Use GDPTlab to make a GDPT measurement and output particle trajectory data.
3. Compute the experimental diffusion coefficient using Equation 3.30. Code implemented in Matlab.
4. Compute the analytical diffusion coefficient using Equation 3.31 and compare with D computed found in previous step.

Results and Discussion

Using the methods described above, I first computed the analytical value of the diffusion coefficient for my particle system that I later used for comparison. I then took several particle diffusion videos and followed the workflow described above to compute the diffusion coefficient from the experimental setup and compared them with the analytical value computed from the Stokes-Einstein relation. Throughout the course of development, I took many timeseries measurements for particles, but here I report the values for four trials. A longer discussion of why I chose only four trials will be presented below. For the "expected" analytical value, I used the following parameters with Equation 3.31:

- $k_B = 1.3806 \times 10^{-23} \frac{Nm}{K}$ for the Boltzmann constant,
- $T = 293.15K$ since the suspension had been stored at room temperature,
- $\eta = 0.001 \frac{Ns}{m^2}$ as the room temperature viscosity of water, and
- $r = 250nm$ for the radius of the particle

which resulted in an analytical diffusion coefficient of:

$$D_{Analytical} = 8.589 \times 10^{-13} \ \frac{m^2}{s}$$

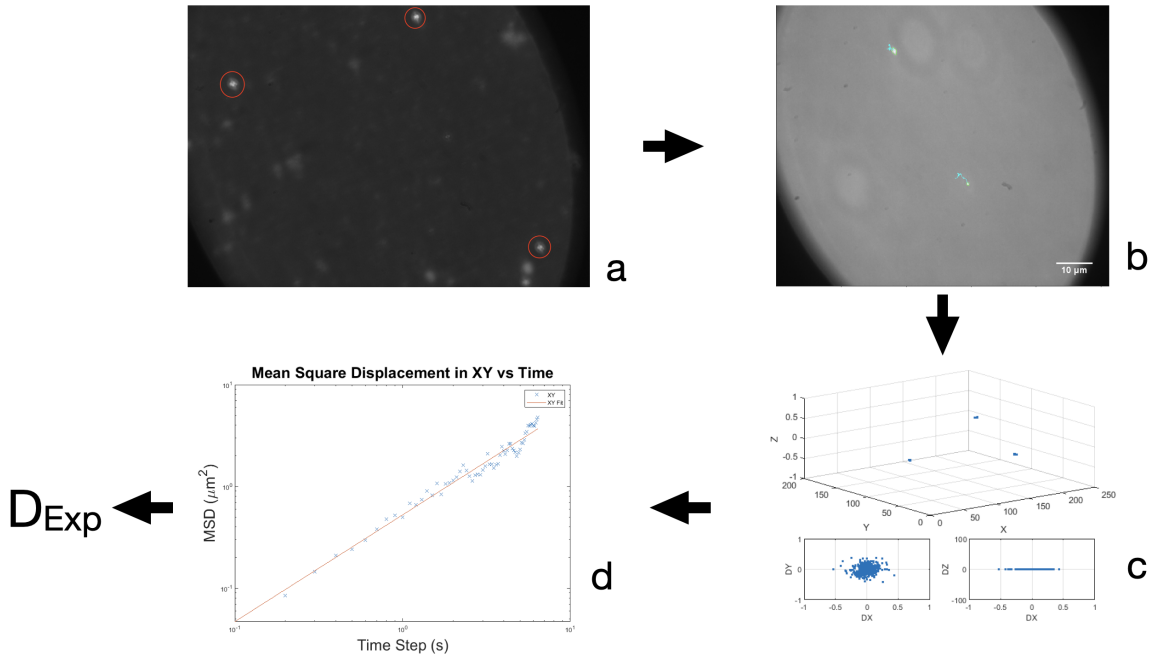

Figure 4.6: General analysis workflow for diffusion experiments. a) Start with particle images. b) Images loaded to GDPTlab - example of image from timeseries with tracks from GDPTlab. c) Complete GDPT measurement to produce trajectories. d) Compute diffusion coefficient from plot of MSD vs timestep size.

This result represented the model diffusion coefficient for our system. As an additional point of comparison, I simulated the suspension parameters using my simulation framework described in Chapter 3. Using the same parameters as described above when computing the analytical value, and by averaging over 20 replicants, I found a mean simulation diffusion coefficient of:

$$D_{Simulation} = 8.741 \times 10^{-13} \ \frac{m^2}{s}$$

which showed good agreement with the analytical expected result. The simulated value was 1.83% lower than the analytical value, well within any of the other percent differences listed in the simulation diffusion results described earlier in Chapter 3.

Next I generated several diffusion timeseries and used GDPTlab and my Matlab code mentioned in the previous section to compute the experimental values for the diffusion coefficient. GDPTlab outputs particle coordinates in the individual dimensions, x and y in this 2D case, so I wrote my Matlab code to compute the MSD using Equation 3.30 three ways:

- 1D analysis in the x-direction: $n = 1$ with the displacement computed using the x coordinates only

- 1D analysis in the y-direction: $n = 1$ with the displacement computed using the y coordinates only
- 2D analysis: $n = 2$ with the displacement computed using the x and y coordinates

and the results of the four trials are summarized below in Table 4.1.

Table 4.1: Experimental results of the diffusion coefficient from four separate trials.

Trial	D_x $(\frac{m^2}{s})$	D_y $(\frac{m^2}{s})$	D_{xy} $(\frac{m^2}{s})$
1	4.605×10^{-13}	5.673×10^{-13}	3.709×10^{-13}
2	4.554×10^{-13}	8.478×10^{-13}	4.699×10^{-13}
3	7.275×10^{-13}	6.905×10^{-13}	4.985×10^{-13}
4	6.651×10^{-13}	8.840×10^{-13}	5.965×10^{-13}

With these being early results, we can see that there are several different avenues in which we can interpret and analyze the data. Firstly, we notice all values are in the expected order of magnitude, which was an optimistic result for setting up the particle tracking system and working towards system and method verification. This shows that at least with my first trials, I am in the ballpark for tracking particles in 2D. Some values were closer to the expected analytical result than others, and all results, with the exception of the D_y from Trial 4 were lower than the expected value. Another general observation to note is, especially seen in Trials 1 and 3, that the diffusion coefficients in the x and y directions were relatively close in magnitude, indicating there was roughly symmetric displacement in those directions. This was graphically seen in the GDPTlab output plots for some trials as well such as the one shown in Figure 4.5. This symmetric behavior is also an optimistic result as we expect in true diffusion for the particle to be able to move, on average, the same in all directions. Of course that result is assuming infinitely long timescales and pure diffusion of independent particles in a totally quiescent fluid with no advective flow [53], which is not quite the exact situation replicated in my setup. This symmetric behavior was unfortunately not seen in all four of these trials to the same degree, with Trial 2 having the most significant difference between the two directions.

One final general trend that can be seen in the results tabulated above is the difference in the values for D_{xy} when compared to the 1D results within this same trials. One potential cause could be compounding errors with computations from imaging to GDPTlab and finally to my analysis code. This may be more of an issue with my Matlab code implementation. The method for computing the MSD with 2D vs 1D was coded from scratch, so I may have made an error when computing the displacements when inputting the arrays of coordinates from GDPT lab for the 2D computation. Additional work in double checking the code is the first thing on the list for future experiments if I continue this work. For the rest of the discussion, I will be focusing mainly on analyzing the values presented for the 1D results.

In general, with the exception of one result, the experimental diffusion coefficients were lower in magnitude than the "expected" analytical value. This behavior has several potential causes, and the first one I explored comes from the physical parameters that affect diffusion. Looking at the definition of the diffusion coefficient from the Stokes-Einstein Relation in Equation 3.31, we see that the particle and solution parameters can effect diffusion coefficient are the particle radius r, temperature T, and solvent viscosity η, which is also a function of temperature. First investigating the size effect, as particle size increases, the diffusion coefficient is reduced. The particles used in this trial were described as having a mean diameter of $500nm$, and to verify, I used a DLS particle size analyzer (Anton Parr Litesizer) and then imaged a sample of the particles in a SEM for further investigation. The results from both instruments can be seen in Figure 4.7 below.

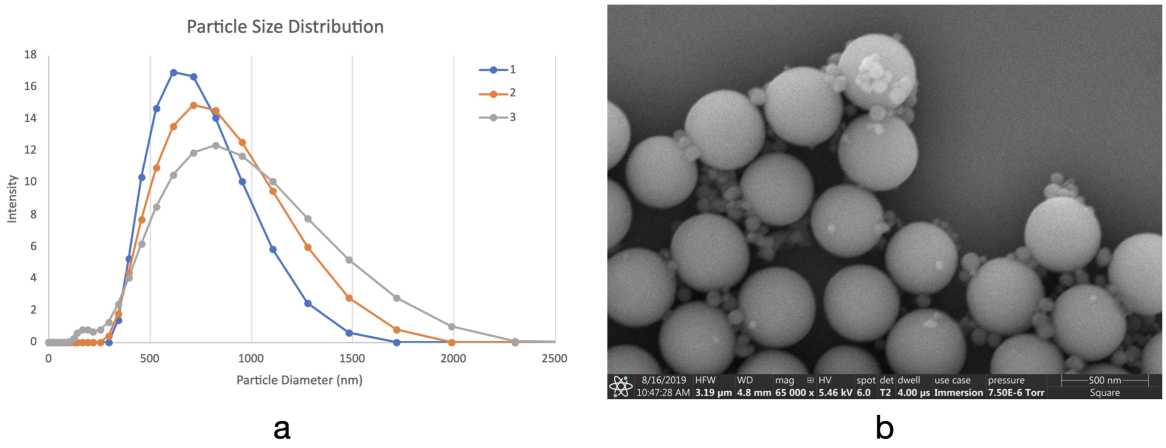

Figure 4.7: Litesizer and SEM image results from investigating Silica particle size. a) Output plot from the Litesizer showing size distributions from three successive runs. b) SEM image of silica particles used for diffusion experiments. Small particulates around the main spherical particles can be seen and may be contamination that affected the experimental diffusion coefficient results.

First looking at the left panel of Figure 4.7, we see the distribution of particle size from three separate successive runs. The mean diameters for the three runs were reported to be $660.2nm$, $668.0nm$, and $672.2nm$. The mean values were all fairly similar, but the size measurement distributions looked different between the three runs. In all cases, we see a mean higher than the expected value of $500nm$ as well as quite a wide, and skewed distribution in the direction of larger diameter. This immediately led me to believe something was off with my particle suspension, so I investigated further and imaged the particles with a SEM. In the right panel, we can see the larger particles appear to be close in size to the $500nm$ scale bar in the bottom right corner. However, we also see smaller particulates that are mixed in with the larger particles. I do not concretely know the source of these smaller particulates, but if they were present in my suspensions during the experiments that

could have a significant effect. I hypothesized that these contaminants may be from when I was mixing my solution and if they were sticking to the particles during the zeta sizer measurements, this could potentially explain the increased mean size, as well as the spread since the amount of small particles sticking to the larger ones most likely varied extremely widely. The phenomenon of particle agglomeration in general will be discussed further below as it was a common issue throughout my experiments. In addition to possibly explaining the behavior of the size distributions in the Litesizer results, the presence of these contaminants could also have had wider ranging effects on the diffusion experimental results. From my fluorescent images, I cannot tell with certainty if the smaller particulates were present, but we can explore the potential effect of an increased size of particle by revisiting the analytical value calculation. Again using Equation 3.31, but replacing the original radius of $250nm$ with the radius of the smallest mean particle size result from the Litesizer ($330.1nm$) we get the result of:

$$D_{LargerParticle} = 6.504 \times 10^{-13} \frac{m^2}{s}$$

which is closer to most of the results from Table 4.1. This is most certainly not the only reason the results from the experiments are were different, but it does show the need for several improvements in future experiments.

Immediately, one of the first steps I had planned to make was starting over with new imaging solutions and re-verifying the quality of the suspensions with the Litesizer and SEM before taking all new diffusion datasets. However, due to the onset of the COVID-19 pandemic as well as other time and funding constraints, I was unable to dedicate the time to rerun the experiments with new suspensions.

As mentioned above, size was not the only possible factor contributing to the difference in diffusion coefficient results. Temperature and viscosity were also potential factors based on the definition of the diffusion coefficient from Equation 3.31. I did not verify these properties with my own measurements like in my investigation of size, but those properties could both be measured independently in future experiments. In these experiments they most likely would not have varied as much as the effective particle size as the lab room where the suspensions were stored and where the microscope timeseries images were taken were in a building held around $20°C$.

Another consideration when analyzing this data was the potential for hindered diffusion due to the particles being near the glass slide. The Stokes-Einstein relation assumes pure diffusion free from any wall affects [8], but if the particles are close enough to the surface, their displacement can be affected in both the direction of the wall and those perpendicular to it [17]. For this current study, the effect of the wall on the diffusion coefficient can be described as:

$$\frac{D_{xy}(h)}{D_0} = 1 - \frac{9}{16}\frac{a}{h} + O\left(\frac{a^3}{h^3}\right) \tag{4.1}$$

where D_{xy} is the diffusion coefficient in the direction parallel to the wall, h is the distance from the wall in the perpendicular (z) direction, D_0 is the diffusion coefficient without accounting for any effects from the wall, and a is the particle radius. As h grows larger, we see a reduced

effect on the hindered diffusion. In my experiments I tried to choose particles far enough above the surface of the glass slide, but did not have a quantitative rule of thumb in place so some of the particles may have been closer to the wall. To see if this hindered diffusion effect was responsible for the reduced diffusion coefficient I measured, I calculated the height h above the glass slide the particles would need to be to have a diffusion coefficient averaged from the D_x and D_y values with an assumed particle size of $500nm$ in diameter. Using Equation 4.1 above, , neglecting the $O\left(\frac{a^3}{h^3}\right)$ term for this discussion, I found the particles would need to be $614nm$ above the surface of the glass slide to have as large of a reduction on the diffusion coefficient. It is unlikely that any of the particles I images were this close to the surface, however this hindered diffusion could still play a role in a smaller measured diffusion coefficient.

To explore further explore this effect, we can see to make a 1% reduction in relative diffusion coefficient $\frac{D_{xy}(h)}{D_0} = 0.99$, we get the ratio of $\frac{a}{h} = 0.0178$. In my system with particles with radii of $250nm$, this effect (1% relative reduction) could start to play a part in my measurements if the particle height was less than $14\mu m$ from the glass slide. Some of the particles imaged may have been within this threshold, and in future experiments I can account for this factor by making sure to note the z position of the particles relative to the glass surface either 1) factoring this height into the analysis of the experimental results when comparing to the analytical value, or 2) deciding on a procedure where the particles imaged are always chosen to be above a certain height to limit this effect. Option 2 above may be a little more difficult when experiments are expanded to 3D as the Airy disk signature from particles could be detected when the particle is below the image focal plane. For my system, I found I could detect the emitted light from particles with GDPTlab around $60\mu m$ above and below the focal plane, but that distance is system dependent and will need to be considered in future experiments. In practice, a combination of both options could be used, with the important practice of noting the z position of the focal plane relative to the glass slide providing the necessary information to account for this effect.

One major consideration I have not yet addressed is the limited amount of data from these experiments - not just the four reported trials and their diffusion coefficients, but also the limits on images in the data sets (my setup reliably gave me 130 images to work with before memory limits were reached). As I previously mentioned, I took many videos of particles, yet I only reported four trial results. This was partially due to most of the time I had for these experiments being dedicated to developing the setup for this round of experiments as well as the EPD observations discussed more in the next sections and limited time to fine-tune my methods specifically for this diffusion trials. To capture diffusion, I strove to find particles in the suspension that appeared to be independently diffusing - specifically not too close to other particles, but also close enough so that my images could capture multiple for averaging. This meant that many videos I captured were not fully analyzed if those conditions were not met for the entire duration, i.e. particles started to move closer together and agglomerate, or I found a particle that started to drift in a particular direction as opposed to randomly walk. The second example situation of particles advecting occurred often, and I observed

them especially if I tried imaging anywhere near the edge or surface of the droplet. At the edge, and especially if I had been imaging this particular drop for several trials, the water would begin to evaporate and the particles suspended would start to advect towards that edge. Several of the timeseries I took ended up containing situations like the above, so many were not analyzed further. In future experiments, I might aim to change the setup from a droplet to image the particle suspension in a larger volume that allowed for more locations not affected by this advection. One option is the EPD cell used for the EPD observations described below. A change like that would help me gather more timeseries in general, which give me a more robust study of my setup's capability to track particles. More data in general will also be helpful in future studies, as the MSD is computed with the ensemble average, which averages over particles and time increments. Both an increased number of particles, such as in a more concentrated solution, and an increased number of time increments made available by more images in a timeseries via either longer durations at the same framerate or a higher framerate with a similar duration. Both would aid in improving the ability of that ensemble average to more accurately compute the diffusion coefficient and would be directions I looking into for future experiments.

In summary, this section described the preliminary results from my 2D diffusion experiments. In this section, I reported results from four different trials and discussed several factors that could explain why my experimental results diverged from the analytical expected result. While these results showed that more work is necessary to verify this experimental setup, I am motivated that the early results were in the right order of magnitude and that these early trials resulted in many lessons learned that will be further discussed in the future directions section below. Although work still remains to fully verify this setup, these early results still showed progress towards the goals of making a particle tracking setup that can observe EPD in action. The next set of experiments further adds to that progress.

4.3.2 Observation of Electrophoresis, EPD

While quantitative verification of setup was being completed with the diffusion experiments mentioned above, I also wanted to move forward with EPD setup. This next set of experiments was aimed at observing particles depositing via EPD *in-situ*.

The goal of these experiments is to observe deposition of particles under EPD. Using the single camera setup as before, an EPD cell will be used to provide the electric field needed to drive the electrophoresis and deposition of particles. The cell will be transparent allowing the deposition to be captured on the camera for observation. In the future, experiments like this could directly lead to particle tracking data in the form of trajectories of the particles as they deposit. This trajectory data will be valuable in several aspects to the EPD field including increasing understanding of some of the kinematics and phenomena specific to EPD as well as helping validate and verify models seeking to capture the physics of EPD for optimization and process development. These experiments did not quite get to that point, but this early work can lead to more possibilities in the future. More details on future directions for this research will be presented in the next section.

EPD Cell and setup on microscope

For these experiments, I used the same basic setup on the inverted microscope as described previously, but with EPD components added. The added EPD components included the EPD cell and DC power source, a Keithley 2400 SourceMeter. Together they were integrated on the microscope basically replacing the glass slides from the diffusion experiment setup. The EPD cells were constructed as shown in the Figure 4.8 below. The cell is configured

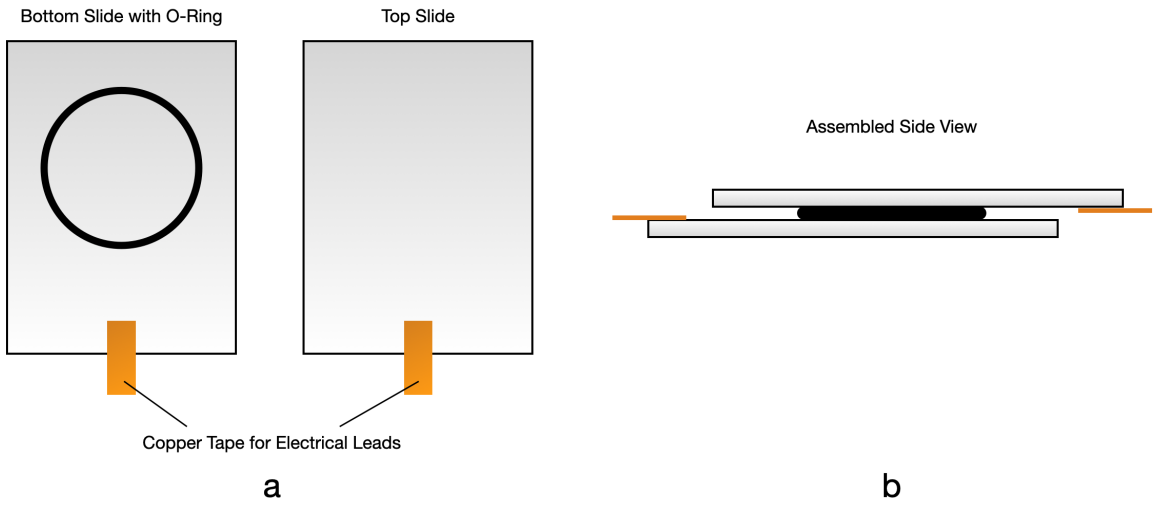

Figure 4.8: Schematic of the EPD Cell used for observations of deposition. a) Top view of the two slides used showing components. b) Side view of the cell assembled as it would look when making an observation on the microscope.

like a sandwich with two 2"x3" glass slides as the bread. The bottom slide has an o-ring adhered in place to form a reservoir for the particle suspension which also serves as a spacer to separate the two slides. In this case I adhered the o-ring to the slide with a UV-cured optical adhesive, but other adhesives could have been used. Both slides have one side with an Indium Tin Oxide (ITO) coating which allows it to be electrically conductive while optically transparent. When connected to the DC power source, these conductive faces will serve as deposition electrode and the counter electrode. The o-ring was adhered to the ITO-coated side of the bottom slide. Finally, for ease of making electrical connections, I attached a piece of conductive copper tape to each slide for connecting to the DC power source. Together this creates the transparent "cell" that can contain the particle imaging suspension as well as allow EPD to occur while the camera can observe the particles in the direction of deposition. The steps to create this device are also detailed in Appendix A.

For the microscope setup, this experiment was very similar to the diffusion trials above with some minor changes. The main change was the addition of the DC power source and it's connection to the EPD cell for imaging. As seen in the Figure 4.9, I situated the EPD cell

on the microscope stage such that the reservoir of particle suspension can be observed by the objective microscope. I then connected the DC power source to the electrical leads created by the copper tape to drive the electrophoresis of particles and the resulting deposition on the electrode.

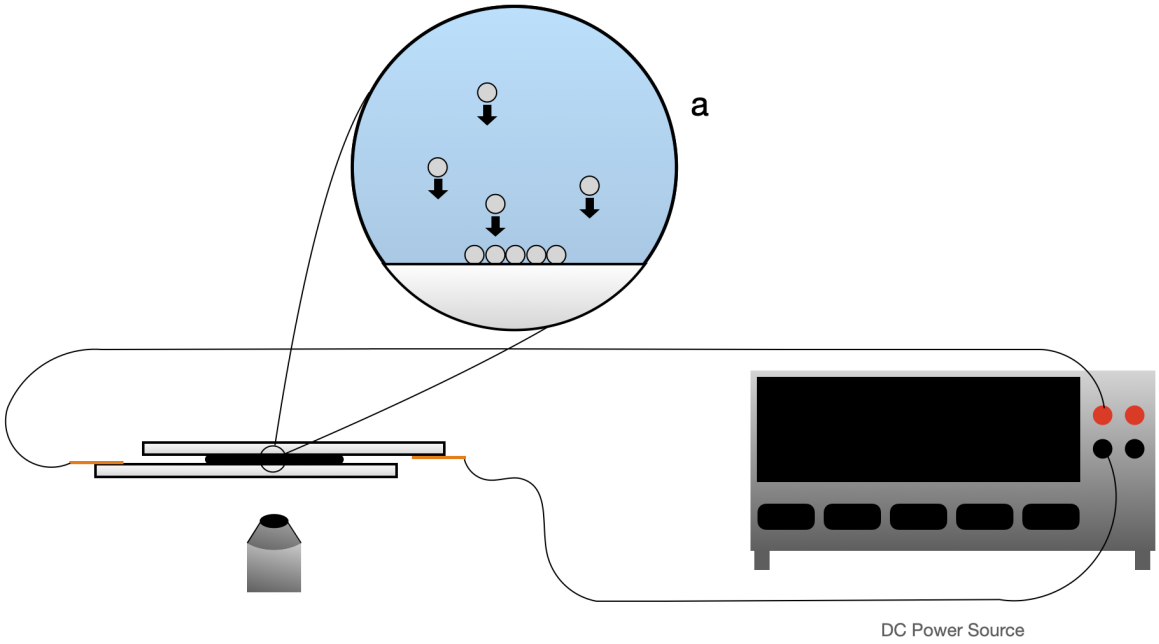

Figure 4.9: Schematic of the deposition experiment setup. EPD cell and power source are the newly added components from the previous setup. a) Zoomed in cutaway view of particles depositing inside the EPD cell.

Similar to the diffusion experiments above, I created the imaging suspensions by mixing the particles with DI water to form a suspension with desired concentration. I chose the concentration based on having enough particles in the frame to start observing the deposition of particles on the electrode. Too few particles in the suspension and a layer might not form, too many and the images might be too visually dense. Since these trials were more of a qualitative observation, the concentration of particles could be higher than those initially used for my early diffusion trials and were not limited by the limit of the particle tracking system to capture all particles frame-to-frame. For future particle tracking experiments, a discussion of a technique to balance the need for enough particles to form a deposit, but not so many that the particle tracking images are too visually dense will be further discussed in the future directions section. The suspensions used for imaging were sonicated as mentioned in the diffusion experiment section to ensure the particles were dissipated throughout the suspension and not agglomerated. For this set of observations, I used $0.8\mu m$ diameter polystyrene particles that were not fluorescently labeled for development. The images below were taken in a brightfield setup, which used the halogen lightsource on the

Axiovert 200 instead of the 120Q lightsource like for the fluorescent images. I began taking fluorescent images for observation of deposition, but due to time constraints and other factors, I did not complete trials to report here. This will be further discussed in the future research directions section.

Qualitative Results and Discussion

The preliminary observations of particle deposition on my system are presented here. While the results are not quatitative in nature, this early work showed was a step towards that goal. I also discuss some behavior observed during these depositions that can be of interest for future studies.

Using the procedure discussed above, I took timeseries images of the particle suspensions within the EPD cell. For imaging, I found a setting of $5V$ and $1A$ worked well for observing particles in my EPD cell. I would first begin the acquisition and then turn on the power source output to produce the voltage differential that drives the particle electrophoresis and deposition on slide surface of the EPD cell. I moved the stage to focus on a region just above the glass slide to capture the depositing particles in focus. For these acquisition settings with the brightfield images, I used a framerate of 30 frames per second for a duration of 10 seconds.

Figure 4.10 below shows select frames from one of the deposition observations with the frames taken at time values of $t = 0, 2, 4, 6, 8,$ and 10 seconds. In the first frame, a few particles are visible but not yet in focus indicating they are above the focal plane. In the next frame, we see more particles moving into the field of view with some coming more into focus and approaching the surface of the glass slide. This pattern continues through the deposition process in the next two frames as we see more particles enter the field of view and more coming into focus near the slide surface. Around the second to last frame we see that the amount of particles coming into the field of view seems to slow down relative to the earlier increases, and finally in the last frame we see the highest number of particles near the slide surface. These early videos taken of the deposition as it was occuring was an exciting milestone to hit, even without setting it up for quanitative analysis. This showed that my setup on the microscope could image particles depositing via EPD with the single camera setup and was the first step in moving towards generating the particle trajectories.

From this early deposition video, we can make a few observations of some particle behavior during EPD. One was the behavior seen with different field strengths. When taking these first observations, I started with a voltage setting of $1V$ and then increased that later on as I made observations, as shown in the images used for Figure 4.10 where the voltage was set to $5V$. When starting low, I noticed not only a longer travel time for particles to enter the field of view, but also less particles depositing onto the slide. This may indicate that the electrical driving force due to the applied potential was not high enough to overcome repulsive interactions with the surface. As mentioned previously, a minimum electrical driving force is required for deposition [19]. As I increased the voltage setting, the speed of particles entering the field and the number of particles depositing or sticking to the glass

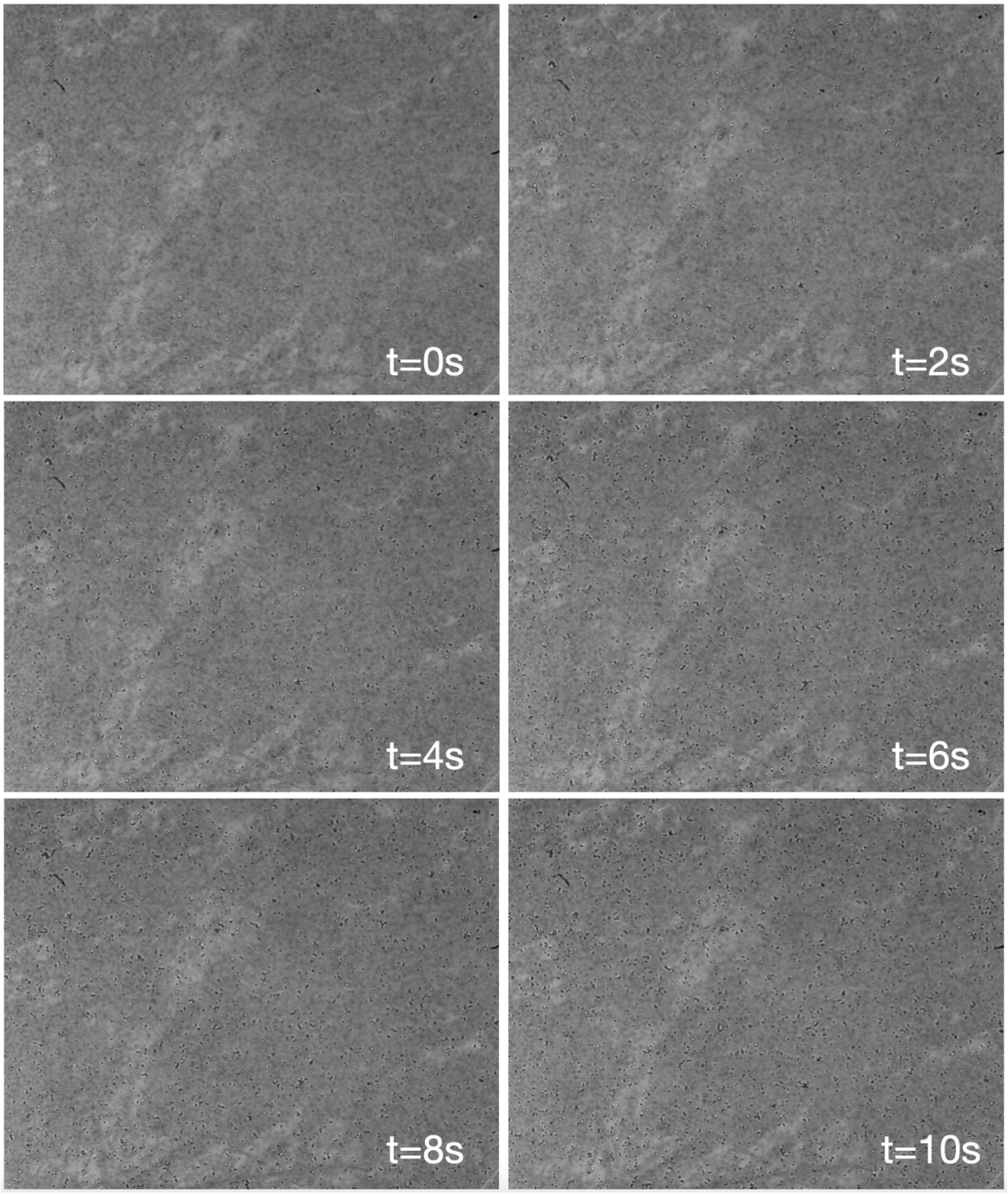

Figure 4.10: Frames captured from an early deposition trial. The six frames represent moments captured at $t = 0, 2, 4, 6, 8$, and 10 seconds.

slide also increased. In this limited trial run, the highest setting I used was $6V$ and in that case. Due to the limited nature of these observations, I can only hypothesize generally as to the behavior I noticed, but this behavior also is expected when looking at some of the theory behind EPD described in Chapter 2.

Another observation I noticed in this experimental run was the agglomeration of particles as they deposited onto the surface. I observed particle agglomeration in the early diffusion trials as well, but here it is part of the deposition process and an intended behavior to note. It is difficult to see in the larger images in Figure 4.10, but can be seen more in the zoomed in frames shown in Figure 4.11 below.

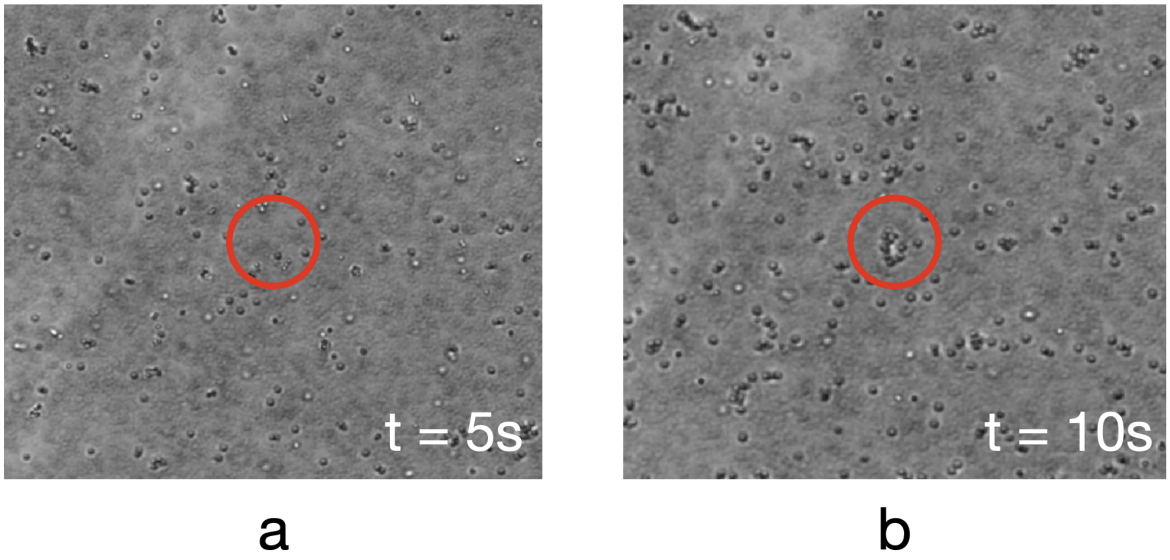

Figure 4.11: Zoomed in frames from the same deposition series as Figure 4.10. The circled region in both frames shows a) the particles as they are entering the field of view before they are deposited, and b) particles as they agglomerate while depositing.

The circled regions in Figure 4.11 showed that groups of particles started to combine and agglomerate as they deposited on the surface. This particular timeseries of deposition did not capture the deposition of a complete layer, but I would expect to see the particles agglomerate and rearrange as more particles deposited. Future studies will be aimed at observing more particles and how they interact at the deposition site. While the experiments with EPD observations did not progress to the point of generating particle trajectories, I did get to observe particles depositing via EPD on my setup, and this early work can be a jumping off point for future studies of EPD. Possible direction of that future work are discussed in the next section.

4.4 Lessons Learned and Future Directions for Experimental Work

The experimental setup and results discussed so far are very early work in creating and verifying the particle tracking platform for *in-situ* EPD observation and continued efforts in this direction will help further develop the methods to achieve that goal. I had many lessons learned along the way that will be helpful for future experiments in observing EPD. This section will further discuss those lessons learned and speak to future directions for this experimental work.

Lessons Learned

First and foremost, to work with particle tracking systems I learned working the with proper suspension is crucially important. Speaking specifically to my results in the 2D diffusion trials, verifying the properties such as particle size was an important step to ensure I am measuring what I expect when evaluating displacements later on. Using the Litesizer provides not only a measurement of particle size, but also of the suspension's zeta potential - which is a critical property for the EPD process as discussed earlier in Chapter 2. The Litesizer results from my diffusion trials were also a clue that my effective particle sizes were not quite what I expected and led to further investigations with imaging on the SEM. In general, more measured data is key to understanding the outcomes of the experiment.

More measured data on factors including size as mentioned above, as well as imaging position can also improve my experiments. Recording the relative position of the particles I am imaging to the physical surface of the glass slide is another measurement that I did not take when performing my experiments, but is another important step for future experiments. For diffusion, that height above the glass slide is an important factor and if the particles are too close, the effect of hindered diffusion should be considered.

I can also further improve the diffusion studies and general development of the system by improving the quantity and quality of images. As mentioned for diffusion, the ensemble average component of the calculation can be aided by having more frames, or position data points for a particle in an experimental run. This was partly limited by the camera setup, however, more experimentation with acquisition settings may have provided alternative parameters for capturing more images. This can also be a factor if considering new equipment for creating another setup. The number of particles can also improve the ensemble average, so I can aim to take more images with more particles present in the field of view. I can achieve this by creating more suspensions with increased concentration of tracer particles.

Another factor possibly affecting my suspensions and diffusion results was hinted at earlier in that section's discussion: particle agglomeration. I previously discussed the potential for the smaller particulates sticking to the main tracer particles, but the potential for agglomeration between the tracer particles is also relevant to these experiments. Throughout the development of this process and the diffusion experiments, I observed particle agglomer-

ation many times. Sometimes it would only be one or two particles sticking together, other times it would be several, like the group of particles shown in Figure 4.12.

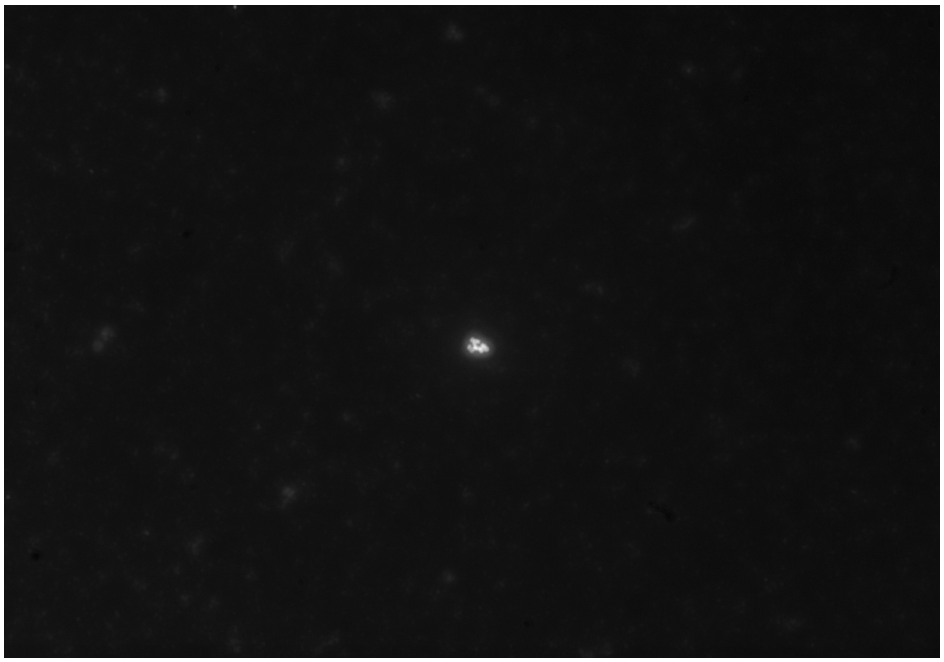

Figure 4.12: Example microscope image with group of agglomerated particles.

Typically when I searched for particles to image for the diffusion trials, I would avoid groups of particles like the ones shown. The Stokes-Einstein relation is derived for a single independent spherical particle, and a large group of particles will not exhibit the classical Brownian motion so they would result in different results if they were included in the particles used for the MSD computation. In the experimental procedure development, I tried to prevent this agglomeration by sonicating the suspensions as mentioned in the sections above. However, it is possible that some particles still agglomerated after sonication, especially if I was imaging over a longer period of time and the particular trial was done later in the day after the suspension was allowed to settle. In the case where it may be only a pair of particles, and they were only detectable by a larger Airy disk such as if they were on the upper or lower boundaries in the z-direction, the particles could adversely affect the overall diffusion coefficient calculations because they were not undergoing the classic Brownian motion. This issue could be addressed in future experiments by 1) sonicating the suspensions well before the taking data to prevent agglomeration in the first place, and 2) limiting the time a suspension is allowed to settle while taking data.

Future Directions

So far, my experimental work has started to make progress on the two original goals mentioned at the beginning of the chapter, but there is still a lot of room for continued progress. To continue this direct work, I would break it into the following major milestones:

1. Continue development of procedures for suspension and data analysis and redo 2D diffusion experiments.

2. Use a complete GDPT measurement to verify the setup with 3D diffusion experiments.

3. Use verified system with GDPT to produce quantitative data of EPD experiments.

To start with the first milestone, my work so far has accomplished creating the platform for particle tracking, and started verifying the data from observations in 2D diffusion. The results I presented in this chapter showed a lot of work still needs to be done to continue that verification. The 2D diffusion experiments are meant to be the first test of the basics of the platform eventually being used to observe EPD, and more data to show the data from tracking fluorescent particles in 2D will inspire confidence to move on to the next step. These trials should be performed with particle suspensions made with particles with sizes verified on a Litesizer or SEM before use in the particle tracking trials. Properly sonicating the suspensions is another key step I would definitely use, either a bath sonicator or even a horn sonicator as necessary to avoid the particle agglomeration issue. Finally, taking note of the particle focal plane's position with respect to the glass slide surface will provide extra information on the potential effect of hindered diffusion due to wall effects as the particles approach the wall. I believe making those main additions to the work presented so far will improve future 2D diffusion experiments for this particle tracking platform. Finally, with the process of creating suspensions for imaging better tuned, I believe more diffusion trials performed will further improve the confidence in the verification of the system. More data points will improve the averaging performed in the calculations as well as provide more insight on the reliability of the system.

After fine-tuning the process for performing diffusion experiments and evaluations in 2D, I would move on to the second milestone to evaluate the diffusion of particles in 3D with the platform. The suspensions and physical components of the system will have been mostly fully developed during the work towards the first milestone, so the additional development in this milestone will more likely be in the direction of refining the images for use with GDPTlab. For the 3D study, the biggest addition to the previous work is creating the calibration image stacks. I did not present results with them earlier, but I did make several early calibration stacks to begin 3D evaluations with GDPTlab. To take the calibration images, I used the same setup as the 2D diffusion trials and located a particle or set of particles that were near the surface of the glass slide. I then noted the location of the focal plane of the approximate center of the particle as a reference, then moved the stage up until I could barely see the Airy disk from the particle. Next, in small increments of $2\mu m$, I moved the stage down and

took and image at each increment, stopping when I could barely see the Airy disk again. The calibration stack was usually about 60 images.

With these first attempts at calibration stacks, I learned a few things about the images that will help guide future experiments. First, this process was slow, as each image required time for me to adjust the stage height, to view the image preview to assure noise and contrast were acceptable, and finally to take the image acquisition and save the files. This could be on the order of 20-30 seconds so a full stack would take up to 30 minutes. This led to concerns about photobleaching of the fluorescent particles, so I also started to make sure to close the shutter on the lightsource while not in use during image acquisition. This process could also be improved and simplified if the microscope had motor controlled stages, as I had to manually adjust the position with the focus knob. This would reduce the time, and increase the reliability, but would also increase the cost of the setup.

Another point I learned with these early calibration stack images was the importance of maintaining z position of the particles. The ability of the GDPT method to measure the z position of particles accurately is determined by the accuracy of the calibration stack. In my first efforts, the particles were settled near the surface of the glass slides, but were not totally stationary. Motion in the x and y directions was not an issue as long as the particles did not move out of frame, as GDPTlab was able to find the approximate center of the Airy disk in the calibration images and correct for differences in 2D position when training the calibration model. Since the particles were not attached to the glass slide however, they also were able to move slightly in the z direction. This motion was not large in magnitude, but definitely was large enough to minimize the difference in sequential images. In some cases significant motion may have been able to make an image look like it was out of order in the stack such as if a particle moved up a large amount in the water and then back down between images. This led to calibration image stacks that improperly trained the model for predicting the z position. For future calibration stacks, I would aim to keep the particles constrained, especially in the z direction. One first option, would be to find a particle that is already stuck to the glass slide, as this will happen on occasion. With my dilute suspensions, I had trouble finding particles already stuck, but it might just have taken more time to find some. Another option I would use would be to use an EPD cell and deposit a small amount of particles to the surface of the bottom slide thereby constraining the particle for the entire imaging process. This would ensure that the particles were in a constant position for all calibration images. Speeding up the process either through practice or a more automated method, avoiding photobleaching, and constraining the particles will aid future experiments in improving the calibration stack images.

The first two milestones are working towards verifying the system to eventually produce the trajectories of particles depositing via EPD. Once those are complete, the third milestone can be approached. So far, my work towards that milestone consisted of early trials of implementing and observing EPD on the microscope. I was able to integrate the EPD components with the microscope and observed EPD of polystyrene particles. Future work in towards this milestone will combine the GDPT measurement with deposition timeseries images of the particles. While these first attempts were done with particles with no fluores-

cent label and images were taken with brightfield background, future studies will also use fluorescent particles, similar to the diffusion trials for particle tracking. At first, suspensions with lower particle concentrations will be easier to use for development and observation. Experiments investigating the deposition of a single layer can provide good insight into deposition behavior as well as further develop the measurement capabilities of the system as the calibration and experimental image parameters are further refined. As experiments progress, observing depositions that span multiple layers will also be of interest. To reduce the inevitable increase in visual density of particles, the suspensions can be cleverly chosen to use refractive index-matched particles and solutions. The deposit can begin to form with the near-invisible index-matched particles before fluorescent tracer particles are introduced allowing observations of the tracer particles and their interactions with the previously deposited layers. This concept is shown below in Figure 4.13. There are several potential solvent and particle combinations that can provide the index-matched properties with a first potential option of silica particles ($n = 1.458$) and Tetrahydrafurfuryl Alcohol ($n = 1.456$) as used by Bender and Wagner [6]. A non-exhaustive list of additional options has been compiled in a review by Wiederseiner et al [60].

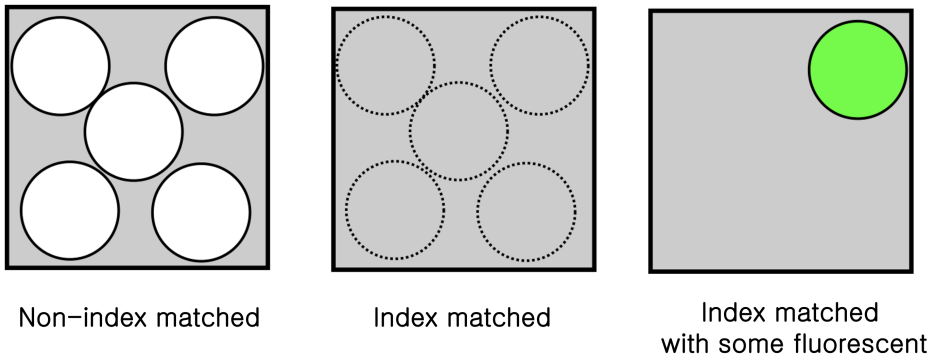

Figure 4.13: Graphic introducing the index-matched particle and tracer particle technique for imaging higher particle concentration systems.

Starting from my preliminary work with these experiments, there are different directions in which future work could proceed, but the path laid out here may be helpful in guiding those experiments that seek to achieve that third milestone from above: quantitative analysis of *in-situ* EPD.

4.5 Summary and Conclusions

This chapter discussed my preliminary experimental work towards further understanding the kinematics of the EPD process. The two main goals of the work were to:

1. Provide a platform to study *in-situ* 3D trajectories of particles during EPD under a variety of experimental parameters.

2. Provide particle trajectories that can be compared to and inform simulations to more accurately capture the complex behavior of particles during EPD for future process optimization.

To build the particle tracking platform for my experiments, I used a fluorescent microscope set up to image fluorescent particles and use a single camera to track particles in 3D using the GDPT technique. On the way to prepping the system for observing EPD directly, I performed simple 2D diffusion experiments to start to verify the system. Those experiments provided many lessons in the operation of the system and showed good directions for more 2D tests and 3D experiments after that to verify the system. I also progressed in developing the methods for observing EPD on the microscope system by constructing transparent EPD cells for observation and taking videos of particles depositing. I did not use the very preliminary observations for any quantitative analysis, but they did show that my system could be used to observe EPD *in-situ*. Finally, I presented some lessons learned and future directions to continue this work towards quantitatively observing the particles depositing via EPD to enhance our understanding of the kinetics and to inform simulations for further optimisation and development of the process.

Chapter 5

Summary and Conclusions

As external field-driven AM processes have gained more interest for their abilities to manufacture components with tailored material properties and geometries, more studies are needed to develop and optimize these processes. In this work, I focused on electric field-driven processes, such as electrospray of particles in air, and Electrophoretic Deposition of colloid particles suspended in a liquid, and aimed to contribute towards further understanding through a combination of computational and experimental work. With the process of EPD as a main focus, I discussed how the electric field-driven process can be used for several applications including colloidal crystals. While the kinetics of the EPD process have been studied through *ex-situ* observations, the underlying particle dynamics are not yet well understood and simulations for predicting the crystal structure of this process are computationally intensive and are still being developed. My work discussed in Chapter 3 involved the development of a particle-based framework, which I used as a platform for studying these electric field-driven AM processes. The framework was designed to run on limited computational resources to provide a potential development tool in combination with existing higher fidelity models that use more computing resources. Through developmental milestones, I compared results of diffusive motion and electrophoretic velocity behavior with analytic theory and found good agreement before exploring qualitative particle behavior with the full deposition model. While these deposition simulations were mostly performed with parameters similar to electrospray of particles in air, they showed the capability of the framework which could be used to further explore depositions of colloids via EPD in the future. In Chapter 4, I discussed preliminary experimental work towards *in-situ* observation of the EPD process to increase general understanding of how particles integrate into a deposit. I created a particle tracking setup to observe particles and began diffusion trials to verify the setup for eventually generating particle trajectories during EPD. Due to the onset of the COVID-19 pandemic, I was limited to preliminary development of a particle tracking platform, but was able to visually observe particle deposition. These conceptual results showed that, with further development, my experimental setup could be used to provide quantitative data of particle trajectories to also inform the particle simulations.

Both the numerical and experimental studies I discussed in this dissertation showed good

preliminary results, as well as several avenues for future studies. The simulation work is a stepping stone to developing a "digital twin" of the electric field-driven AM processes, and the particle tracking platform is in the early stages of providing particle trajectories to both inform future simulations and contribute directly to our understanding of the EPD process. From these efforts, I learned many lessons applied to both simulation work and experimental studies, all of which will be invaluable tools I can use towards any future endeavors related to AM process development.

Bibliography

[1] Bruce J. Ackerson et al. "Crystallization by settling in suspensions of hard spheres". In: *Phys. Rev. E* 59 (6 1999), pp. 6903–6913. DOI: 10.1103/PhysRevE.59.6903. URL: https://link.aps.org/doi/10.1103/PhysRevE.59.6903.

[2] Andor. *Solis I.* Version 4.32.30065.0. URL: https://andor.oxinst.com/products/solis-software/solis-i.

[3] Rune Barnkob, Christian J. Kähler, and Massimiliano Rossi. "General defocusing particle tracking". In: *Lab Chip* 15 (17 2015), pp. 3556–3560. DOI: 10.1039/C5LC00562K. URL: http://dx.doi.org/10.1039/C5LC00562K.

[4] Rune Barnkob and Massimiliano Rossi. "DefocusTracker: A Modular Toolbox for Defocusing-based, Single-Camera, 3D Particle Tracking". In: *Journal of Open Research Software* (2021). DOI: 10.5334/jors.351.

[5] Rune Barnkob and Massimiliano Rossi. "General defocusing particle tracking: fundamentals and uncertainty assessment". In: *Experiments in Fluids* 61.4 (2020), p. 110. DOI: 10.1007/s00348-020-2937-5. URL: https://doi.org/10.1007/s00348-020-2937-5.

[6] Jonathan Bender and Norman J. Wagner. "Reversible shear thickening in monodisperse and bidisperse colloidal dispersions". In: *Journal of Rheology* 40.5 (1996), pp. 899–916. DOI: 10.1122/1.550767. eprint: https://doi.org/10.1122/1.550767. URL: https://doi.org/10.1122/1.550767.

[7] L Besra and M Liu. "A review on fundamentals and applications of electrophoretic deposition (EPD)". In: *Progress in Materials Science* 52.1 (Jan. 2007), pp. 1–61. ISSN: 00796425. DOI: 10.1016/j.pmatsci.2006.07.001. URL: https://linkinghub.elsevier.com/retrieve/pii/S0079642506000387 (visited on 06/27/2019).

[8] Xin Bian, Changho Kim, and George Em Karniadakis. "111 years of Brownian motion". In: *Soft Matter* 12 (30 2016), pp. 6331–6346. DOI: 10.1039/C6SM01153E. URL: http://dx.doi.org/10.1039/C6SM01153E.

[9] S. Biringen and C.-Y. Chow. "Flow Topics Governed by Ordinary Differential Equations: Initial-Value Problems". In: *An Introduction to Computational Fluid Mechanics by Example*. John Wiley & Sons, Ltd, 2011. Chap. 1, pp. 1–49. ISBN: 9780470549162. DOI: https://doi.org/10.1002/9780470549162.ch1.

[10] D. S. Bolintineanu et al. "Particle dynamics modeling methods for colloid suspensions". In: *Computational Particle Mechanics* 1.3 (2014), pp. 321–356.

[11] S. Bradbury and P. Evennett. *Contrast Techniques in Light Microscopy*. BIOS Scientific Publishers, Ltd., 1996.

[12] T. M. Braun et al. "Simulation of Copper Electrodeposition in Millimeter Size Through-Silicon Vias". In: *Journal of The Electrochemical Society* 167.16 (2020), p. 162508. DOI: 10.1149/1945-7111/abd112. URL: https://dx.doi.org/10.1149/1945-7111/abd112.

[13] Universität der Bundeswehr München. *GDPTlab, matlab implementation of the general defocusing particle tracking*. Version 1.0. URL: https://www.unibw.de/lrt7/gdpt.

[14] Christoph Cremer and Barry R. Masters. "Resolution enhancement techniques in microscopy". In: *The European Physical Journal H* 38.3 (Apr. 2013), pp. 281–344. ISSN: 2102-6459, 2102-6467. DOI: 10.1140/epjh/e2012-20060-1. URL: http://link.springer.com/10.1140/epjh/e2012-20060-1 (visited on 03/28/2023).

[15] John C. Crocker and David G. Grier. "Methods of Digital Video Microscopy for Colloidal Studies". In: *Journal of Colloid and Interface Science* 179.1 (1996), pp. 298–310. ISSN: 0021-9797. DOI: https://doi.org/10.1006/jcis.1996.0217. URL: https://www.sciencedirect.com/science/article/pii/S0021979796902179.

[16] P. A. Cundall and O. D. L. Strack. "A discrete numerical model for granular assemblies". In: *Géotechnique* 29.1 (1979), pp. 47–65. DOI: 10.1680/geot.1979.29.1.47. eprint: https://doi.org/10.1680/geot.1979.29.1.47. URL: https://doi.org/10.1680/geot.1979.29.1.47.

[17] Eric R. Dufresne et al. "Hydrodynamic Coupling of Two Brownian Spheres to a Planar Surface". In: *Physical Review Letters* 85.15 (Oct. 9, 2000), pp. 3317–3320. ISSN: 0031-9007, 1079-7114. DOI: 10.1103/PhysRevLett.85.3317. URL: https://link.aps.org/doi/10.1103/PhysRevLett.85.3317 (visited on 08/14/2019).

[18] Nina V. Dziomkina, Mark A. Hempenius, and G. Julius Vancso. "Layer-by-layer templated growth of colloidal crystals with packing and pattern control". In: *Colloids and Surfaces A: Physicochemical and Engineering Aspects* 342.1 (2009), pp. 8–15. ISSN: 0927-7757. DOI: https://doi.org/10.1016/j.colsurfa.2009.03.049. URL: https://www.sciencedirect.com/science/article/pii/S0927775709001356.

[19] Begoña Ferrari and Rodrigo Moreno. "EPD kinetics: A review". In: *Journal of the European Ceramic Society* 30.5 (Mar. 2010), pp. 1069–1078. ISSN: 09552219. DOI: 10.1016/j.jeurceramsoc.2009.08.022. URL: https://linkinghub.elsevier.com/retrieve/pii/S0955221909004300 (visited on 06/27/2019).

[20] William E. Frazier. "Metal Additive Manufacturing: A Review". In: *Journal of Materials Engineering and Performance* 23.6 (2014), pp. 1917–1928. DOI: 10.1007/s11665-014-0958-z. URL: https://doi.org/10.1007/s11665-014-0958-z.

[21] Rishi Ganeriwala and Tarek I. Zohdi. "A coupled discrete element-finite difference model of selective laser sintering". In: *Granular Matter* 18.2 (2016), p. 21. DOI: 10.1007/s10035-016-0626-0. URL: https://doi.org/10.1007/s10035-016-0626-0.

[22] Brian Giera et al. "Mesoscale Particle-Based Model of Electrophoresis". In: *Journal of The Electrochemical Society* 162.11 (Jan. 1, 2015), pp. D3030–D3035. ISSN: 0013-4651, 1945-7111. DOI: 10.1149/2.0161511jes. URL: http://jes.ecsdl.org/content/162/11/D3030 (visited on 06/27/2019).

[23] Brian Giera et al. "Mesoscale Particle-Based Model of Electrophoretic Deposition". In: *Langmuir* 33.2 (Jan. 17, 2017), pp. 652–661. ISSN: 0743-7463. DOI: 10.1021/acs.langmuir.6b04010. URL: https://doi.org/10.1021/acs.langmuir.6b04010 (visited on 06/27/2019).

[24] Yu Guo and Jennifer Sinclair Curtis. "Discrete Element Method Simulations for Complex Granular Flows". In: *Annual Review of Fluid Mechanics* 47.1 (2015), pp. 21–46. DOI: 10.1146/annurev-fluid-010814-014644. eprint: https://doi.org/10.1146/annurev-fluid-010814-014644. URL: https://doi.org/10.1146/annurev-fluid-010814-014644.

[25] H. C. Hamaker. "Formation of a deposit by electrophoresis". In: *Trans. Faraday Soc.* 35 (0 1940), pp. 279–287. DOI: 10.1039/TF9403500279. URL: http://dx.doi.org/10.1039/TF9403500279.

[26] Yingbin Hu. "Recent progress in field-assisted additive manufacturing: materials, methodologies, and applications". In: *Materials Horizons* 8.3 (2021), pp. 885–911. DOI: 10.1039/D0MH01322F. URL: http://dx.doi.org/10.1039/D0MH01322F.

[27] C W. Hull. "Apparatus for production of three-dimensional objects by stereolithography". 4575330. 3D Systems Inc. Aug. 8, 1984.

[28] Neil Hunt, Roger Jardine, and Paul Bartlett. "Superlattice formation in mixtures of hard-sphere colloids". In: *Phys. Rev. E* 62 (1 2000), pp. 900–913. DOI: 10.1103/PhysRevE.62.900. URL: https://link.aps.org/doi/10.1103/PhysRevE.62.900.

[29] Nan Kang et al. "On the texture, phase and tensile properties of commercially pure Ti produced via selective laser melting assisted by static magnetic field". In: *Materials Science and Engineering: C* 70 (2017), pp. 405–407. ISSN: 0928-4931. DOI: https://doi.org/10.1016/j.msec.2016.09.011. URL: https://www.sciencedirect.com/science/article/pii/S0928493116311833.

[30] Chun-Han Lai et al. "Rapid Fabrication of Cylindrical Colloidal Crystals and Their Inverse Opals". In: *Journal of The Electrochemical Society* 157.3 (2010), P23. DOI: 10.1149/1.3280268. URL: https://dx.doi.org/10.1149/1.3280268.

[31] Siu Kwan Lam, Antoine Pitrou, and Stanley Seibert. "Numba: A LLVM-Based Python JIT Compiler". In: *Proceedings of the Second Workshop on the LLVM Compiler Infrastructure in HPC*. LLVM '15. Austin, Texas: Association for Computing Machinery, 2015. ISBN: 9781450340052. DOI: 10.1145/2833157.2833162. URL: https://doi.org/10.1145/2833157.2833162.

[32] Kangtaek Lee and Sanford A. Asher. "Photonic Crystal Chemical Sensors: pH and Ionic Strength". In: *Journal of the American Chemical Society* 122.39 (Oct. 2000), pp. 9534–9537. DOI: 10.1021/ja002017n. URL: https://doi.org/10.1021/ja002017n.

[33] Randall J LeVeque. *Finite Difference Methods for Ordinary and Partial Differential Equations: Steady-State and Time-Dependent Problems*. Society for Industrial and Applied Mathematics, 2007.

[34] Jeff W. Lichtman and José-Angel Conchello. "Fluorescence microscopy". In: *Nature Methods* 12 (2005), pp. 910–919. ISSN: 1548-7105. URL: https://doi.org/10.1038/nmeth817.

[35] Eric MacDonald and Ryan Wicker. "Multiprocess 3D printing for increasing component functionality". In: *Science* 353.6307 (2016), aaf2093. DOI: 10.1126/science.aaf2093. eprint: https://www.science.org/doi/pdf/10.1126/science.aaf2093. URL: https://www.science.org/doi/abs/10.1126/science.aaf2093.

[36] Mathworks. *Matlab*. Version R2021b. URL: https://www.mathworks.com/products/matlab.html.

[37] Jeronimo Mora et al. "Projection based light-directed electrophoretic deposition for additive manufacturing". In: *Additive Manufacturing* 22 (2018), pp. 330–333. ISSN: 2214-8604. DOI: https://doi.org/10.1016/j.addma.2018.05.020. URL: http://www.sciencedirect.com/science/article/pii/S2214860418300976.

[38] Debanjan Mukherjee and Tarek I. Zohdi. "Electromagnetic control of charged particulate spray systems—Models for planning the spray-gun operations". In: *Computer-Aided Design* 46 (2014). 2013 SIAM Conference on Geometric and Physical Modeling, pp. 211–215. ISSN: 0010-4485. DOI: https://doi.org/10.1016/j.cad.2013.08.034. URL: https://www.sciencedirect.com/science/article/pii/S0010448513001747.

[39] Debanjan Mukherjee et al. "Investigation of Guided-Particle Transport for Noninvasive Healing of Damaged Piping Systems by Use of Electro-Magneto-Mechanical Methods". In: *SPE Journal* 20.04 (Aug. 2015), pp. 872–883. ISSN: 1086-055X. DOI: 10.2118/169639-PA. eprint: https://onepetro.org/SJ/article-pdf/20/04/872/2128997/spe-169639-pa.pdf. URL: https://doi.org/10.2118/169639-PA.

[40] *multiprocessing — Process-based parallelism*. URL: https://docs.python.org/3/library/multiprocessing.html#.

[41] Bruce Roy Munson et al. *Fundamentals of Fluid Mechanics, Sixth Edition*. John Wiley & Sons, 2009.

[42] Landon Oakes et al. "Roll-to-Roll Nanomanufacturing of Hybrid Nanostructures for Energy Storage Device Design". In: *ACS Applied Materials & Interfaces* 7.26 (2015). PMID: 26053115, pp. 14201–14210. DOI: 10.1021/acsami.5b01315. eprint: https://doi.org/10.1021/acsami.5b01315. URL: https://doi.org/10.1021/acsami.5b01315.

[43] Andrew J. Pascall, Kyle T. Sullivan, and Joshua D. Kuntz. "Morphology of Electrophoretically Deposited Films on Electrode Strips". In: *The Journal of Physical Chemistry B* 117.6 (2013). PMID: 22866811, pp. 1702–1707. DOI: 10.1021/jp306447n. eprint: https://doi.org/10.1021/jp306447n. URL: https://doi.org/10.1021/jp306447n.

[44] Andrew J. Pascall et al. "Light-Directed Electrophoretic Deposition: A New Additive Manufacturing Technique for Arbitrarily Patterned 3D Composites". In: *Advanced Materials* 26.14 (2014), pp. 2252–2256. DOI: 10.1002/adma.201304953. eprint: https://onlinelibrary.wiley.com/doi/pdf/10.1002/adma.201304953. URL: https://onlinelibrary.wiley.com/doi/abs/10.1002/adma.201304953.

[45] Eric Perkins and John R. Williams. "Generalized Spatial Binning of Bodies of Different Sizes". In: *Discrete Element Methods*, pp. 52–55. DOI: 10.1061/40647(259)10. eprint: https://ascelibrary.org/doi/pdf/10.1061/40647\%28259\%2910. URL: https://ascelibrary.org/doi/abs/10.1061/40647%5C%28259%5C%2910.

[46] PMR. *Paint Robots Market Size, Global Industry Report, 2018-2023*. Available from: https://pmrpressrelease.com/paint-robots-market-size-global-industry-report-2018-2023/. 2019.

[47] Porsche. *Six stages to a perfectly painted Macan*. Available from: https://newsroom.porsche.com/en/company/paint-shop-10782.html. 2014.

[48] Brian G. Prevo and Orlin D. Velev. "Controlled, Rapid Deposition of Structured Coatings from Micro- and Nanoparticle Suspensions". In: *Langmuir* 20.6 (2004). PMID: 15835658, pp. 2099–2107. DOI: 10.1021/la035295j. eprint: https://doi.org/10.1021/la035295j. URL: https://doi.org/10.1021/la035295j.

[49] Markus Raffel, Christian E Willert, Jürgen Kompenhans, et al. *Particle image velocimetry: a practical guide*. Vol. 3. Springer, 2018.

[50] W.S. Rasband. *ImageJ*. URL: https://imagej.nih.gov/ij/.

[51] V Rokhlin. "Rapid solution of integral equations of classical potential theory". In: *Journal of Computational Physics* 60.2 (1985), pp. 187–207. ISSN: 0021-9991. DOI: https://doi.org/10.1016/0021-9991(85)90002-6. URL: https://www.sciencedirect.com/science/article/pii/0021999185900026.

[52] Guido van Rossum. *Python*. Version 3.9.13. URL: https://www.python.org.

[53] W. B. Russel, D. A. Saville, and W. R. Schowalter. *Colloidal Dispersions*. Cambridge Monographs on Mechanics. Cambridge University Press, 1989. DOI: 10.1017/CBO9780511608810.

[54] Partho Sarkar and Patrick S. Nicholson. "Electrophoretic Deposition (EPD): Mechanisms, Kinetics, and Application to Ceramics". In: *Journal of the American Ceramic Society* 79.8 (1996), pp. 1987–2002. DOI: https://doi.org/10.1111/j.1151-2916.1996.tb08929.x. eprint: https://ceramics.onlinelibrary.wiley.com/doi/pdf/10.1111/j.1151-2916.1996.tb08929.x. URL: https://ceramics.onlinelibrary.wiley.com/doi/abs/10.1111/j.1151-2916.1996.tb08929.x.

[55] Peter H. Smith et al. "Magnetically assisted directed energy deposition". In: *Journal of Materials Processing Technology* 288 (2021), p. 116892. ISSN: 0924-0136. DOI: https://doi.org/10.1016/j.jmatprotec.2020.116892. URL: https://www.sciencedirect.com/science/article/pii/S092401362030306X.

[56] Christopher M. Spadaccini. "Additive manufacturing and processing of architected materials". In: *MRS Bulletin* 44.10 (2019), pp. 782–788. DOI: 10.1557/mrs.2019.234.

[57] James W. Swan and Eric M. Furst. "A simpler expression for Henry's function describing the electrophoretic mobility of spherical colloids". In: *Journal of Colloid and Interface Science* 388.1 (2012), pp. 92–94. ISSN: 0021-9797. DOI: https://doi.org/10.1016/j.jcis.2012.08.026. URL: https://www.sciencedirect.com/science/article/pii/S002197971200937X.

[58] Tecplot, Inc. *Tecplot 360 EX*. Version 2021 R2. URL: https://www.tecplot.com.

[59] Kevin Verma et al. "Modeling and simulation of electrophoretic deposition coatings". In: *Journal of Computational Science* 41 (2020), p. 101075. ISSN: 1877-7503. DOI: https://doi.org/10.1016/j.jocs.2020.101075. URL: https://www.sciencedirect.com/science/article/pii/S1877750319308506.

[60] Sébastien Wiederseiner et al. "Refractive-index and density matching in concentrated particle suspensions: a review". In: *Experiments in Fluids* 50.5 (2011), pp. 1183–1206. DOI: 10.1007/s00348-010-0996-8. URL: https://doi.org/10.1007/s00348-010-0996-8.

[61] Marcus Worsley. *Unpublished image of colloidal crystal from EPD, LLNL.*

[62] Younan Xia, B. Gates, and Sang Hyun Park. "Fabrication of three-dimensional photonic crystals for use in the spectral region from ultraviolet to near-infrared". In: *Journal of Lightwave Technology* 17.11 (1999), pp. 1956–1962. DOI: 10.1109/50.802980.

[63] Wei-Cheng Yan, Jingwei Xie, and Chi-Hwa Wang. "Electrical Field Guided Electrospray Deposition for Production of Gradient Particle Patterns". In: *ACS Applied Materials & Interfaces* 10.22 (2018). PMID: 29758161, pp. 18499–18506. DOI: 10.1021/acsami.8b02914. eprint: https://doi.org/10.1021/acsami.8b02914. URL: https://doi.org/10.1021/acsami.8b02914.

[64] Guangming Zhang et al. "A Microscale 3D Printing Based on the Electric-Field-Driven Jet". In: *3D Printing and Additive Manufacturing* 7.1 (2020), pp. 37–44. DOI: 10.1089/3dp.2018.0154. eprint: https://doi.org/10.1089/3dp.2018.0154. URL: https://doi.org/10.1089/3dp.2018.0154.

[65] Xiaoji Zhang et al. "An Integrated Dual Ultrasonic Selective Powder Dispensing Platform for Three-Dimensional Printing of Multiple Material Metal/Glass Objects in Selective Laser Melting". In: *Journal of Manufacturing Science and Engineering* 141.1 (Oct. 2018). 011003. ISSN: 1087-1357. DOI: 10.1115/1.4041427. eprint: https://asmedigitalcollection.asme.org/manufacturingscience/article-pdf/141/1/011003/6278923/manu_141_01_011003.pdf. URL: https://doi.org/10.1115/1.4041427.

[66] T. I. Zohdi. "Additive particle deposition and selective laser processing-a computational manufacturing framework". In: *Computational Mechanics* 54.1 (2014), pp. 171–191. DOI: 10.1007/s00466-014-1012-6. URL: https://doi.org/10.1007/s00466-014-1012-6.

[67] T. I. Zohdi. "Embedded electromagnetically sensitive particle motion in functionalized fluids". In: *Computational Particle Mechanics* 1.1 (2014), pp. 27–45. DOI: 10.1007/s40571-014-0013-8. URL: https://doi.org/10.1007/s40571-014-0013-8.

Appendix A

Additional Experimental Details

The following appendix contains more details on some of the experimental procedures I used when performing the work described in Chapter 4.

Glass Slide Cleaning Procedure

1. Place glass slides in bath sonicator with water, try to keep separated to avoid slides.
2. Sonicate for 1 hour.
3. Remove slides from bath sonicator carefully using tweezers.
4. Rinse both sides of glass slide with Acetone.
5. Rinse both sides of glass slide with Isopropyl Alcohol.
6. Dry both sides of glass slide using nitrogen gas.

EPD Cell Assembly Steps

1. Clean ITO-glass slides using procedure described above.
2. Clean O-ring using Isopropyl Alcohol and wipe dry with a lint-free wipe.
3. Use multimeter set to check for continuity and determine which side of glass slides has the conductive ITO coating.
4. Place O-ring on one slide on the side with the ITO coating. Position as shown in Figure 4.8.
5. Spread optical adhesive around circumference of O-ring, making sure to create a seal on the slide.

6. Use UV light source to cure adhesive, working around the circumference to ensure all adhesive is cured properly.

7. Use tweezers to press on O-ring and check that adhesive is constraining the O-ring all the way around. Add more adhesive and cure if needed.

8. Apply copper tape to ITO-coated side on both slides for electrical leads.